Changing teleconnection patterns in the North Atlantic from 850 to 2099 AD - The role of atmosphere-ocean-sea ice interaction

Master's Thesis

Faculty of Science
University of Bern

presented by
Moritz Pickl
2017

Supervisor:
Prof. Dr. Christoph C. Raible

Institute for Climate and Environmental Physics
Oeschger-Centre for Climate Change Research
University of Bern

Abstract

The variability of the atmospheric circulation can be simplified by the concept of teleconnections, which characterize simultaneous variations of climate parameters at distant regions and therefore control the large-scale atmospheric flow. The climate in the North Atlantic sector is subjected to strong variations, and the most important teleconnection is the North Atlantic Oscillation (NAO), describing a meridional seesaw of sea level pressure. In this thesis, the spatio-temporal variability of the predominant teleconnections in the North Atlantic sector is investigated in a 1250-year simulation of the coupled general circulation model CESM. The application of wavelet transform to two NAO-indices yields that the temporal behaviour of the simulated NAO is highly non-stationary. Both indices exhibit strongest variations on inter-annual, decadal and multi-decadal timescales, but no specific frequency predominates over longer periods. Also the spatial patterns of the simulated wintertime teleconnections in the North Atlantic, assessed with 30-year running window teleconnectivity maps, show strong variations. Three different methods were employed to classify the individual teleconnection situations into meaningful groups, and all of them agree that NAO-like teleconnections with meridionally aligned centers of action prevail. According to the method which uses predefined box pairs to classify teleconnections, 71% of all time steps are characterized by at least one NAO-like teleconnection. However, zonally oriented teleconnections are present during almost half of the time steps (43%), and situations with neither NAO-like nor zonal teleconnections account for 15% of the time steps. Based on these results, the relationship between the different states of climate variability and the sea surface temperature and the extent of Arctic sea ice is investigated by composite and linear regression analysis. A consistent SST-pattern is found only in the central North Atlantic for NAO-like teleconnections, suggesting a regional connection between the atmosphere and the ocean. However, as the magnitude of the detected SST-signal is very low, it is unclear whether this linkage is reliable. With the applied method, no relation to distant SST (e.g. tropical Atlantic or Pacific) nor to the sea ice extent in the Arctic is found.

Contents

Chapter 1

Introduction

The North Atlantic Oscillation (NAO) is the most prominent pattern of atmospheric variability of the Northern Hemisphere. It characterizes a large-scale bipolar seesaw of atmospheric mass between the Arctic and the sub-tropical Atlantic. In other words, the NAO refers to an anti-correlation of the atmospheric sea level pressure between the centers of action, the northerly located near Iceland and the southerly near the Azores islands (*Wallace and Gutzler* 1981). Especially in the boreal cold season, the NAO exerts a strong influence on weather and climate in Europe and eastern North America (*Barnston and Livezey* 1987). By altering the large-scale atmospheric circulation in the North Atlantic region, the NAO affects the seasonal mean heat and moisture transports between the North Atlantic ocean and the adjacent continents as well as the paths and intensity of winter storms (*Jones et al.* 2003). Also sea surface temperature (*SST*), heat content and currents of the North Atlantic Ocean and sea ice cover in the Arctic and sub-polar North Atlantic experience significant changes induced by the NAO (*Visbeck et al.* 2003). This large-scale climatic impact of the NAO is accompanied by ecological, economic and hydrological implications, ranging from agricultural harvests, fishery yields and energy supply to water management (e.g. *Hurrell et al.* 2003).

Thanks to the prominence and the wide range of effects which come along with this phenomenon, the NAO has been subject of interest for a very long time within the climate research community. Being one of the oldest known weather patterns, its first qualitative description dates back to the late 18th century (*Wanner et al.* 2001). Since then, the research on the NAO has undergone many phases, from first statistical descriptions with correlation techniques over the dynamical understanding of the atmospheric processes and the relationship to other components of the climate system to changes of the NAO as response to anthropogenic climate change (*Wanner et al.* 2001). Due to its enormous and extensive impact, it is crucial to better understand its variability and dynamics on long time scales. Also in the context of detection and attribution of climate change, an understanding of internal climate processes and its differentiation from externally forced changes is essential. In the following section, the history of scientific research on the North Atlantic Oscillation will be addressed in more detail.

1.1 History of scientific research on the NAO

This section is mainly based on the review papers from *Wanner et al.* (2001) and *Stephenson et al.* (2003) which serve as profound and detailed surveys about the history of scientific research on the NAO. The first mentioning of the phenomenon was made by Hans Egede Saabye, a Danish missionary in the 1780s, who described the opposing temperatures between Denmark and Greenland in winter. In the 19th century, the first quantitative analyses of Northern Hemisphere climate variability were conducted. For example, *Dove* (1841) and *Hann* (1890) investigated temperature time series of the Northern Hemisphere and determined that zonal temperature variations were often more pronounced than meridional temperature variations.

The development of statistical methods and their application to climatological data in the early 20th century enabled *Exner* (1913) to identify an anti-correlation in the time series of sea level pressure over Iceland and the Azores. *Defant* (1924) derived a statistical mode and the first index of the NAO with a precursor of EOF analysis. At the same time, scientists started to investigate mechanisms that control this climate variability. While *Walker and Bliss* (1932) and *Bjerknes* (1964) considered the NAO as a regional phenomenon with drivers like ocean-atmosphere interactions, *Rossby and Collaborators* (1939) opined a hemispheric-scale point of view where land-sea contrasts and topography were the main drivers for the NAO.

With the progress of understanding atmospheric dynamics and large-scale planetary waves, theoretical studies about the interaction of pressure systems and the zonal circulation were conducted and zonal indices describing the mean zonal wind at specific latitudes were introduced (e.g. *Lorenz* 1967). *Barnston and Livezey* (1987) showed that the NAO is the only low-frequency mode of variability being present year-round, confirming that the NAO is one of the most dominant and robust circulation patterns on the globe.

Hurrell (1995) established a new two-point NAO-index, defined as the difference between the normalized sea level pressure in Lisbon (Portugal) and Stykkisholmur (Iceland), with the advantage of being extended back into the past which became the most commonly used NAO-index. In the 1990s, climate model simulations showed that NAO-like variability can be generated by atmosphere-only general circulation models, demonstrating that the formation of the NAO is a purely atmospheric process (e.g. *Glowienka-Hense* 1990).

1.2 Current research on the NAO

Even though the NAO attracted researchers for more than two centuries, there are still many open questions about the phenomenon. One example is the still ongoing debate whether the NAO is confined to the North Atlantic sector or if it is a fraction of the Northern Hemisphere Annular Mode (NAM), which exhibits the strongest variability over the North Atlantic sector (*Thompson and Wallace* 1998).

Another debate concerns the temporal fluctuations of the NAO-index. Showing variability on many timescales, ranging from the weekly formation and dissipation of single events over inter-seasonal and inter-annual variability to decadal and multi-decadal fluctuations, the NAO-index exhibits no preferred time scale (*Hurrell et al.* 2003). However, the NAO-index shows periods with enhanced or reduced low-frequency (multi-decadal) variability (*Appenzeller et al.* 1998; *Luterbacher et al.* 1999; *Raible et al.* 2001), with many different mechanisms suggested in the literature. The most important ones are atmosphere-ocean (e.g. *Raible et al.* 2001; *Eden and Willebrand* 2001; *Marshall et al.* 2001; *Czaja et al.* 2003) - and atmosphere-sea ice interactions (e.g. *Nakamura et al.* 2015; *Pedersen et al.* 2016), external forcings such as greenhouse gas emissions (e.g. *Ulbrich and Christoph* 1999), volcanic eruptions (e.g. *Le et al.* 2016) and internal atmospheric processes and stratospheric coupling (e.g. *Baldwin and Dunkerton* 1999; *Orsolini et al.* 2011). Despite the large amount of studies concerning the mechanisms for temporarily enhanced multi-decadal variability of the NAO, no agreement has been achieved yet.

Finally, not only the temporal but also the spatial characteristics of the NAO were found to be non-stationary. Several studies investigating the low-frequency characteristics of teleconnection patterns in the North Atlantic region with global circulation models (GCM) have detected changes in shape and/or position of these patterns (e.g. *Raible et al.* 2006; *Moore et al.* 2013; *Raible et al.* 2014). *Ulbrich and Christoph* (1999) investigated the NAO-index and the positions of the centers of action of the NAO with rising greenhouse gas forcing and found a systematic north-eastward shift of the northern center of action. In other studies, structural changes of the NAO-centers of action can be linked to atmosphere-ocean coupling (*Raible et al.* 2001) or to ENSO (*Raible et al.* 2004). *Moore et al.* (2013) applied the teleconnectivity method from *Wallace and Gutzler* (1981) and observed multiple locations for the centers of action associated with the NAO, with the dominance of a pair of centers of action changing over time. They found that this multi-decadal mobility is not captured by the first empirical orthogonal function (EOF) for the Atlantic sector, which is often used to describe the NAO. They rather explained systematic displacements of the centers of action by a linear combination of the first three EOFs. *Raible et al.* (2014) investigated the stability of Northern Hemisphere teleconnections in different millennial-scale GCM-simulations and compared the spatial structures to a reference pattern from reanalysis data. They found that both the simulated and observed patterns of the NAO are not stable in time over longer scales and that this variability is not related to changes in external forcings.

1.3 Aims of the thesis

Building on the results of the above mentioned studies, especially the ones from *Moore et al.* (2013) and *Raible et al.* (2014), this thesis aims at investigating the temporal and spatial changes of the North Atlantic climate variability by exploiting the output of a millennium-scale simulation of a state-of-the-art fully coupled climate model. More specifically, the prevailing research questions are:

- Is the spatial structure of the North Atlantic climate variability properly simulated by the model, compared to observations?
- How is the temporal variability of the NAO characterized in the GCM-simulation? Do we find periods of enhanced and damped low-frequency-variability in the NAO-index?
- How does the spatial structure of the North Atlantic climate variability change over time and can different regimes, dominating over longer time periods, be identified?
- Can the detected structural changes be linked to coupled processes in the climate system, e.g. to atmosphere-ocean-sea ice interactions?

These questions will be tackled by the following approach: Chapter 2 sets the theoretical background for this work, including a general description of the North Atlantic climate and the concept of teleconnections and modes of variability, the governing atmospheric processes and impacts of the NAO on the climate system. The model and the experimental setup that are used to conduct the transient simulation are presented in chapter 3, and the methods for the analysis used during the course of this work are explained in chapter 4. Chapter 5 gives a short review about the evaluation of the simulated data. Results and discussion are presented in chapter 6 and 7. Finally, a summary of the work and a short outlook about possible future research on this topic are given in chapter 8.

Chapter 2

Background and theory

The NAO is a feature of climate variability in the extra-tropical Northern Hemisphere. In order to understand the phenomenon, a short overview about extra-tropical atmospheric dynamics and climate variability is necessary.

2.1 The spatial structure of extra-tropical climate and climate variability

The atmospheric dynamics of the mid-latitudes are dominated by westerly flow and dynamic low- and high pressure systems (eddies) generated by baroclinic waves. These waves owe their existence to the spontaneous break-out of baroclinic instability which occurs in the area of strong meridional temperature gradients, e.g. at the polar front in the North Atlantic and Pacific. In the developing waves, warm sub-tropical air masses flow poleward ahead of the eastward moving surface cyclone, while cold polar air flows equatorwards behind the cyclone. This thermally indirect circulation, also referred to as the Ferrel Cell, ensures the exchange of heat and momentum between the tropical and extra-tropical regions and therefore reduces the equator-to-pole temperature gradient. This process is strongest during the cold season, as the temperature difference between the pole and the tropics is more pronounced there (e.g *Lorenz* 1967). Investigating instantaneous maps of geopotential height (Z) on the Northern Hemisphere reveals that these eddies appear in a band between 45° and 60° around the globe, typically with a wavenumber between 5 and 10 (e.g. *Blackmon and White* 1982). Because these waves are short-lived, they average out when examining long time scales.

Nevertheless, the atmosphere shows distinct wave patterns even when averaging over climatological time periods, especially in the cold season (Fig. 2.1 a). These stationary, planetary-scale waves with low-pressure troughs over north-eastern Canada and east of Asia and high-pressure ridges west of Europe and over western North America are forced by land-sea contrasts in heating and the major elevations on the Northern Hemisphere (Rocky Mountains, Greenland Ice sheet, Tibetan plateau) which alter the vorticity of the flow (see subsection 2.3.3). Although these wave patterns are geographically anchored, they change in time due to chang-

ing heating processes in the atmosphere or due to chaotic, internal processes. The amplitude and the spatial structure of the variability of the waves vary longitudinally and seasonally and are strongest over the northern oceans in boreal winter (Fig. 2.1 b) (*Hurrell and Deser* 2009).

To understand this variability, one has to consider the climatology of the jet streams. Idealized model experiments (e.g. by *Lee and Kim* (2003)) showed that a strong sub-tropical jet (e.g. in the Atlantic sector) hinders the formation of transient eddies at higher latitudes. Conversely, when the sub-tropical jet is weak, baroclinic eddies form at high latitudes and interact with the zonal-mean flow, generating a purely eddy-driven jet. Because the latitude of the transient eddies is fairly variable, the eddy-driven jet experiences a strong meridional meandering, leading to high variability in the geopotential height field. These findings are consistent with the climatology of the zonal wind at 200 hPa (approximate height of the maximum of the thermally-driven jet stream) on the Northern Hemisphere, which is shown in Fig. 2.2. The thermally driven jet stream exhibits two distinct maxima, one located eastward of Asia and the other one over eastern North America. These areas coincide with areas of low variability in the geopotential height field (Fig. 2.1 b), indicating that a strong sub-tropical jet inhibits the formation of high-latitude baroclinic eddies. In contrast, the positions of the zonal wind minima are located in the eastern North Atlantic and in the central Pacific (Fig. 2.2), which is in agreement with the high variance of the geopotential height field (Fig. 2.1 b).

2.2 Teleconnections and modes of variability

As a consequence of this transient behavior of the baroclinic waves in the eastern North Atlantic and the Pacific, climate anomalies of opposite sign occur at distant regions. For example,

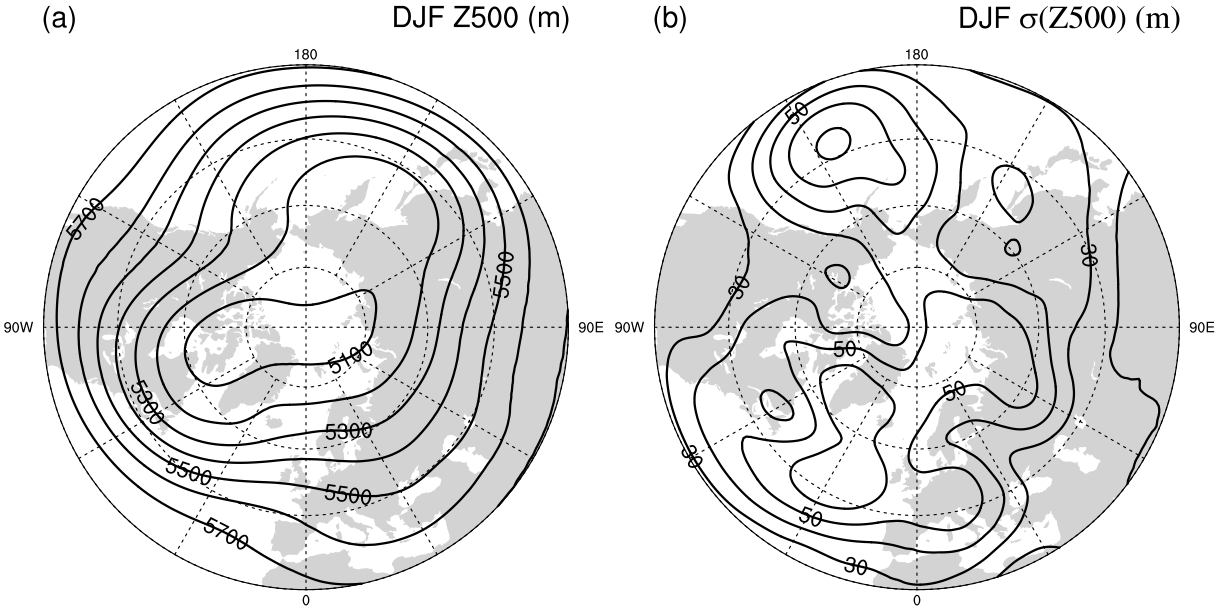

Figure 2.1: Mean winter (DJF) 500-hPa geopotential height ($Z500$) (a) and its standard deviation (σ) (b) over the Northern Hemisphere from 1979-2015, EraInterim.

Europe lies within a ridge of the wave and therefore receives warm and wet air, whereas eastern North America/Greenland exhibits colder-than-normal temperatures at the same time, as it is within a low-pressure trough (*Wallace and Gutzler* 1981). These simultaneous variations in climate over distant parts of the globe are called teleconnections, which dates back to *Ångström* (1935). When such a spatial pattern manifests a temporal behavior that can be explained by an index, it is called mode of variability (*Wallace and Gutzler* 1981).

These concepts help to simplify the rather complex large-scale atmospheric general circulation and the associated long-term climate variability. Because the atmosphere has the strongest variability in the North Pacific and North Atlantic regions in boreal winter (see section 2.1), it seems likely that the most prominent teleconnections of the Northern Hemisphere are located within these zones, which are the North Atlantic Oscillation (NAO) and the Pacific-North American (PNA) patterns. Other teleconnections in the North Atlantic region are the East Atlantic (EA) pattern, consisting of centers of action over the eastern North Atlantic near Great Britain and over the Mediterranean, and the Scandinavian (SCA) pattern, consisting of centers of action over Scandinavia, Western Europe and Eastern Russia.

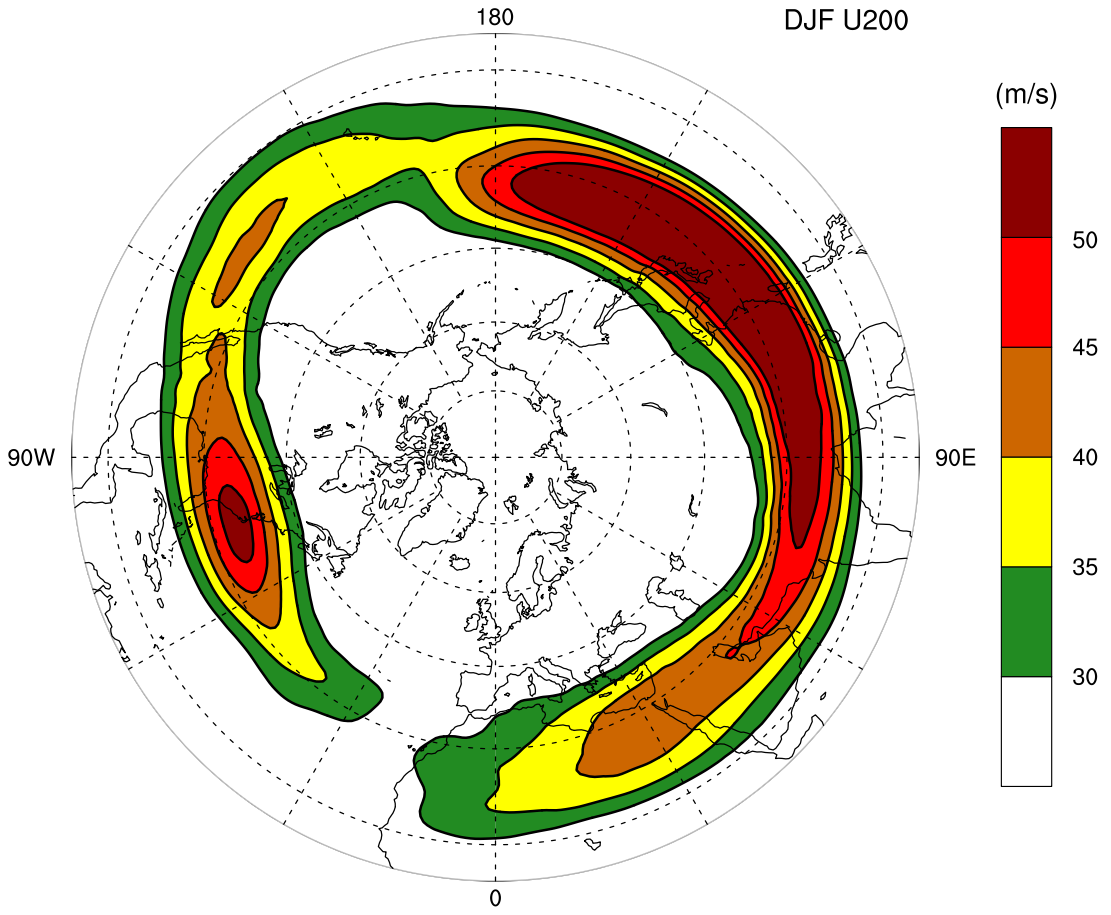

Figure 2.2: Mean winter (DJF) 200-hPa zonal wind speeds (U200) over the Northern Hemisphere from 1979-2015, EraInterim.

2.3 The North Atlantic Oscillation

The NAO is the most important mode of variability on the Northern Hemisphere in boreal winter. In the following section, the phenomenon itself, its influence on the climate system and the governing atmospheric processes will be explained in detail.

2.3.1 Description of the NAO

The NAO refers to a redistribution of atmospheric mass between the Arctic and the sub-tropical Atlantic. As a result of this spatial oscillation, two phases can statistically be described: During the positive phase (NAO+), higher-than-normal pressure is observed over the southern center of action, while lower-than-normal pressure is detected over the northern center of action, i.e., the meridional pressure gradient is enhanced. Fig. 2.3a shows such a situation which occurred in winter 2015 where a strong trough lies over the northern North Atlantic. The negative NAO-phase (NAO-) describes the opposite situation with higher-than-usual pressure over the northern center of action and lower-than-usual pressure over the southern center of action, resulting in a reduced meridional pressure gradient. Such a situation is shown in 2.3b where a so-called 'high-over-low' geopotential height field is observed in the North Atlantic region (*Wallace and Gutzler* 1981).

To describe the temporal behavior of these dynamics, different indices have been introduced. Most of them refer to a sea level pressure (SLP) difference between two representative locations for the centers of action. The commonly used station-based index for the NAO is the Hurrell North Atlantic Oscillation Index by *Hurrell* (1995) using sea level pressure measurements at Ponta Delgada (Azores) and Reykjavik (Iceland). It is defined as

$$NAOI(t) = \frac{SLP(t)_{Pde} - \overline{SLP}_{Pde}}{\sigma(SLP_{Pde})} - \frac{SLP(t)_{Rey} - \overline{SLP}_{Rey}}{\sigma(SLP_{Rey})} \tag{2.1}$$

where $\overline{SLP}$ refers to the temporal mean of the SLP and $\sigma(SLP)$ to the standard deviation. Its temporal evolution from 1864 to 2017 is shown in Fig. 2.4.

It is important to note that the NAO does not have a bimodal frequency distribution and therefore does not flip between the two phases. It rather shows a continuous transition between the two phases with no clear preferred frequencies on inter-annual to decadal time scales. The NAO can be observed year-round but is strongest during wintertime and its spatial pattern and impacts deviate strongly in the different periods of the year (*Barnston and Livezey* 1987; *Folland et al.* 2008).

2.3.2 Impacts on the climate system

The impacts of the NAO-phases on different parts of the climate system are manifold and therefore depicted highly idealized in Fig. 2.5. Only the most important ones are discussed briefly. As already described above, NAO+ shows a well-developed pressure gradient between the

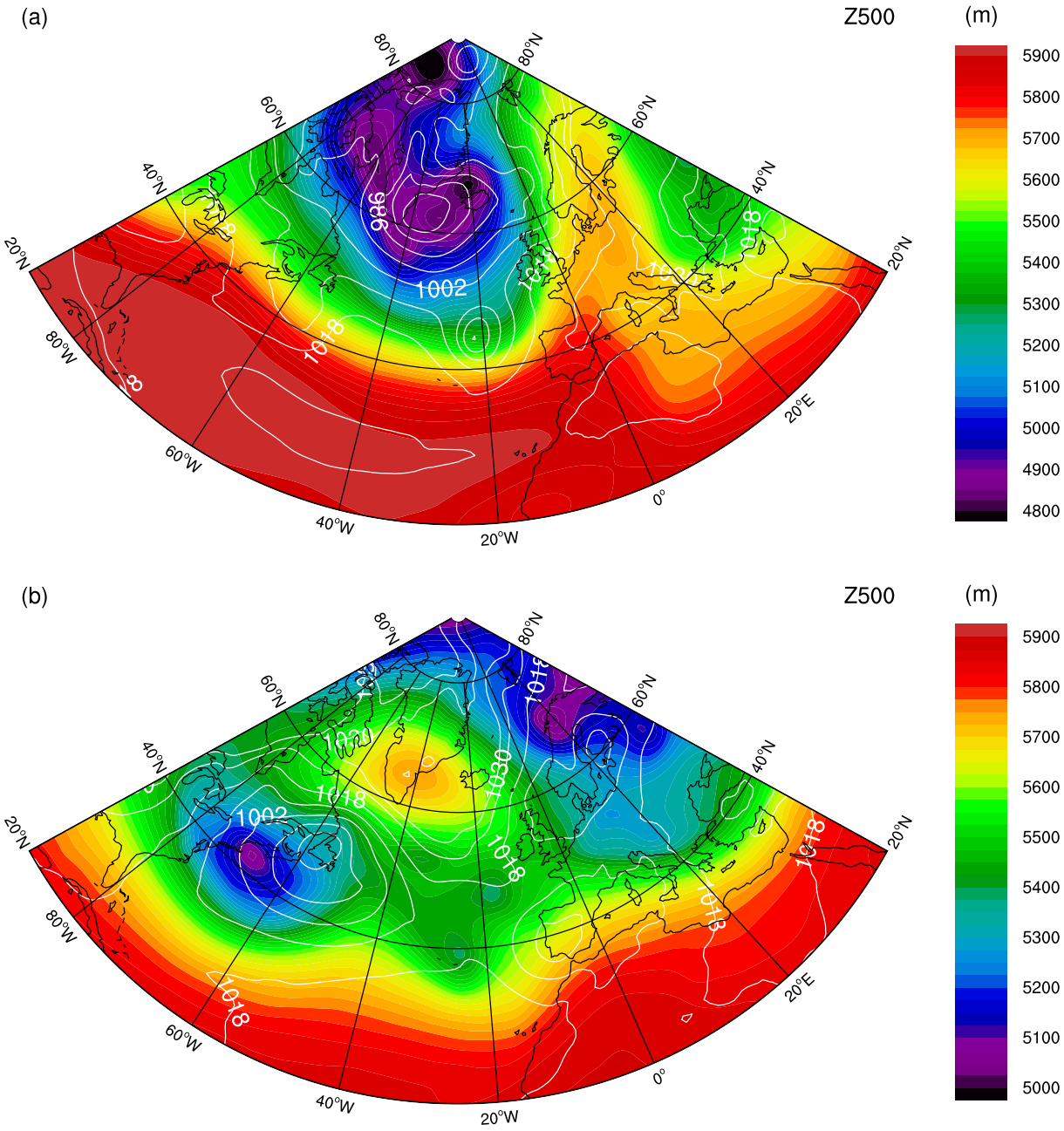

Figure 2.3: 500-hPa geopotential height (shading) and sea level pressure (white contours, the interval is 8 hPa) in the North Atlantic sector at December 30, 2015 12 UTC (a) and January 3, 2010 12 UTC (b), EraInterim.

Icelandic Low and the Azores High, which results in a strengthening and a north-eastward diversion of the westerly flow. This also deflects the storm track northwards, transporting heat and moisture to Central Europe, which leads to warmer- and wetter-than-usual conditions. For the opposite phase, converse effects are observed: The westerlies are weakened and have no meridional component, deflecting the storms southerly which enables cold-air advection from the north towards Central Europe. The Mediterranean and Northern North America experience a cooling and Northern and Central Europe and South-Eastern North America a warming during NAO+, the opposite conditions appear during NAO- (*Jones et al.* 2003).

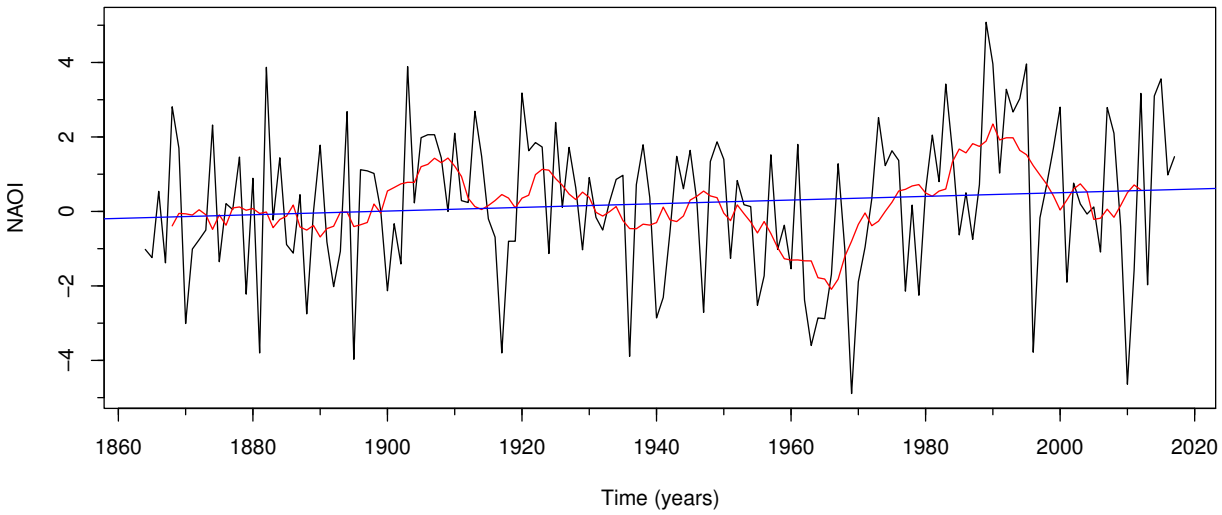

Figure 2.4: Winter (DJF) North Atlantic Oscillation Index (NAOI), calculated as the difference between normalized SLP between Ponta Delgada, Azores, and Reykjavik, Iceland (black line). The red line shows the 10-year running mean and the blue line the linear trend. The data is from *Hurrell* (2017).

It seems likely that such major temperature anomalies also affect the underlying ocean. Therefore, positive SST anomalies are found at the northern European coast and east of southern North America and negative SST anomalies are located south-east of Greenland and west of North Africa during NAO+. Again, the opposite is observed for the negative phase.

Also the large-scale ocean circulation in the North Atlantic is affected by both the temperature anomalies (thermohaline circulation), resulting in a tripole pattern of the SST, and the pressure patterns (wind-driven gyre circulation). Because of the altered ocean currents, the sea ice in the Labrador Sea is affected. During NAO+, the Labrador Sea is covered with ice which disables sea ice transport by the Transpolar Drift Stream. Conversely, when the Labrador Sea is open during NAO-, sea ice and water transport through the Fram Strait occurs (*Visbeck et al.* 2003). These major effects on the climate system also affect marine and terrestrial ecosystems and have socio-economic implications for Europe and north-eastern North America (e.g. *Drinkwater et al.* 2003; *Mysterud et al.* 2003).

2.3.3 Atmospheric processes governing the NAO

In contrast to the well known mode of variability El Niño Southern Oscillation (ENSO) which arises from coupled atmosphere-ocean dynamics (*Bjerknes* 1969), the formation of the NAO is an atmosphere-only process. As already mentioned in section 2.1, the climate variability in the North Atlantic sector arises from the stationary planetary-scale waves induced by the topography and the land-sea contrasts on the Northern Hemisphere. This is based on the law of conservation of potential vorticity (PV) under frictionless and adiabatic conditions, which can be written as

$$\frac{D}{Dt}\left[(\zeta+\beta)\left(\frac{\partial\theta}{\partial p}\right)\right]=0. \tag{2.2}$$

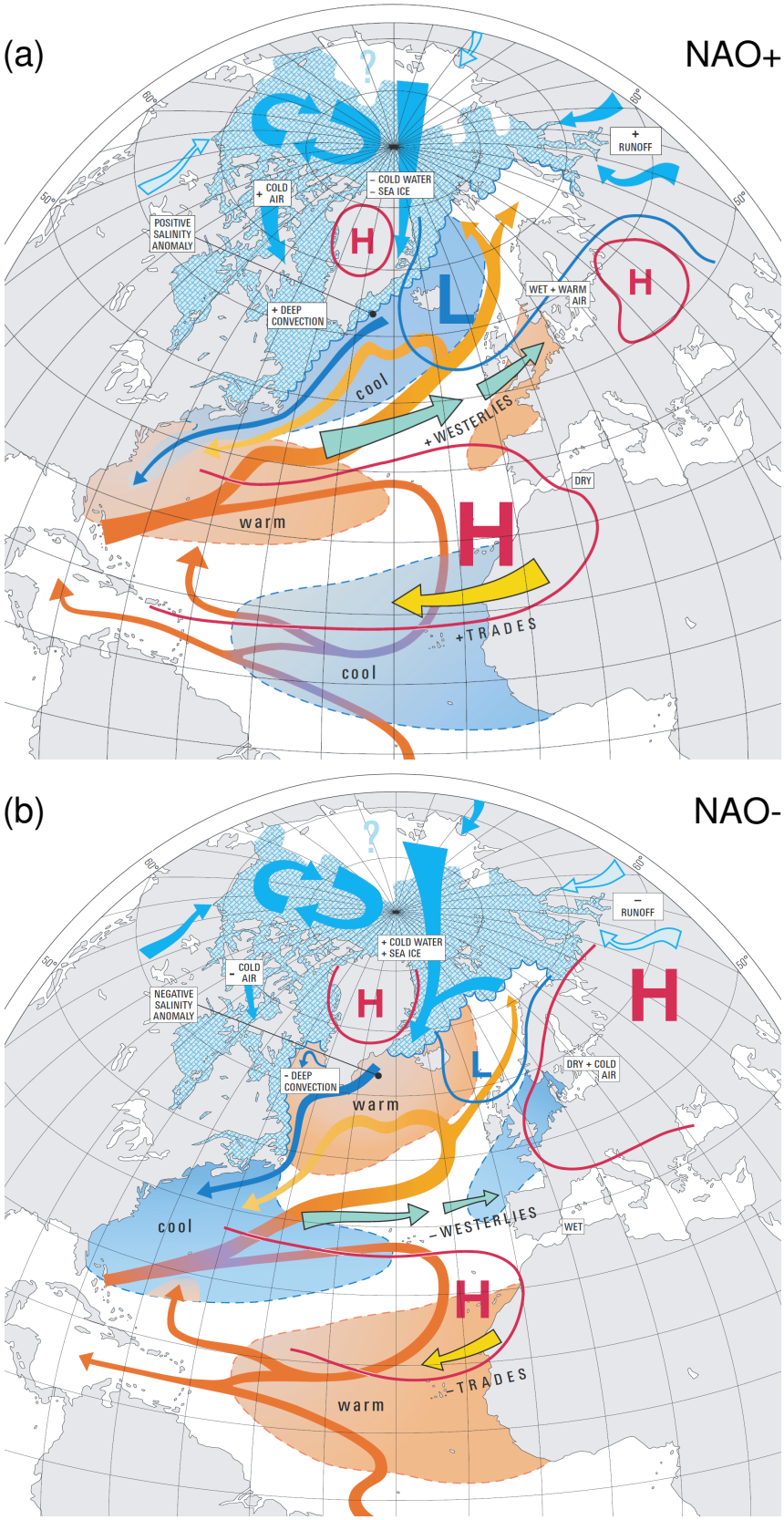

Figure 2.5: Idealized sketch of the positive (a) and negative (b) phase of the NAO and its impacts on the climate system in the North Atlantic region. Shaded surfaces indicate *SST*s and sea ice extension, arrows show flow systems in atmosphere, ocean and rivers and blue and red contours mark sea level pressures. Taken from *Wanner et al.* (2001).

$\frac{D}{Dt}$ is the material derivative, ζ is the relative vorticity, β is the planetary vorticity, and $\frac{\partial\theta}{\partial p}$ is the static stability (*Holton* 2004). As the whole term cannot be changed under adiabatic and frictionless conditions, a meridional displacement of an air parcel which changes the planetary vorticity β has to change the relative vorticity. Analogous, a change of the static stability parameter also changes the relative vorticity of an air parcel. Fig. 2.6 schematically illustrates the alteration of a zonally uniform flow over topography. Fig. 2.6a is in the $x - y$ plane and shows the meridional displacement of the flow in response to the orographic forcing. Fig. 2.6b depicts the changes of the static stability parameter and its effect on the relative vorticity as a result of the topography in the $x - p$ plane. In the setup of a purely westerly flow, both the change of the Coriolis parameter as well as the change of the static stability induce a wave downstream the mountain ridge whose amplitude decreases with increasing distance of the mountain ridge. Together with diabatic heating contrasts between the oceans and the continents which have a similar effect as topography, this leads to the wavenumber 3 pattern in the climatological Z500 field on the Northern Hemisphere (Fig. 2.1), shown in section 2.1.

By using idealized model experiments with atmosphere-only GCMs and a prescribed climatological course of the sea surface temperatures, several authors were able to simulate NAO-like variability (e.g., *Walter et al.* 2001; *Brayshaw et al.* 2009). They showed that both the topography over North America as well as the land-sea contrasts on the Northern Hemisphere are sufficient to produce a barotropic NAO-signal in the atmosphere in the North Atlantic sector. Single NAO-events like the situations shown in Fig. 2.3 originate from upper-level synoptic waves, also called Rossby waves, which are driven by transient eddy fluxes. Note that the North Atlantic area is a sector of very high transient eddy-activity, as described in section section 2.1. When these waves break, NAO-events can occur. While anticyclonic wave breaking is related to positive NAO-phase, cyclonic wave breaking is associated to the negative NAO-phase (*Feldstein* 2003; *Benedict et al.* 2004). During the events, both phases are sustained by the breaking of upstream synoptic-scale waves. When these disturbances are no longer present, the NAO-event decays by mixing processes. Both phases undergo a complete life cycle of growth and decay within approximately two weeks, but the opposite phases do not necessarily alternate (*Feldstein* 2003; *Benedict et al.* 2004).

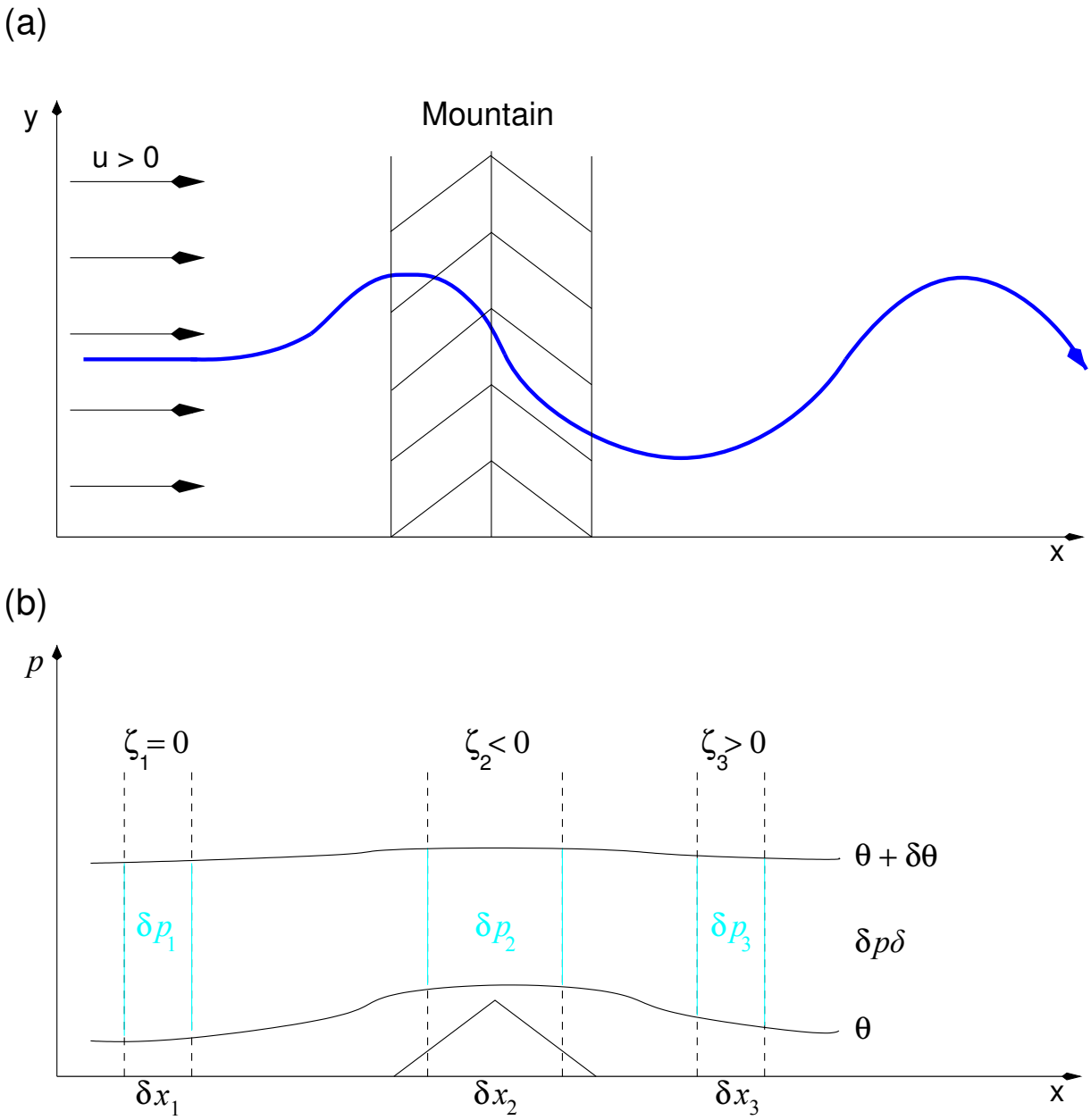

Figure 2.6: Schematic of the alteration of a uniform zonal flow by topography. (a) shows the meridional displacement of the flow in response to the mountain ridge in the $x - y$ plane, and (b) illustrates the effects of the static stability change on the relative vorticity in the $x - p$ plane. Adapted from (*Raible* 2017), originally from *Holton* (2004).

Chapter 3

Model and experimental design

3.1 Community Earth System Model (CESM)

This study is based on a transient millennial-scale simulation from 850 to 2099 AD conducted by *Lehner et al.* (2015) with the fully coupled Community Earth System Model (CESM; *Hurrell et al.* 2013) developed by the National Center for Atmospheric Research (NCAR). The version of CESM used for the simulation is release 1.0.1 and includes components for atmosphere (Community Atmosphere Model v.4 (CAM4) (*Neale et al.* 2010)), ocean (Parallel Ocean Program v.2 (POP2) (*Smith et al.* 2010)), land (Community Land Model v.4 (CLM4) (*Lawrence et al.* 2009)) and sea ice (Community Ice Code 4 (CICE4) (*Hunke and Lipscomb* 2010)), all coupled by a flux coupler (*Hurrell et al.* 2013). The model physics of CESM rely on the fourth version of the Community Climate System Model (CCSM4), the previous GCM developed by NCAR. Additionally, a carbon cycle module is included in CESM's atmosphere, ocean and land components (*Lehner et al.* 2015).

The CAM4 has a finite-volume core with a uniform horizontal resolution of 1.25° x 0.9 ° and 26 hybrid levels. It is based on the primitive equations in hydrostatic equilibrium which is a good approximation for processes with a horizontal extent larger than 10 km (*Neale et al.* 2010; *Lehner et al.* 2015).

The ocean dynamics in POP2 are described by the primitive equations for a thin stratified fluid using the hydrostatic and Boussinesq approximations. It has 60 depth levels and a nominal horizontal resolution of 1° which is slightly higher at the equator and around Greenland, to where the North Pole is displaced. It includes a biogeochemical model based on a nutrient-phytoplankton-zooplankton-detritus food web dynamics (*Smith et al.* 2010; *Lehner et al.* 2015).

The CLM4 operates on the same horizontal grid as CAM4 and includes a prognostic carbon-nitrogen cycle and a prognostic fire module (*Lawrence et al.* 2009; *Lehner et al.* 2015).

The CICE4 has the same horizontal resolution as POP2 and includes elastic viscous plastic dynamics, energy-conserving thermodynamics and a sub-grid scale ice thickness distribution

(*Hunke and Lipscomb* 2010; *Lehner et al.* 2015). For further information see *Hurrell et al.* (2013) and the references for the individual components.

3.2 Experimental design

In order to conduct the simulation from 850 to 2099 AD, first a 500-year control simulation (CTRL) with constant 850 AD forcing was branched off from an 1850 AD control simulation. A transient simulation covering the period from 850 to 2099 AD was then branched off from year 258 of the control simulation where most quantities of the surface climate were considered reasonably equilibrated at the start of the transient simulation. The applied transient forcings used in the simulation largely follow the Paleoclimate Modeling Intercomparison Project 3 (PMIP3; *Schmidt et al.* 2012) and Coupled Model Intercomparison Project 5 (CMIP5; *Taylor et al.* 2012) protocols and are shown in Fig. 3.1 (*Lehner et al.* 2015). The forcing components are:

- total solar irradiance (TSI): Variations of the solar constant due to the 11-year solar cycle and the orbital cycles. Fig. 3.1a shows the TSI reconstruction used for this simulation where it fluctuates between 1364 and 1367 Wm^{-2} (*Vieira et al.* 2010) in comparison to one large-amplitude reconstruction and the bulk of small-amplitude reconstructions of the original PMIP3 protocol (*Schmidt et al.* 2012).

- volcanic and anthropogenic aerosols: The reconstruction of *Gao et al.* (2008) provides estimates of sulfate aerosol loadings in the stratosphere from volcanic eruptions from 850 to 2001 CE (Fig. 3.1b). This is implemented into CESM as fixed single-size distribution in the three layers of the lower stratosphere (*Neale et al.* 2010). After the year 2001 the volcanic forcing remains zero (*Lehner et al.* 2015). Non-volcanic aerosols (black and organic carbon, dust and sea salt) are represented as non-time-varying up to 1850 CE. Post-1850 CE the temporal evolution of anthropogenic aerosol emissions are taken into account by using the estimate of *Lamarque et al.* (2010). Only the direct aerosol effect (scattering and absorption), but not the indirect and semi-direct aerosol effects (microphysical processes in clouds) are taken into account in CESM.

- greenhouse gases (GHG): Even though the carbon cycle module of CESM interactively calculates the CO_2-concentration changes originating from different sources (e.g. fossil-fuel emissions and carbon cycle-climate feedbacks), it is radiatively inactive. Instead, the radiative forcing of the long-lived GHGs (CO_2, CH_4 and N_2O, Fig. 3.1c) is prescribed by estimates from high-resolution Antarctic ice cores and measurements in the mid-twentieth century (*Schmidt et al.* 2012; *Lehner et al.* 2015). For the extension of the simulation post 2005 AD the Representative Concentration Pathway 8.5 (RCP 8.5) was used, representing the 'business-as-usual' emission scenario, corresponding to a forcing of approximately 8.5 Wm^{-2} by the end of the 21st century (*Moss et al.* 2010).

- land use and land use changes (LULUC): Fig. 3.1d shows LULUC reconstructions from *Pongratz et al.* (2008) and *Hurtt et al.* (2011). Global anthropogenic LULUC was small until

the industrial era where LULUC increases, mostly due to the expansion of crop land and pasture. The effects of shifting cultivation and wood harvest on carbon emissions from land use are neglected (*Lehner et al.* 2015).

For further information about the configuration of the simulation see *Lehner et al.* (2015).

The simulation has already been exploited for different research questions in the paleo-climatological community. *Lehner et al.* (2015) assessed the forcing uncertainty associated with reconstructions of the total solar irradiance and found that the differences between climate models can be

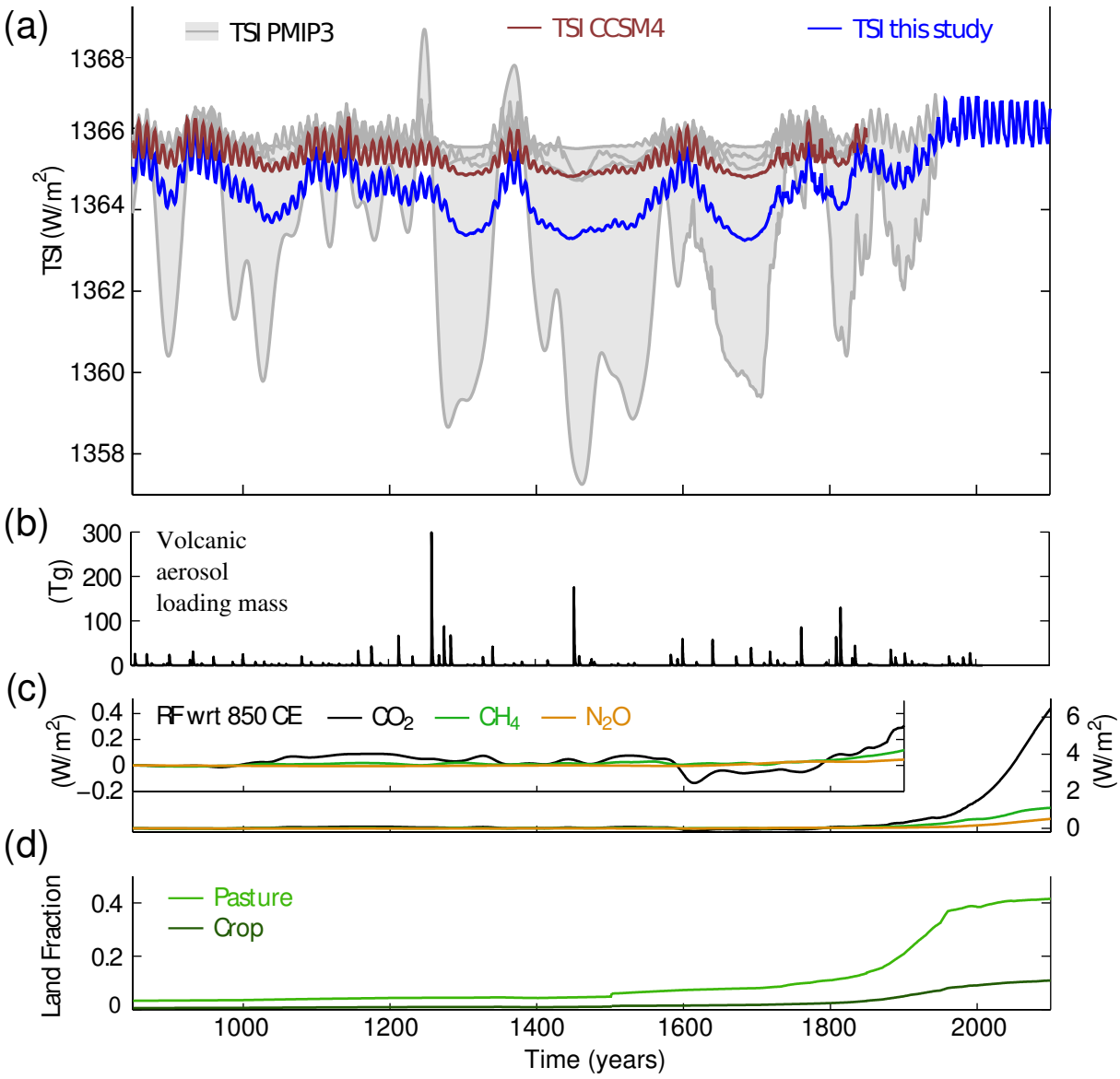

Figure 3.1: Forcings used in the last millennium simulation with CESM. (a) TSI in comparison with different TSI reconstructions proposed by PMIP3. (b) Volcanic forcing as total volcanic aerosol mass. (c) Radiative forcing from the greenhouse gases CO_2, CH_4 and N_2O. (d) Land use and land use changes. Adapted from *Lehner et al.* (2015).

higher than the forcing uncertainty for specific quantities. Further, they figured that externally forced signals may be masked by internal variability and estimated the climate-carbon-cycle sensitivity to 1.0 - 2.1 ppm $^{\circ}C^{-1}$. In another study, *Keller et al.* (2015) investigated changes in the marine responses to ENSO and focused on the ocean carbon cycle. During the Maunder Minimum (17th century), the ENSO amplitude is increased compared to the 21st century warm period, while ENSO-driven air-sea carbon flux anomalies and marine productivity are weakened. Finally, *Camenisch et al.* (2016) used the transient simulation to analyze the role of internal climate variability and external forcings in forming extreme climatic conditions, with a focus on an exceptionally cold period in the 15th century and its effects on societies. They conclude that the conditions were mainly driven by internal variability, which increased the seasonal temperature cycle and finally led to a food production reduction and famine in parts of Europe.

Chapter 4

Methods

In this chapter, the methods that are applied to tackle the research questions are introduced. The first part deals with the temporal and spatial representation of modes of variability and teleconnections. Then, we cover cluster analysis and in particular the k-means method, an approach to classify datasets statistically. Finally, a technique to analyze periodicities in a time series, the wavelet transform, is introduced.

4.1 Representation of teleconnections

As teleconnections and modes of variability are not uniquely defined, several different methods of representing their temporal and/or spatial characteristics exist. Indices calculating the pressure or geopotential height differences at two centers of action are a common way to deal with the temporal variability of teleconnections, while teleconnectivity maps give detailed spatial information about climate variability. Methods based on the Principal Component Analysis (PCA) can be used for both spatial and temporal analyses.

4.1.1 Station-based indices

One way to illustrate the temporal evolution of teleconnection patterns are station-based or grid point-based indices. A commonly used NAO-index has already been introduced in subsection 2.3.1: The Hurrell North Atlantic Oscillation Index (*Hurrell* 1995), which is defined as the difference of normalized sea level pressure between Ponta Delgada (Azores, 25.66° W, 37.75° N) and Reykjavik (Iceland, 21.93° W, 64.15° N):

$$NAOI(t) = \frac{SLP_{Pde}(t) - \overline{SLP}_{Pde}}{\sigma(SLP_{Pde})} - \frac{SLP_{Rey}(t) - \overline{SLP}_{Rey}}{\sigma(SLP_{Rey})}. \tag{4.1}$$

Note that a representative reference period needs to be chosen in order to prevent biased results. The index based on observations is calculated with the reference period 1979-2015, and the simulated index refers to the period 850-2099. Advantageous about this method is that

these indices reach back to the mid-19th century or earlier because only sea level pressure measurements at two stations are needed. The major disadvantage is that station-based indices are spatially fixed, meaning that they do not represent any spatial variability. Furthermore, single station pressure measurements are influenced by transient and small-scale meteorological events independent from the NAO and, thus, contain noise.

When dealing with gridded data, normally the closest grid cells to the coordinates of the stations are used. In this thesis, Ponta Delgada is represented by the grid cell 26.25° W, 38.17° N and Reykjavik by 22.5° W, 64.55° N.

4.1.2 Indices and maps based on Principal Component Analysis (PCA)

This section is mainly based on the textbook "*Statistical methods in the atmospheric sciences*" (*Wilks* 1995). Principal Component Analysis and Empirical Orthogonal Function (EOF) analysis are both the same statistical method which reduce a data set consisting of a large number of variables to a data set containing fewer new variables which are linear combinations of the original variables. These new variables, called Principal Components (PCs), Empirical Orthogonal Functions (EOFs) or leading eigenvectors, represent the maximum possible fraction of variability contained in the original data set. In other words, the mode of variability is split into a finite sum of several space-time modes. As atmospheric fields generally exhibit large correlations amongst each other, a PCA results in a much more condensed representation of their variations. Furthermore, a PCA can be used to analyze both spatial and temporal variations of atmospheric fields. Usually the Principal Components are calculated as linear combinations of the anomalies $x' = x - \overline{x}$ of a field. The first PC is the linear combination of x' which has the largest variance. The consecutive PCs are the linear combinations with the subsequent largest variances, provided that they are uncorrelated with the PCs with lower order. The PCs are uniquely defined by the eigenvectors of the covariance matrix $[S]$ or the correlation matrix $[R]$ of the original data. In particular, the m_{th} PC, u_m, is obtained by projecting the anomaly vector x' onto the m_{th} eigenvector e_m of $[S]$,

$$u_m = e_m^T x' = \sum_{k=1}^{K} e_{km}^T x'_k, \quad m = 1, ..., M. \tag{4.2}$$

Note that if the original data x is a time series, then the PCs are also time series. Each PC represents a fraction of the total variation (R^2) in the original dataset that is proportional to its eigenvalue λ_m,

$$R_m^2 = \frac{\lambda_m}{\sum_{k=1}^{K} \lambda_k}. \tag{4.3}$$

When PCA is applied to an atmospheric field with K grid points, each eigenvector also contains K elements which have a one-to-one correspondence with the K locations from which the corresponding PC is calculated. Each eigenvector element e_{km} can be plotted on a map at the same location as its corresponding data value x'_k. This map then depicts which locations are

contributing most strongly to the respective PC. These geographic patterns of the eigenvectors indicate the spatial distribution of simultaneous data anomalies and can be interpreted as representations of uncorrelated modes of variability of the original data field. Interpretations like that, especially with PCs of higher order, have to be handled with care as often no physical process can be found behind the patterns. Also the time series of the PCs are useful when studying teleconnections as they serve as an alternative way to produce indices.

When applying this method to sea level pressure data in the North Atlantic sector (20-80° N, 70° W - 40° E), then the leading eigenvector represents the NAO. Fig. 4.1a shows the spatial pattern of the leading eigenvector of a PCA applied to the winter (DJF) *SLP* field from 1979 to 2015 in the Atlantic sector which clearly shows the two centers of action over Iceland/Scandinavia and over the central North Atlantic. This mode of variability explains 53.1% of the *SLP* variance in the Atlantic sector. Fig. 4.1b shows the time series of the leading PC, which is highly correlated with the station-based index (cor = 0.88 for the DJF-indices of the period 1899-2017, data taken from *Hurrell* (2017)) and therefore serves as alternative NAO-index.

4.1.3 Teleconnectivity maps

Another approach to visualize teleconnection patterns is to compute the correlation matrix R whose elements $r_{i,j}$ are the temporal correlation coefficients between any selected grid point (with subscript i) and every other grid point (with subscript j) of a meteorological field (e.g. *SLP* or *Z*500). The columns of R, R_i, can then be displayed in the form of one-point correlation maps. Areas with strong anti-correlations denote areas that vary counter-cyclical with respect to the grid point i and therefore indicate a teleconnection.

To merge the information of the strongest teleconnections from i one-point correlation maps into one map, the correlation matrix R can be used to calculate the teleconnectivity matrix T,

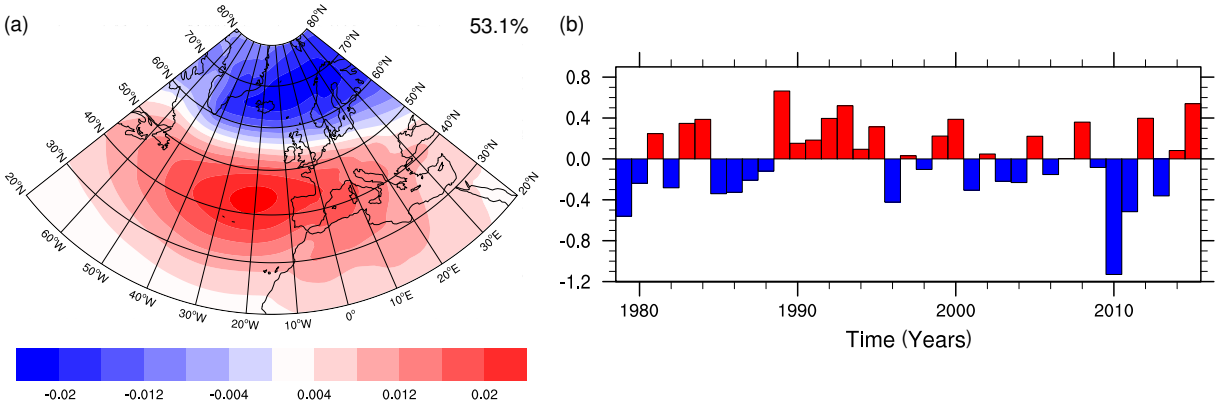

Figure 4.1: Leading eigenvector (a) and the time series of the first PC (b) of the winter (DJF) mean sea level pressure (*SLP*) over the North Atlantic sector (70° W - 40° E, 20-80° N), calculated with EraInterim data from 1979-2015. The fraction of variance explained by the leading eigenvector is 53.1%.

whose elements T_i are the strongest negative values of $r(i,j)$ in the ith column of R:

$$T_i = min(r_{i,j}) \quad \text{for all } j. \tag{4.4}$$

For additional information, the strongest centers of teleconnectivity are connected with the grid points with which they show the strongest negative correlation by teleconnectivity axes (*Wallace and Gutzler* 1981). The algorithm determining the local minima works as follows: At each grid point (i,j), the neighboring grid points $i \pm 6, j \pm 6$ are inquired whether they contain a smaller value than the grid point (i,j). If there is at least one point with a smaller teleconnectivity, it is passed over to the next grid point $(i+1, j+1)$. If no smaller value is found within the neighboring $i, j \pm 6$ grid points, the teleconnectivity at point (i,j) has to be lower than a specified threshold in order to be considered as a minimum. The selection of the threshold has to be done manually, as the teleconnectivity values are sensitive to the selected time period and the region. By carefully evaluating single teleconnectivity maps, the threshold of $T = -0.7$ has been chosen as minimum criterion.

4.2 Cluster analysis

Cluster analysis is a method to group data into subsets (or clusters) by 'objective' statistical criteria. It aims at dividing a large group of data into smaller groups so that the data within each group possesses the same characteristics, and the data in different groups are dissimilar. Clustering is applied in many disciplines of meteorology and climatology, especially for the classification of weather types. There exist many different clustering techniques and the selection of the method is crucial as they differ strongly.

Hierarchical clustering methods seek to classify data by building a hierarchy of clusters where the statistical distance between objects within a cluster is smaller than the statistical distance between objects of different clusters. Non-hierarchical clustering techniques are designed to group items, rather than variables, into a collection of several clusters. For the widely used K-means method, the number of clusters (K) has to be specified in advance. Because the distance matrix does not have to be determined and the basic data does not have to be stored during the calculation, non-hierarchical methods need less computation time and are therefore more suitable for large datasets than hierarchical methods (*Wilks* 1995).

The K-means method is one of the most commonly used clustering tools in the atmospheric sciences and is presented in more detail because it is used to classify teleconnectivity regimes. As already mentioned, the K-means algorithm requires a prior selection of the number of clusters K. Each data point is then assigned to the cluster whose mean yields the least within-cluster sum of squares. Then, the centroids of the clusters are updated by calculating the new means of each cluster, which also minimizes the within-cluster sum of squares. This procedure is repeated until the assignments no longer change. The final assignment of items to clusters depends on the initial selection of K and of the seed points. Two common seed point selection

methods are the 'Forgy' technique which randomly chooses K objects from the data set, and the Random Partitioning method which first randomly assigns a cluster to each data point and then computes the initial centroids as the means of the clusters' randomly assigned points. The K-means clustering is computed with the PAM (Partitioning Around Medoids) -algorithm of the package 'Cluster: Finding Groups in Data' (*Maechler et al.* 2017) in R. It is a more robust version of the standard K-means algorithm as it minimizes a sum of dissimilarities instead of a sum of squared euclidean distances (*Kaufman and Rousseeuw* 1990).

The selection of the appropriate amount of clusters is very important and strongly depends on the physical process that is investigated. In general, increasing K will always reduce the error in the resulting clustering. For example, when K is equal to the number of data points, each point will have its own cluster, where the error is zero. On the other hand, clustering aims at reducing the complexity of the data set and interpretations get more difficult with increasing K. Therefore, a balance between maximum data compression and maximum clustering accuracy has to be found (*Kaufman and Rousseeuw* 1990).

There exist many different measures to determine the quality of the classification, which normally assess the separation of the different clusters. In this thesis, two measures are applied. The Explained Variation (EV), defined as

$$EV = 1 - \frac{ss_i}{ss_t}, \tag{4.5}$$

describes the ratio between the sum of squares within the clusters (ss_i)

$$ss_i = \sum_{k=1}^{K} \sum_{i=1}^{n} (x_{i,k} - \overline{x}_k)^2, \tag{4.6}$$

and the total sum of squares (ss_t), being

$$ss_t = \sum_{i=1}^{n} (x_i - \overline{x})^2, . \tag{4.7}$$

When EV = 1, no variance is lost by the clustering method. The higher EV, the better is the separation of the clusters and therefore the quality of the classification.

The silhouette value of a data point x is a measure of how similar x is to the cluster K to which it is assigned to, compared to the other clusters. Ranging from -1 to 1, values close to 1 indicate that the object is well matched to its own cluster and badly matched to the neighboring ones, while negative values mean that the object was classified into the wrong cluster. The mean of the silhouette values of all data points n is referred to as Silhouette Index (SI) and is defined as

$$SI = \frac{1}{n} \sum_{i=1}^{n} \frac{b_i - a_i}{max(a_i, b_i)}, \tag{4.8}$$

where a_i is the average distance between the data point i and all other data points in the same cluster and b_i is the average distance between the data point i and all data points in the closest neighboring cluster. Again, SI ranges between -1 and 1, where values close to 1 indicate an appropriate number of K, and low or even negative values show that the number of clusters is inappropriate (*Rousseeuw* 1987).

To decide how many clusters are appropriate, EV is plotted against the number of clusters. If there is a distinct global maximum at a relatively low number of clusters, one can choose the associated K. But normally, EV increases with K, which makes the decision more complicated. One strategy is the so-called 'elbow method' where K is chosen at the point where an additional cluster does not add much further information. Then, the selection can be reviewed with SI and the Silhouette-plot which indicates if data points have been classified wrongly.

4.3 Wavelet transform

Originally developed for signal and image processing, wavelet transform (WT) has recently been used to analyze time series in different disciplines. With this tool, multi-scale, non-stationary processes occurring over finite spatial and temporal domains can be described (*Lau and Weng* 1995). In contrast to the traditional Fourier transform, which splits the time series into a series of sine waves of different frequencies and therefore is only able to identify spectral components, the wavelet transform splits the signal into its wavelets, allowing for a time scale presentation. Wavelets are generalized local base functions that can be stretched and translated in both frequency and time.

Mathematically, wavelet transforms decompose a signal $s(t)$ into elementary functions (wavelets) derived from the dilatation and translation of a 'mother wavelet' which should have a similar pattern as the signal being analyzed. A wavelet transform can be expressed as:

$$W(a,b) = \frac{1}{\sqrt{a}} \int s(t)\psi\left(\frac{t-b}{a}\right) dt, \tag{4.9}$$

where W is the wavelet coefficient, a and b are scale (dilation) and position (translation) functions, respectively, $s(t)$ the signal depending on time and ψ the wavelet function. For the atmospheric sciences, the Morlet wavelet has been proven to be an appropriate mother wavelet (*Domingues et al.* 2005). It is defined as:

$$\psi(t) = \pi^{-\frac{1}{4}}(e^{i\xi t} - e^{\frac{\xi^2}{2}})e^{-\frac{t^2}{2}}, \tag{4.10}$$

with ξ being a dimensionless number, which is commonly set to 5.

With a visualization of the wavelet power spectrum (WPS), it is possible to display the amplitude of the wavelet plotted against the frequency, and the variation with time by changing the

wavelet time scale and translating the scaled wavelets (*Lau and Weng* 1995; *Torrence and Compo* 1998). In other words, by applying wavelet transform to a time series, one can detect periods in which the temporal evolution of the signal follows specific periodicities, denoted by high amplitudes in the corresponding frequencies. Employing this method to the NAO-index, one can find periods of enhanced or reduced low-frequency variability.

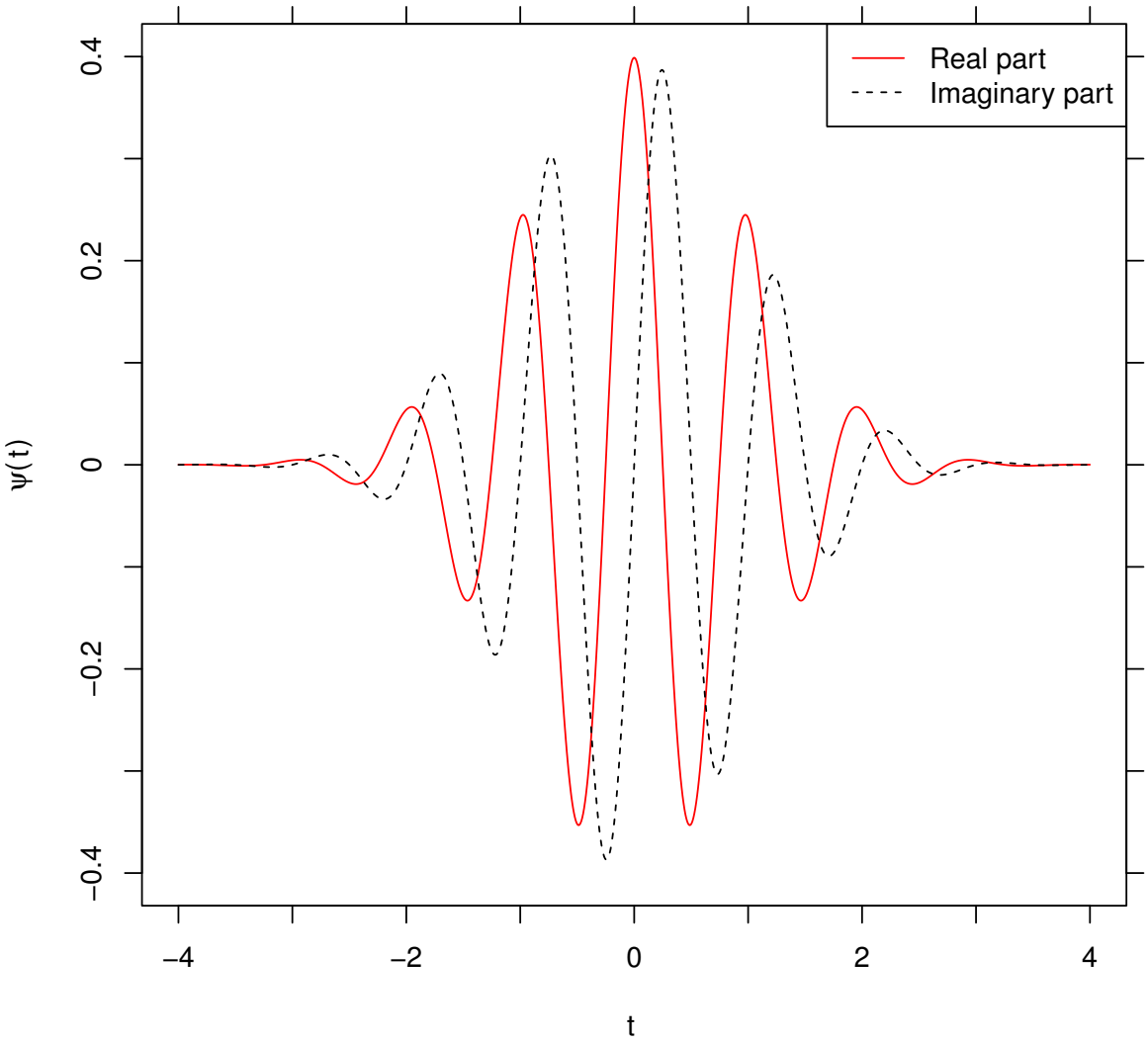

Figure 4.2: Graph of the real (red line) and imaginary (dashed line) part of the Morlet mother-wavelet $\psi(t)$, given in equation 4.10.

Chapter 5

Model evaluation

In this chapter, the transient CESM simulation used in the thesis is evaluated on different temporal and spatial scales. The North Atlantic climate variability acts on the regional scale, but is also connected to large-scale processes on hemispheric scales (e.g. Rossby waves). As the climate variability in the North Atlantic/European region is analyzed in the framework of the last millennium, a short assessment of the long-term climate evolution is given, using the Northern Hemisphere surface air temperature (SAT) with reference to proxy reconstructions and CMIP5 results. Then, climatologies of basic variables, such as temperature, geopotential height or wind speed, are compared to reanalysis data (EraInterim 1979-2015), because the teleconnectivity analysis in section 6.2 is based on 30-year periods. Lastly, the North Atlantic teleconnections from CESM are compared to the ones calculated from EraInterim in order to review whether the simulated climate variability is realistic.

5.1 Long-term climate evolution: Comparison between the model and proxy reconstructions

The following comparison of the simulated Northern Hemisphere surface air temperature (SAT) with proxy reconstructions is taken from *Lehner et al.* (2015). The evolution of SAT over the last millennium in the models CESM, CCSM4, IPSL-CM5-LR and MPI-ESM (colored lines) is drawn in Fig. 5.1 (*Lehner et al.* 2015). It further shows the 5-95% PMIP3 range and the proxy reconstructions from the IPCC-report, and the 5-95% range of the CMIP5 projections for the 21st century under the RCP 8.5 scenario. In general, the CESM simulation shows a good agreement with reconstructions and the multi-model range: The three major climate anomalies in the last millennium, the Medieval Climate Anomaly (MCA, ∼950-1250 CE), the Little Ice Age (LIA, ∼1400-1700 CE) and the anthropogenically driven warming since the beginning of the industrial era are present in the simulation. The warming from 1850-2010 is overestimated compared to observations (HadCRUT4, black line), which is most likely due to the missing of the indirect aerosol effect. The transition of MCA to LIA amounts a cooling of 0.26 K, while the reconstructed amplitudes range between 0.1 and 0.7 K. The start of LIA is triggered by a combination of decreasing TSI and a sequence of strong volcanic eruptions in CESM. During

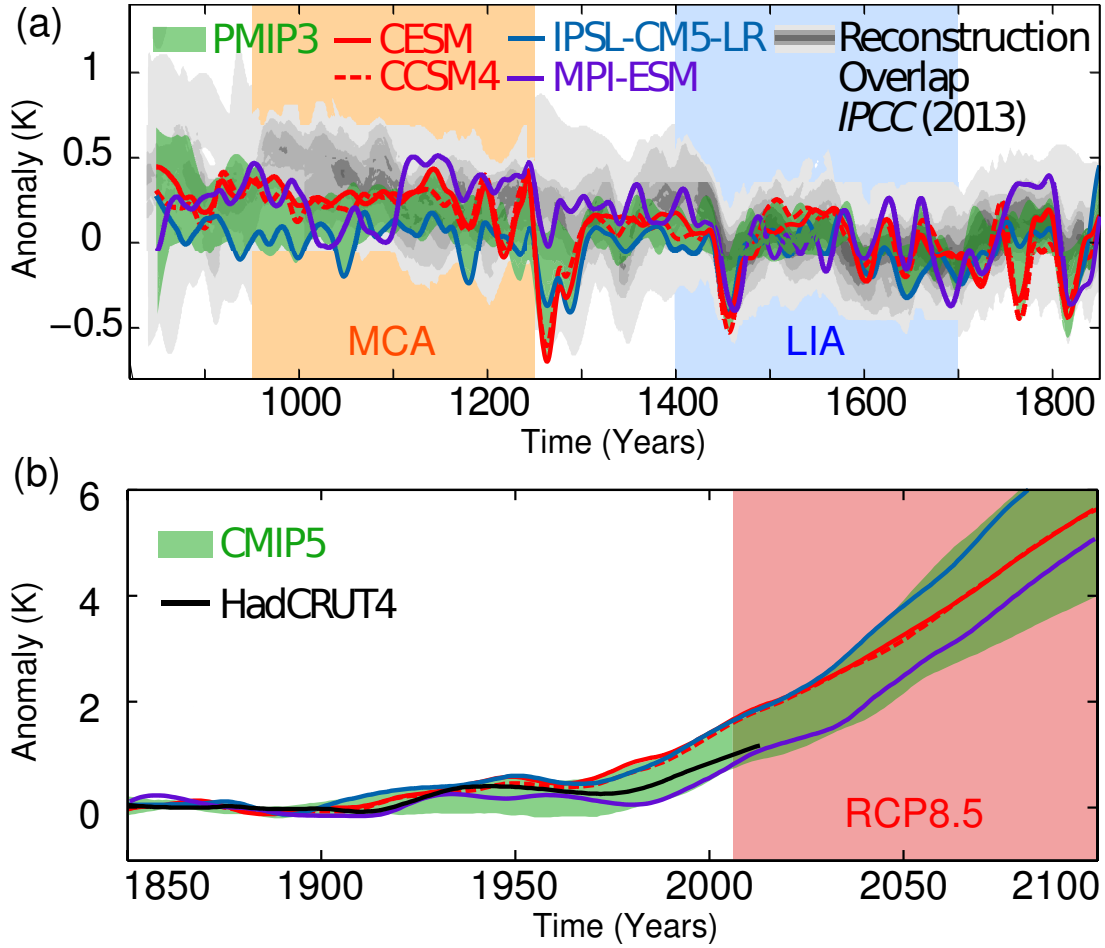

Figure 5.1: Northern Hemisphere surface temperature (SAT) anomalies in simulations of the coupled GCMs CESM (red), CCSM4 (red dashed), IPSL-CM5-LR (light blue) and MPI-ESM (dark blue), reconstructions (gray shaded) and the 5-95% PMIP3 range (a). The black line in (b) indicates observations (HadCRUT4), the green range the 5-95% CMIP5 projections under RCP 8.5 conditions. The anomalies are calculated with reference to 1500-1899 (a) and 1850-1899 (b). Adapted from (*Lehner et al.* 2015).

LIA, the different models show a better agreement than during MCA, and the magnitude of the response to major volcanic eruptions is different (e.g. in the year 1257).

5.2 Comparison to EraInterim data (1979-2015)

For evaluation purposes, the EraInterim global atmospheric reanalysis by the European Centre for Medium-Range Weather Forecasts (ECMWF; *Dee et al.* 2011) is used. This reanalysis is produced with a sequential data assimilation scheme using 12-hourly analysis cycles, where available observations are combined with prior information from a forecasting model. By using this combination, it is possible to obtain information from locally observed parameters to unobserved parameters and to carry this information forward in time. Thus, the data assimilation produces a coherent record of the global atmosphere constrained by the observations available during the period of reanalysis. Starting from 1979 and continuing to be updated forward in near-real time, a large variety of surface and upper-level parameters with a horizontal

resolution of 0.75° on 60 vertical levels is available (*Dee et al.* 2011).

5.2.1 Basic climate variables

At first, the basic climate variables temperature (T), precipitation (RR), sea level pressure (SLP), geopotential height at 500 hPa ($Z500$) and zonal (U) and meridional winds (V) shall be evaluated with a focus on the extra-tropical Northern Hemisphere.

Temperature and precipitation

CESM 850-hPa temperature (T850) and precipitation rate climatologies and their deviations from EraInterim are depicted in Fig. 5.2. The CESM temperature climatology (Fig.5.2a) shows a warm belt within the tropics with highest temperatures over the African continent and the Arabic Peninsula, a baroclinic transition zone between the sub-tropics and the sub-polar regions which is stronger on the Southern Hemisphere, and the cold polar regions. Fig. 5.2b indicates that CESM overestimates continental temperatures at middle and high latitudes on the Northern Hemisphere. At low latitudes, both datasets agree except for single regions (e.g., in the tropical Pacific and in parts of the Sahara and Arabia).

The highest precipitation values in the CESM data (Fig. 5.2c) are found in the inner-tropics, induced by strong convection associated with the ITCZ, and upstream of the major mountain ranges (Himalayas, Andes, Rocky Mountains). In the baroclinic zones of the Northern (North Atlantic and Pacific) and Southern Hemisphere high amounts of precipitation come along with extra-tropical cyclones. The subtropics, especially the Sahara and the oceanic regions on the western sides of the continents, are very dry due to subsiding air masses linked to the Hadley circulation. The brownish colors in Fig. 5.2d indicate that CESM underestimates the precipitation rates in most of the regions of the globe, mainly in the areas with high precipitation rates (inner-tropics, mid-latitudes). In the dry areas of the globe, the estimates of CESM are closer to the EraInterim data.

Sea level pressure and geopotential height

The CESM SLP climatology (Fig. 5.3a) features a zone of low pressure between 25° N/S associated with the ITCZ and a belt of high pressure in the subtropics with highest magnitudes in the Atlantic and Pacific regions and over the Tibetan Plateau. Low pressures are found in a small sector in the North Atlantic as well as everywhere south of 60° S. CESM overestimates the pressure in most parts of the band between 10°-50° N, but underestimates it at high latitudes, especially in the northern North Atlantic (Fig. 5.3b). The pressure gradient between the Azores High and the Icelandic Low is therefore strongly increased (by about 20 hPa), resulting in stronger-than-observed westerly winds (Fig. 5.4). This bias is equivalent to the positive NAO-phase, when the normalization is performed with EraInterim data. Fig. 5.3c shows the CESM $Z500$ climatology with a broad area of highest values within the tropics, a transition zone where the height quickly decreases between 30 and 60° N/S and the polar region with

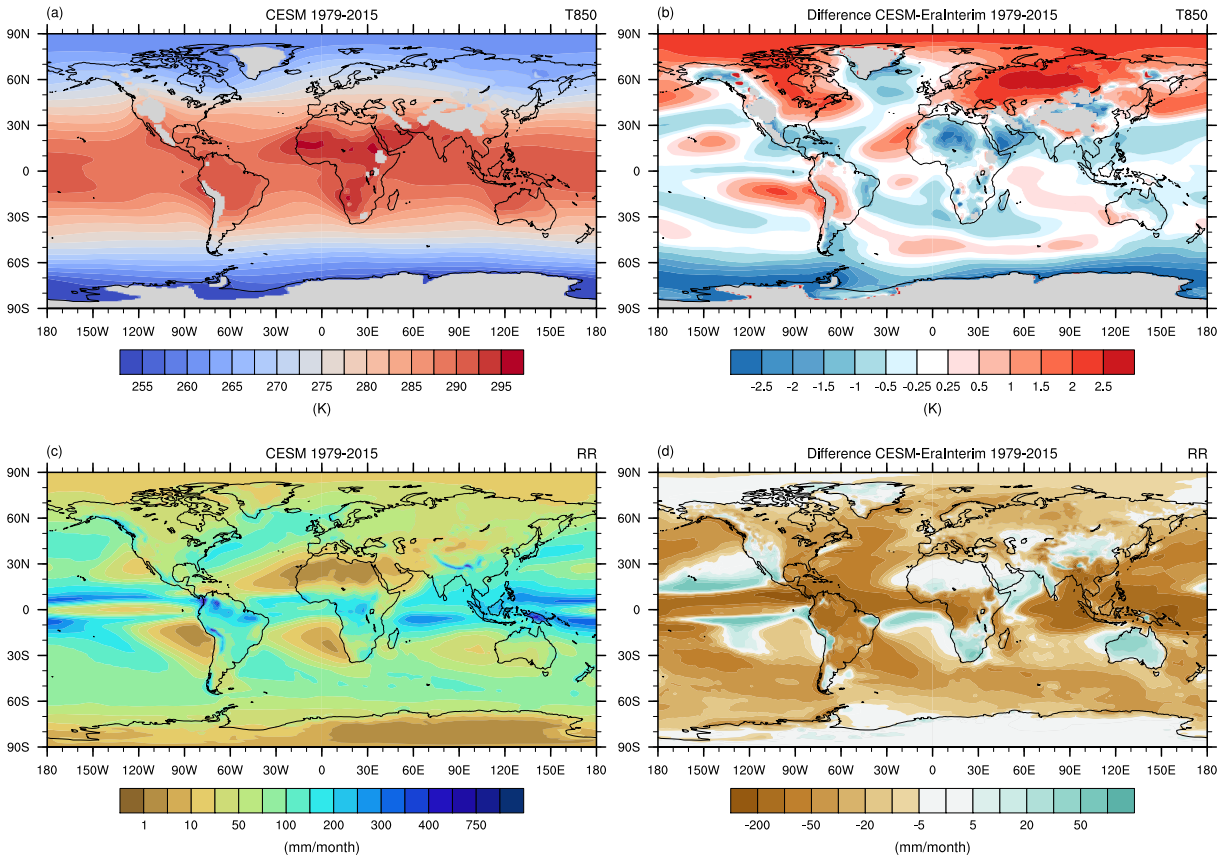

Figure 5.2: 850-hPa temperature (T850) climatology from 1979-2015 from CESM (a) and its difference with EraInterim (b), and total (convective and large-scale) rain rate (RR, mm/month) climatology from 1979-2015 from CESM (c) and its difference with EraInterim (d).

lowest heights. Fig. 5.3d indicates a rather strong systematic bias (100-200 m) of CESM Z500 relative to the EraInterim data almost everywhere. It is strongest in the northern and southern mid-latitudes and slightly weakened in the northern Euro-Atlantic zone. As Z500 and the sea level pressure depend on each other, this matches the increased pressure gradient in this sector. Systematic Z500 errors in the extra-tropics occur in most CMIP5 models, but can have different signs (*Davini and D'Andrea* 2016).

Zonal and meridional flow

The mean zonal wind at 850 hPa (*U*850) from 1979-2015 from CESM in Fig. 5.4a depicts the major zonal wind features, namely the westerlies in the mid-latitudes and the easterlies at low latitudes. In the tropics negative values indicate the trade winds blowing from east to west with strongest magnitudes over the Pacific and in the Caribbean Sea. The extra-tropics are dominated by the westerlies which are very strong on the Southern Hemisphere and weaker on the Northern Hemisphere, where the highest values are found in the storm track areas in the North Atlantic and the North Pacific. Generally, the wind speed is larger over the oceans than over the continents due to surface friction. Fig. 5.4b shows the difference between CESM and EraInterim zonal wind speeds. CESM is biased towards stronger zonal motion in the mid-latitudes, especially in the Atlantic and Pacific storm track regions. This matches the overestimation of

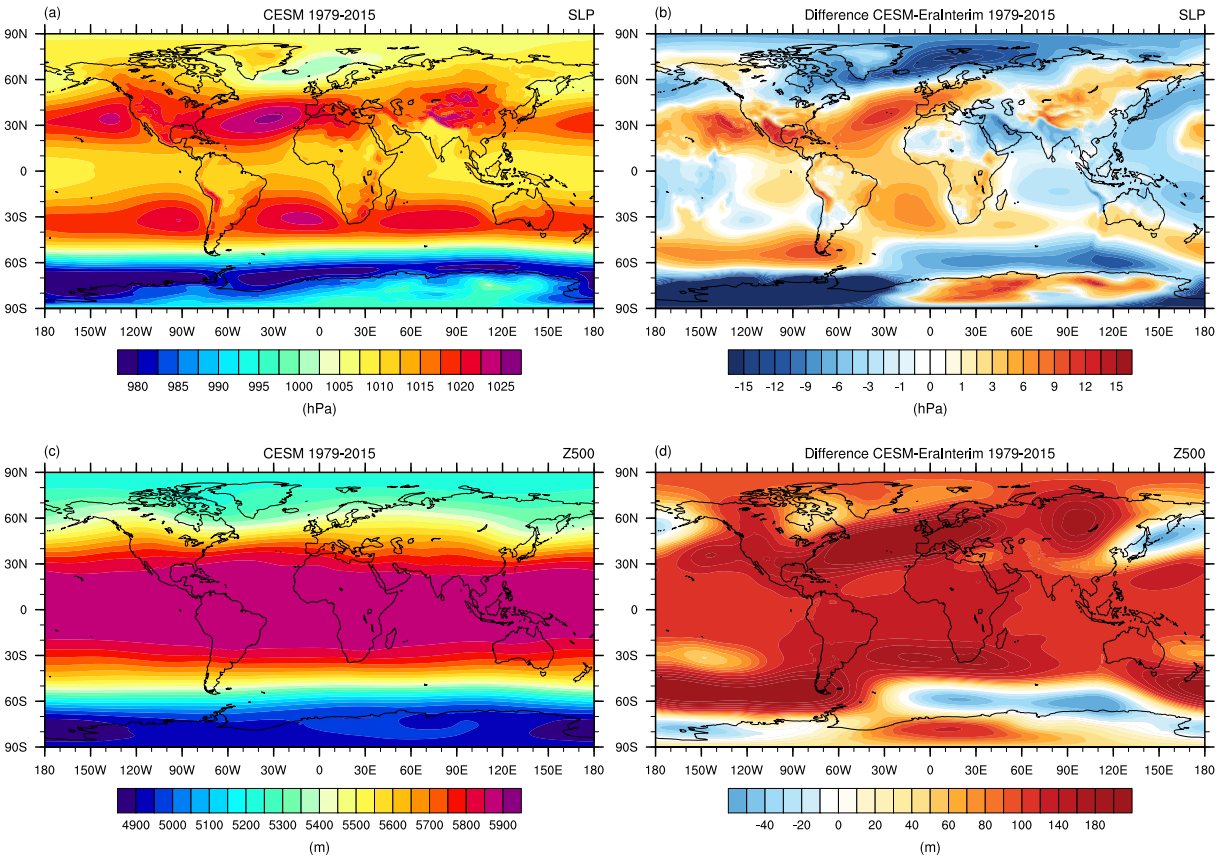

Figure 5.3: *SLP* climatology from 1979-2015 from CESM (a) and its difference with EraInterim (b), and the *Z*500 climatology from 1979-2015 from CESM (c) and its difference with EraInterim (d).

the North Atlantic pressure gradient as well as the systematic *Z*500 bias. The generally too zonal winds in the mid-latitudes are a phenomenon which is present in most CMIP5 climate models (*Davini and D'Andrea* 2016). It is likely linked to the underrepresentation of atmospheric blockings (persistent high-pressure systems deflecting the mean westerly flow), especially in the Euro-Atlantic region, in most climate models. Because the negative phase of the NAO corresponds to a blocking event in the North Atlantic sector, most climate models also suffer from a biased representation of the NAO (*Davini and D'Andrea* 2016).

The mean meridional wind at 850 hPa ($V850$) is shown in Fig. 5.4c. In both CESM and EraInterim, the southerly (northerly) flow in the northern (southern) part of the tropics representing the meridional part of the trade wind circulation are well depicted, whereas the magnitude is slightly larger in the EraInterim data. The differences between the two datasets are small and limited to a few areas, e.g., the western tropical Atlantic and the eastern tropical and subtropical Pacific (Fig. 5.4d). Especially in the North Atlantic, the differences are marginal. Note that both zonal and meridional wind speeds are not displayed in areas where elevations are higher than the chosen pressure level (shaded in gray).

To get insight into the vertical profile of horizontal wind speeds, zonal-mean patterns in the $y-z$-plane are presented in Fig. 5.5. Fig. 5.5a shows the zonal-mean zonal wind ($[U]$) in win-

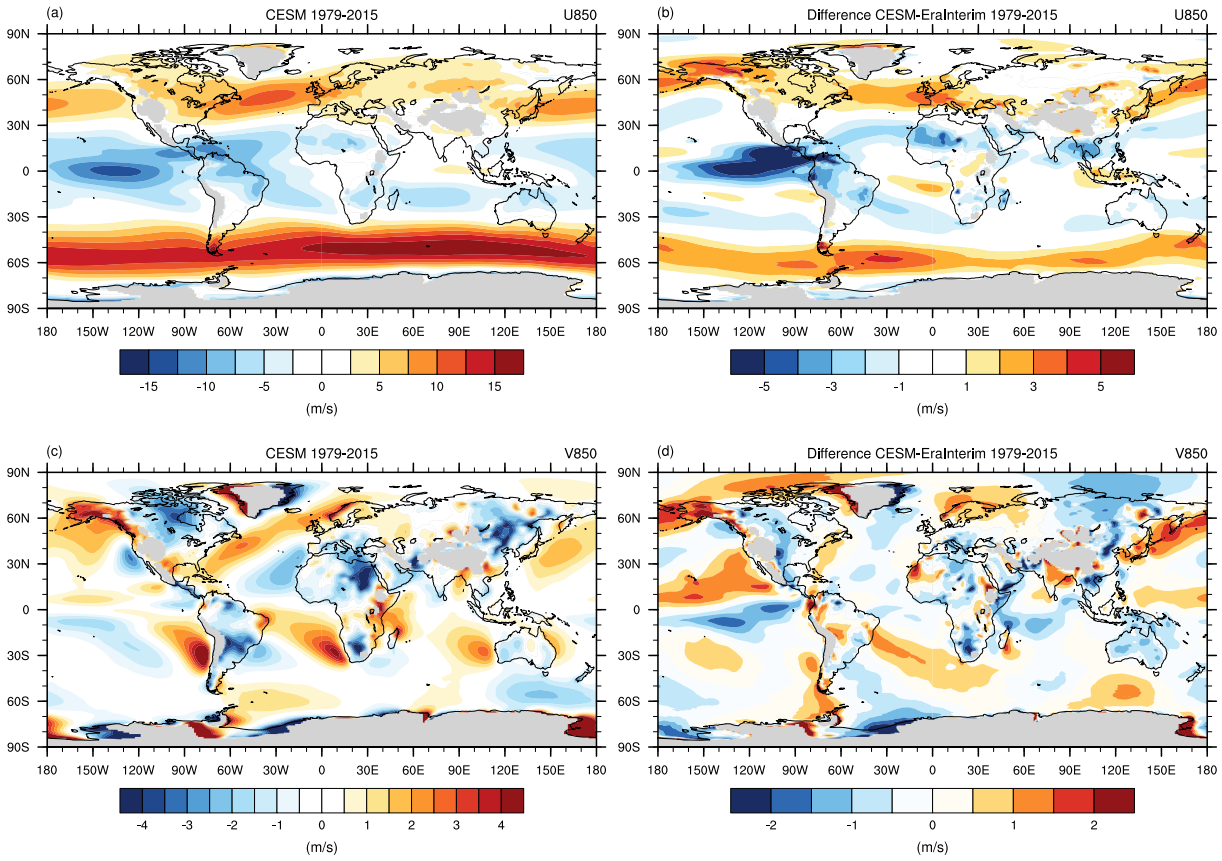

Figure 5.4: Mean 850-hPa zonal wind (U850) climatology from 1979-2015 from CESM (a) and its difference with EraInterim (b), and the mean 850-hPa meridional wind (V850) climatology from 1979-2015 from CESM (c) and its difference with EraInterim (d). Grey shaded areas display elevations higher than the chosen pressure level (850 hPa).

ter from CESM, averaged over the period 1979-2015. The two maxima at 200 hPa and 30° N and 50° S, respectively, are the subtropical jet streams which form as a result of the thermal wind balance. Because of the stronger temperature gradient on the Northern Hemisphere in boreal winter, the jet is more intense on the Northern Hemisphere than on the Southern Hemisphere. The southward shifted position of the jet pair is due to the migration of the ITCZ. The eddy-driven jet, typically located around 60° N/S, cannot be seen in this figure as it is too variable in space and time and therefore averages out. The weak negative values within the tropics are the zonal part of the trade winds, flowing equator-westwards. The strongest discrepancies between CESM and EraInterim regarding the zonal-mean zonal wind are at very high altitudes, mostly in the stratosphere (Fig. 5.5b). Both subtropical jet streams are underestimated, whereas most of the mid-latitudinal westerly flow is too strong throughout the depth of the troposphere and lower stratosphere. This highlights that the 'too zonal' character of the extra-tropical motion is not restricted to the lower-level wind only, but is present at all heights.

The vertical profile of the winter (DJF) zonal-mean meridional wind speed ($[V]$, Fig. 5.5c) is dominated by two well defined circulation cells, namely the Hadley Cell in the tropics and the Ferrel Cell in the mid-latitudes. In the tropics, the trade winds blow equator-wards into

the ITCZ, forcing the air to rise. When reaching the tropopause, the flow diverges poleward. With increasing velocity and the more poleward position (at ca. 10°), the westward deflection by the Coriolis Force intensifies, for which reason the meridional transport is blocked. At ca. 30°, the air subsides and closes the circulation. The Ferrel Cell in the mid-latitudes is driven by transient eddies and allows for a meridional heat transport between the subtropics and the mid-latitudes. At the surface between 30 and 60°, warm air flows polewards within the eddies. At the tropopause, air flows back equator-wards until ca. 30° where it subsides and closes the circulation. The polar cell cannot be seen in Fig. 5.5c because it is too weak. The magnitude

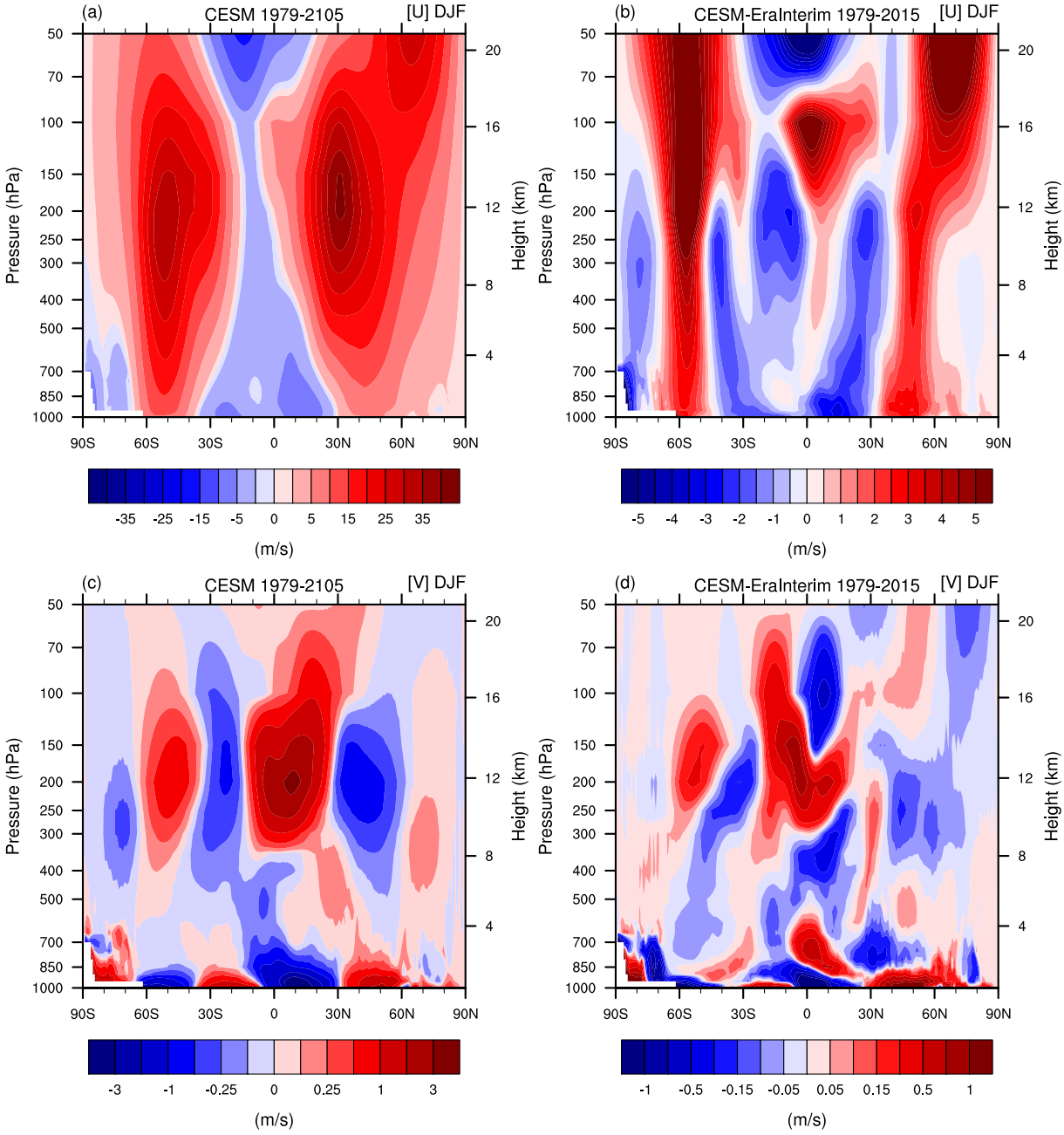

Figure 5.5: Winter (DJF) zonal-mean zonal wind ([U]) climatology from 1979-2015 from CESM (a) and its difference with EraInterim (b), and the winter (DJF) zonal-mean meridional wind ([V]) climatology from 1979-2015 from CESM (c) and its difference with EraInterim (d).

of the thermally driven Hadley cell is larger on the Northern Hemisphere than on the Southern Hemisphere, which is due to the stronger meridional temperature gradient (analogous to the zonal- mean zonal wind). The strongest differences between CESM and EraInterim zonal-mean meridional wind arise at the surface and in the upper troposphere/lower stratosphere (~ 1 ms^{-1}) (Fig. 5.5d), but are overall small (Fig. 5.5d).

5.2.2 North Atlantic modes of variability

In this section, we compare teleconnectivity maps and EOF-maps of the $Z500$ and sea level pressure fields from the CESM simulation with EraInterim reanalysis data.

Teleconnectivity maps

Fig. 5.6 shows winter (DJF) teleconnectivity maps of the North Atlantic region (70° W - 40° E, 20° - 80° N) calculated with detrended $Z500$ and SLP data from 850-1850 of the CESM simulation (a and c) and of the EraInterim dataset from 1979-2015 (b and d). Because teleconnectivity is highly variable over time, a long period was chosen to obtain a robust pattern for the CESM teleconnectivity. Note that because of this longer time, the amplitude is smaller for the CESM teleconnectivity. Therefore, the color scale and the threshold for the teleconnectivity axes are adapted (minimum detection threshold $T < -0.5$ for a and c). The red lines (teleconnectivity axes) connect the local minima with the grid points with which they have the highest negative correlation. Two remarks need to be made concerning the teleconnectivity axes:

- Not every local minimum that has been diagnosed by the minima search algorithm (section 4.1.3) is connected to another grid point by teleconnectivity axes, because only the teleconnections with both centers of action within the plotted domain $\pm$ 10° are drawn. This means that if an isolated minimum is not connected by a red line, the corresponding grid points lies outside of the described domain (e.g. the minimum near 30° E, 70° N in Fig. 5.6a).
- The teleconnectivity axes appear curved on the plot because the teleconnectivity is drawn onto an isogonal projection (Lambert conformal conic projection).

In Fig. 5.6a, several local minima and teleconnectivity axes are identified. The strongest teleconnection is found between the Iberian Peninsula and north-eastern Greenland, resembling a north-easterly shifted NAO-pattern. Furthermore, two meridional connections, one from south-west of the Azores towards the north-western coast of Scotland and one from the south-western edge of the domain towards south of Greenland, are visible. Additionally, two zonal axes from the (eastern) Mediterranean towards (west of) the British Isles are present (East Atlantic pattern). The teleconnectivity calculated from observed $Z500$ data shows a very similar picture (Fig. 5.6b), but with generally enhanced amplitudes. The connection from western Europe towards the north, the meridional connections from the southern North Atlantic towards the central North Atlantic and zonal connections from the south-eastern part of the map towards the center of the domain are all observed. The split-up of the NAO into several dipole

structures (e.g., a western and an eastern connection), as pictured in Fig. 5.6a and b, is also reported in other studies for observational data (*Wallace and Gutzler* 1981; *Moore et al.* 2013).
As the NAO is supposed to be a barotropic system (e.g. *Raible et al.* (2014)), it is present not only at 500 hPa, but also at the surface. Fig. 5.6c and d show teleconnectivity based on sea level pressure fields. In both panels, the number of teleconnections is strongly reduced. In Fig. 5.6c, only two connections from south-western Europe towards the northern/north-eastern part of the region remain, while an additional south-western branch of the NAO remains in Fig. 5.6d. However, the remaining centers of action are associated with the NAO, as they show a bipolar meridional oscillation in the Euro-Atlantic region. Therefore, the observed and modeled NAO can be said to be barotropic.

EOF maps

Additionally to the teleconnectivity method, we compare the climate variability of the observations and the model by means of EOF-maps. In contrast to teleconnectivity maps, which show many simultaneously varying regions and therefore multiple teleconnections, maps based on

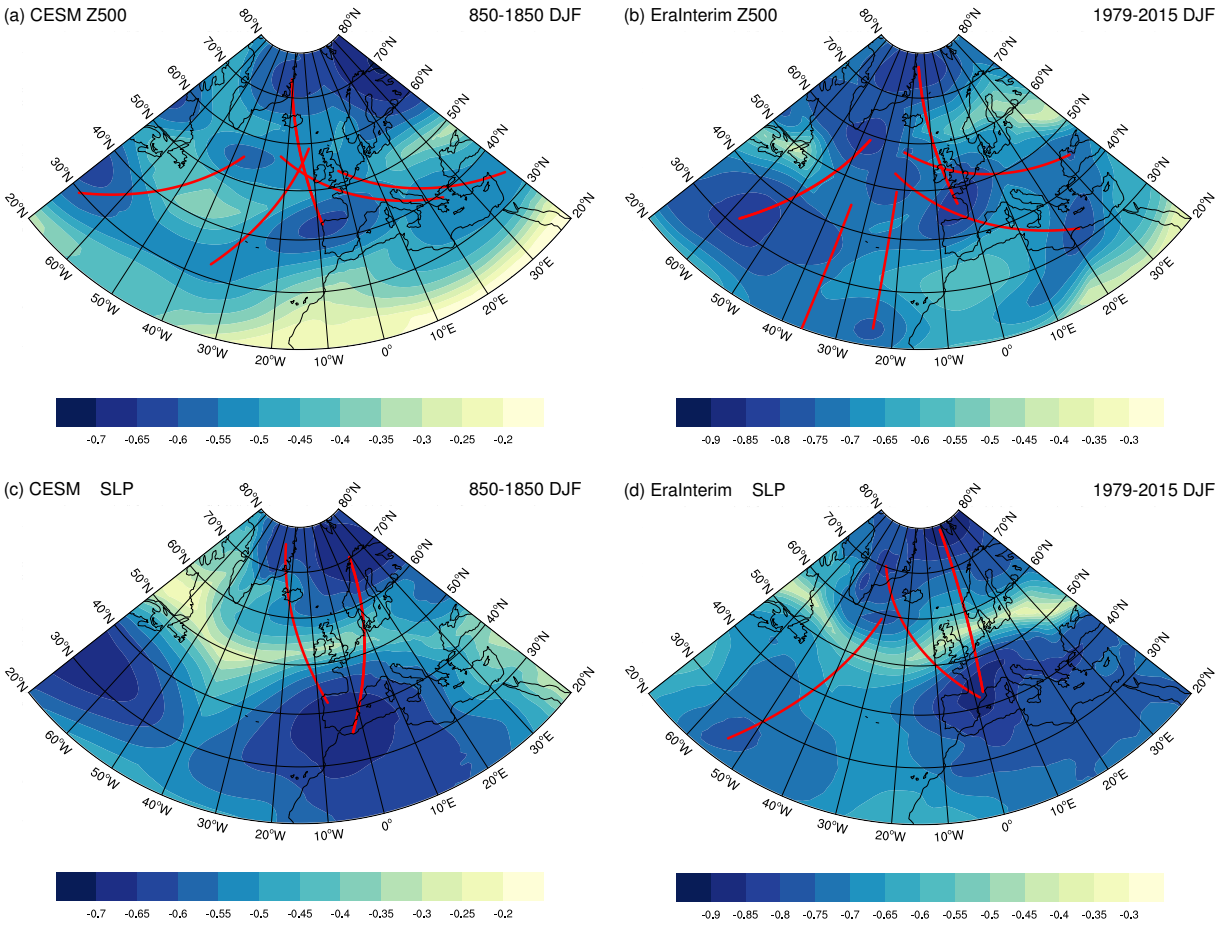

Figure 5.6: *Z*500 CESM (a) and EraInterim (b) and *SLP* CESM (c) and EraInterim (d) winter (DJF) teleconnectivity and teleconnectivity axes (red lines) in the North Atlantic sector (70° W - 40° E, 20° - 80° N) over the period 1979-2015. Note that the threshold for the minima detection is $T <$ -0.5 in (a) and (c) and $T <$ -0.7 in (b) and (d).

EOF analysis only show 'isolated' modes of variability, because the field is divided into orthogonal space-time modes. Therefore, one expects a depiction of single modes of variability when examining maps of the leading eigenvectors of Z500 or sea level. As a result, the interplay between different modes of variability cannot be displayed with a single EOF-map, as they are orthogonal to each other.

Fig. 5.7a shows the first EOF of the Z500 field in the North Atlantic sector, which is often used to define the North Atlantic Oscillation (section 4.1.2), calculated over the period 850-1850. A distinct meridional dipole structure with centers of action over southern Europe and the northern North Atlantic is visible. Compared to the first EOF obtained from observations (Fig. 5.7b), where the centers of action are located north of the Azores and over southern Greenland, both centers of action are shifted to the west. These patterns explain 37.4% (CESM) and (43.2%) of the Z500 variability in the plotted sector. A similar picture is valid for the first EOF of the sea level pressure field (Fig. 5.7c and d). The northern centers of action are in very similar locations between Iceland and northern Scandinavia. The southern center of action of CESM is very spacious with highest values over north-eastern Africa, while the observed one lies north-eastwards of the Azores. The first EOF of CESM sea level pressure accounts for 35.1% of

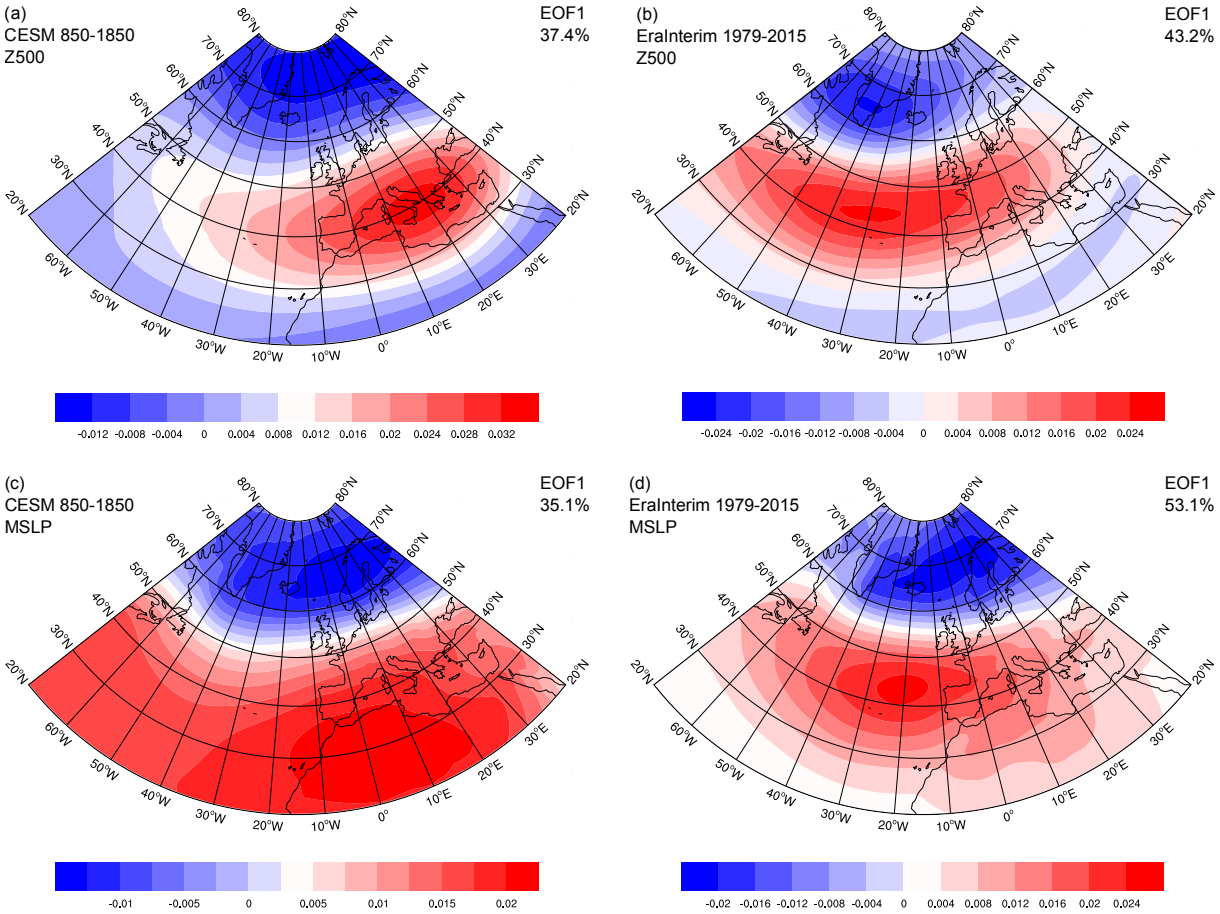

Figure 5.7: Leading eigenvectors of the winter (DJF) detrended CESM Z500 (a), EraInterim Z500 (b), CESM *SLP*(c) and EraInterim *SLP* (d) fields in the North Atlantic sector (70° W - 40° E, 20° - 80° N) over the periods 850-1850 (CESM) and 1979-2015 (EraInterim).

the sea level pressure variability in the Euro-Atlantic region, the observed EOF1 for more than 50%. The first EOFs at the different heights of both CESM and EraInterim are very similar to each other, especially the northern part. Hence, these patterns are quasi-barotropic also from an EOF-viewpoint.

By looking at Fig. 5.8a and b, we realize that the second EOFs of the Z500 field in the Euro-Atlantic region from CESM (over the period 850-1850) and EraInterim substantially differ from each other. The CESM pattern strongly resembles the one from EOF1, as it is also characterized by a meridional dipole structure. The maxima are slightly displaced and the axis between them is tilted clockwise. The second EOF of observed Z500 shows a zonal dipole between the Mediterranean and the central North Atlantic, normally referred to as the East Atlantic pattern. Here, it is almost orthogonal to the pattern of CESM (Fig. 5.8a). This is surprising, because the Z500 teleconnectivity fields of CESM and EraInterim both depict zonal teleconnections. Further, the CESM EOF2 explains 30.9% of the field's variance, which is only slightly less than EOF1, while EraInterim EOF2 only accounts for 19.3% of the variability. The third EOFs of the two datasets are again similar to each other, with a zonal dipole pattern between Europe and the central North Atlantic (Fig. 5.8c and d). Though, the CESM pattern is shifted to the north-

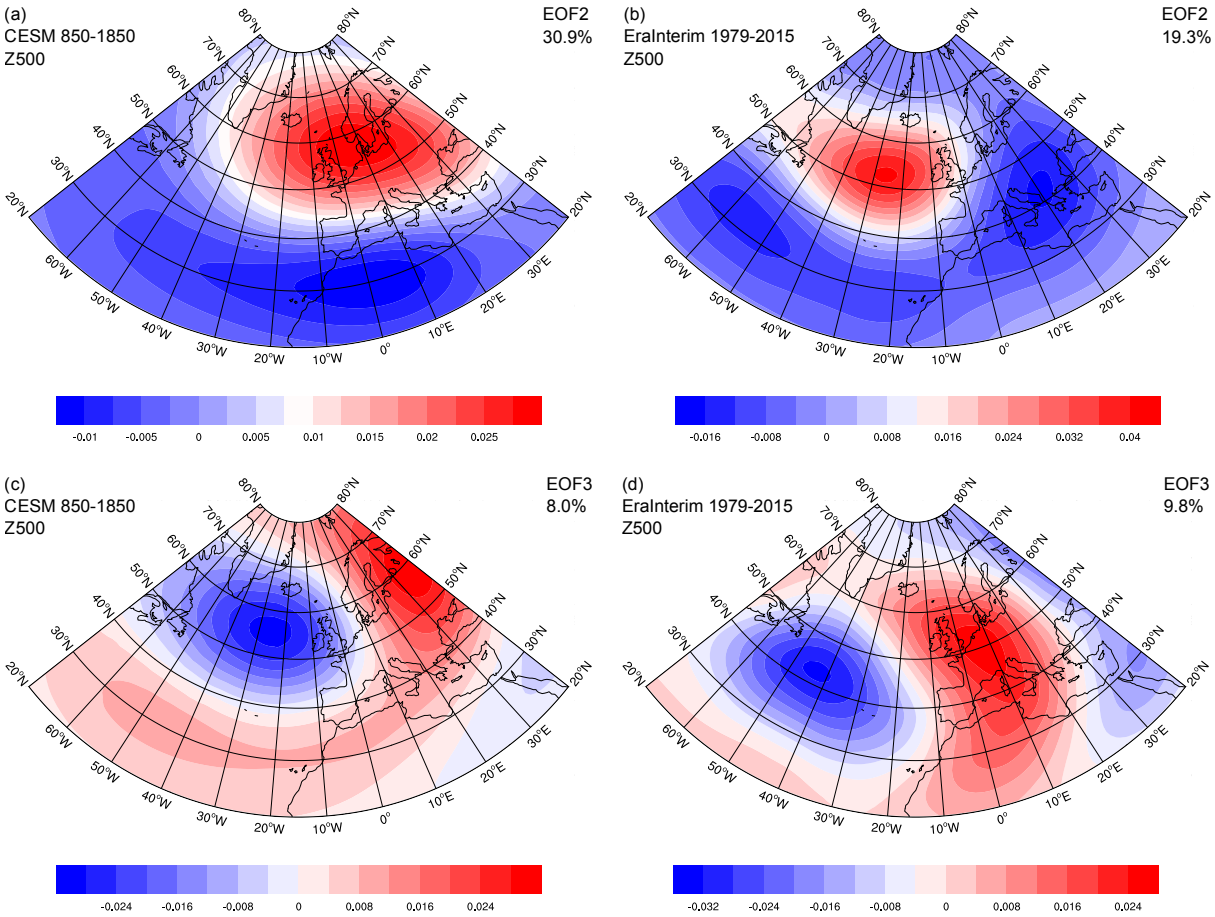

Figure 5.8: EOF2 of CESM (a) and EraInterim (b) and EOF3 CESM (c) and EraInterim (d) the winter (DJF) detrended Z500 field in the North Atlantic sector (70° W - 40° E, 20° - 80° N) over the periods 850-1850 (CESM) and 1979-2015 (EraInterim).

east with reference to the EraInterim pattern. The third EOF plays a minor role in the North Atlantic climate variability, which is indicated by the low fractions of explained variance (8.0% for CESM, 9.8% for EraInterim).

5.3 Summary and Discussion

The long-term mean temperature evolution corresponds well to proxy reconstructions and to other state-of-the-art climate models. By looking at climatological periods from 1979-2015 of the basic climate variables, we found systematic biases in the geopotential height field, the pressure gradient and the zonal wind, especially in the North Atlantic sector. These biases are likely linked to the deficient representation of high-latitude blockings in the North Atlantic sector, which is a common problem of most state-of-the-art climate models (*Davini and D'Andrea* 2016). As the formation of single NAO-events is strongly linked to blockings and wave breaking at high latitudes, many CMIP5-models (also CCSM4) do not properly simulate the dynamical processes underlying the NAO (*Davini and Cagnazzo* 2014). However, *Davini and Cagnazzo* (2014) showed that the spatial patterns of the NAO derived by statistical methods (e.g. EOF1) are mostly well represented by the models, even though the underlying atmospheric dynamics differ from the observed ones.

In the CESM simulation, the spatial characteristics of the North Atlantic teleconnectivity maps agree with the ones from EraInterim. As the focus of this thesis lies primarily on investigating the spatial variability of the teleconnections in the Euro-Atlantic sector and not on its dynamical processes, we conclude that the systematic biases in the simulation are of minor concern. Nevertheless, it is important to be aware of this issue, especially when the role of internal atmospheric dynamics in altering the spatial characteristics of the teleconnections is investigated.

The teleconnectivity maps show a better agreement with the EraInterim data than the EOFs, and they account for a more complex representation of the climate variability. Therefore, the following analysis of the spatial variability of the teleconnections in the North Atlantic is based upon this method.

Chapter 6

Variability of the NAO

In this section, the variability of the NAO during the course of the transient 1250-year long simulation is investigated. Because of its complexity, the analysis is split into a temporal part, where periods of enhanced and reduced decadal and multi-decadal scale variability are detected, and a spatial part, in which structural changes of the centers of action and their positions in the North Atlantic region are of interest.

6.1 Temporal variability

6.1.1 Description of the temporal variability

It is well-known that the NAO fluctuates on many different time scales, ranging from the weekly formation and dissipation of single events over inter-seasonal and inter-annual to decadal and multi-decadal variability (*Hurrell et al.* 2003). Of special interest are periods in which the low-frequency variability is enhanced (i.e. prolonged periods of either the positive or negative phase), because they can mask or amplify other long-term processes. In the following, we assess whether the NAO as simulated by the transient CESM simulation exhibits this temporal behavior by applying the wavelet transform introduced in section (4.3). Wavelet power spectra (WPS) indicate in which frequency a time series shows the most variability. For example, if there is high power at a specific frequency and low power at other frequencies in a time interval, the time series exhibits the strongest variability at the indicated frequency. Obviously, this idealized case is rarely observed, as atmospheric processes like the NAO happen on various time scales.

The wavelet transform is applied to the grid point based NAO-index and the index derived from EOF-analysis over the whole simulated period, and their spectra are displayed in Fig. 6.1. Time intervals with high variability at a certain frequency are colored orange and red, and the 95% confidence interval is marked with crossed lines. Note that the length of the time series (in this case 1250 years) limits the explanatory power of the wavelet power spectrum. The power at very high periods is not meaningful, because the length of the time series is not sufficient to explain temporal variability on this time scale. The maximum period which can be analyzed

is obtained by the length of the time series divided by 2. This is only true for the (two) middlemost time step(s). The closer the time step is to one of either the start or the end of the time series, the lower the maximum period, because less data is available for the analysis. The parts of the wavelet power spectrum that cannot be used for the analysis are marked by the 'cone of influence'.

The grid point based NAO-index from the transient CESM simulation undergoes eminent temporal variations on different frequencies (Fig. 6.1a). Except for the prolonged interval of high power around the period of 256 years, which is partly outside the cone of influence, no dominant and persistent NAO-frequencies are present. At periods between 2 and 8 years, the index experiences enhanced variability during several intervals (e.g. between 1100-1200 and 1400-1500) and reduced variability during 1250-1350 and 1750-1850. At decadal time scales, single significant peaks (around the years 1000, 1450, 1800 and 2050) alternate with distinct gaps (in the intervals 850-950, 1250-1400 and 1550-1700), with overall reduced power than at periods between 2 and 8 years. Generally enhanced power is found at multi-decadal frequencies (periods between 20 and 50 years). While pronounced peaks are found around the years 1100, 1400 and 1550, the periods 1200-1350 and especially after 1850 show large gaps.

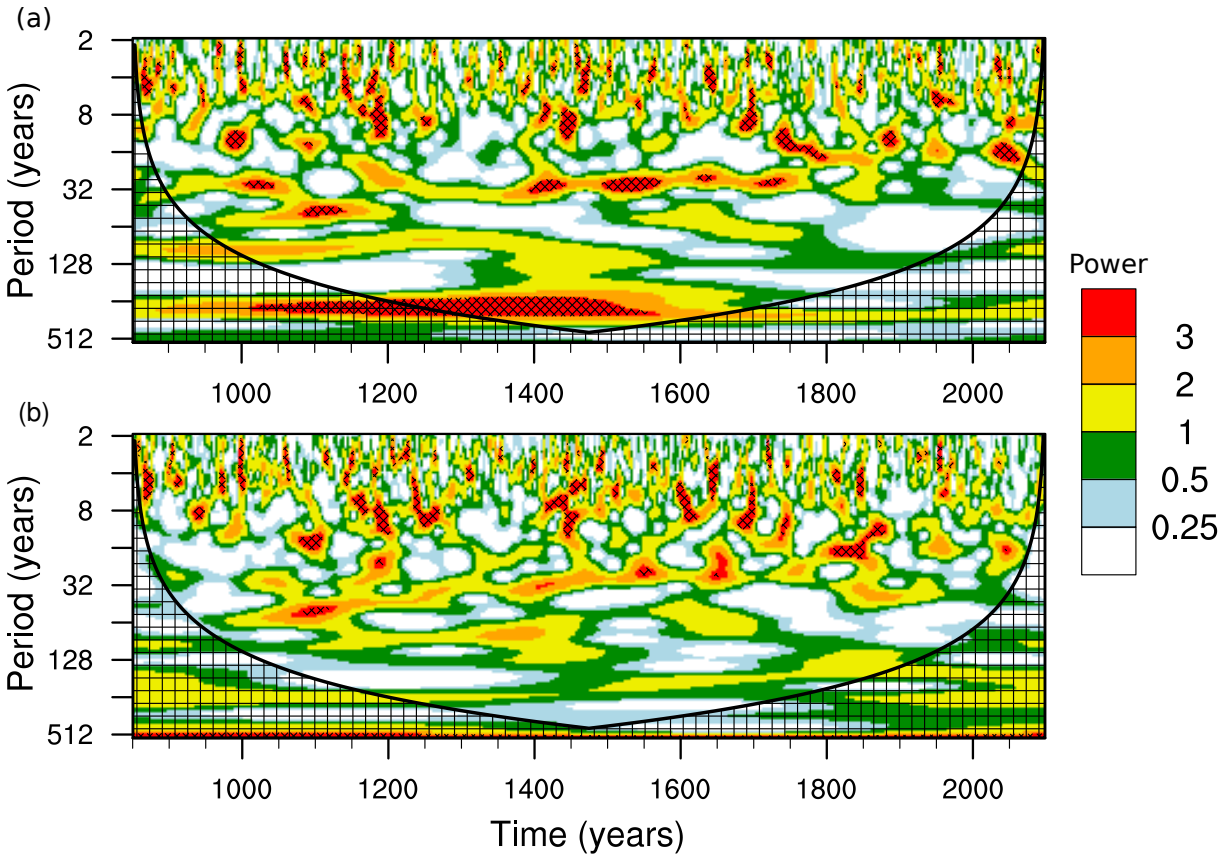

Figure 6.1: Wavelet power spectrum (WPS) of the grid point based (a) and the EOF-based (b) NAO-index from 850-2099. The 95% confidence interval is marked with crossed lines, the 'cone of influence' is indicated by the gridded lines. The parameters for the calculation are a = 1 and b = 0.05, and the mother wavelet is Morlet (equation 4.10).

The wavelet power spectrum of the time series of the *SLP* EOF1 is plotted in Fig. 6.1b. The variability at low periods is similar to the one of the grid point-based index with alternating high and low power on short time scales. Generally, the overall power is slightly reduced compared to Fig. 6.1a, especially at low frequencies/high periods. However, the EOF1-based index also experiences intervals of enhanced low-frequency variability (e.g., between 1050-1150 and between 1800-1900) that alternate with periods of reduced low-frequency variability (e.g. between 900-1000). Most of the time intervals with enhanced power around the period of 32 years lie in phase with the ones from the grid point-based NAO-index, as for example the maxima between the years 1000-1200 and 1400-1700 or at 1950 and 2050. In contrast to the grid point-based index, no prolonged period of enhanced power at low frequencies is present. Still, the two indices share a similar temporal variability with in-phase occurrences of enhanced and reduced low-frequency variability and are both characterized by strong non-stationary behaviour.

To illustrate these temporal variations on different time scales in another way, Fig. 6.2 shows the grid point-based NAO-index and its running mean for two selected time intervals with different wavelet power spectra (from 1300-1400, Fig. 6.2a, and from 1500-1600, Fig. 6.2b). The pure index (dashed black line) illustrates the high-frequency variability, whereas the running mean (red line) is helpful to visualize low-frequency variations. The wavelet power spectrum of the interval from 1300-1400 shows some moderate power at low periods and exhibits a gap between the periods 8 and 32 years. The NAO-index and its running mean are dominated by high-frequency variability with strong year-to-year variations, especially during the first 40 years (Fig. 6.2a). The period from 1500 to 1600 is affected by both high and low-frequency variability, with a distinct maximum around 32 years. Examining the index yields some strong year-to-year variations, but the running mean indicates strong multi-decadal variability with periods of 40 (1505-1545) and 20 (1545-1560) years (Fig. 6.2b).

6.1.2 Discussion

The grid point-based and the EOF-based NAO-indices calculated over the 1250-year CESM simulation exhibit maximum amplitudes in the frequency bands related to inter-annual, decadal and multi-decadal variability, but no predominant frequency is present. This is in general accordance with the results of studies which analyzed the temporal variability of NAO-indices calculated from different data. Investigations of various NAO-indices from observations have shown a strong non-stationary behaviour with variability alternating between quasi-biennial and -decadal time scales, and that the maximum power is mostly concentrated in periods less than 10-15 years (e.g. *Hurrell et al.* 1997; *Pozo-Vázquez et al.* 2001; *Barbosa et al.* 2006). *Barbosa et al.* (2006) conducted wavelet analysis of two different wintertime NAO-indices (Lisbon and Gibraltar) and found differing patterns of low-frequency variability, indicating that the choice of the index strongly affects the results. This agrees with the slightly differing wavelet power spectra of the highly correlated CESM grid point- and EOF-based indices.

As the longest observation-based NAO-index reaches back approximately 2 centuries (extended

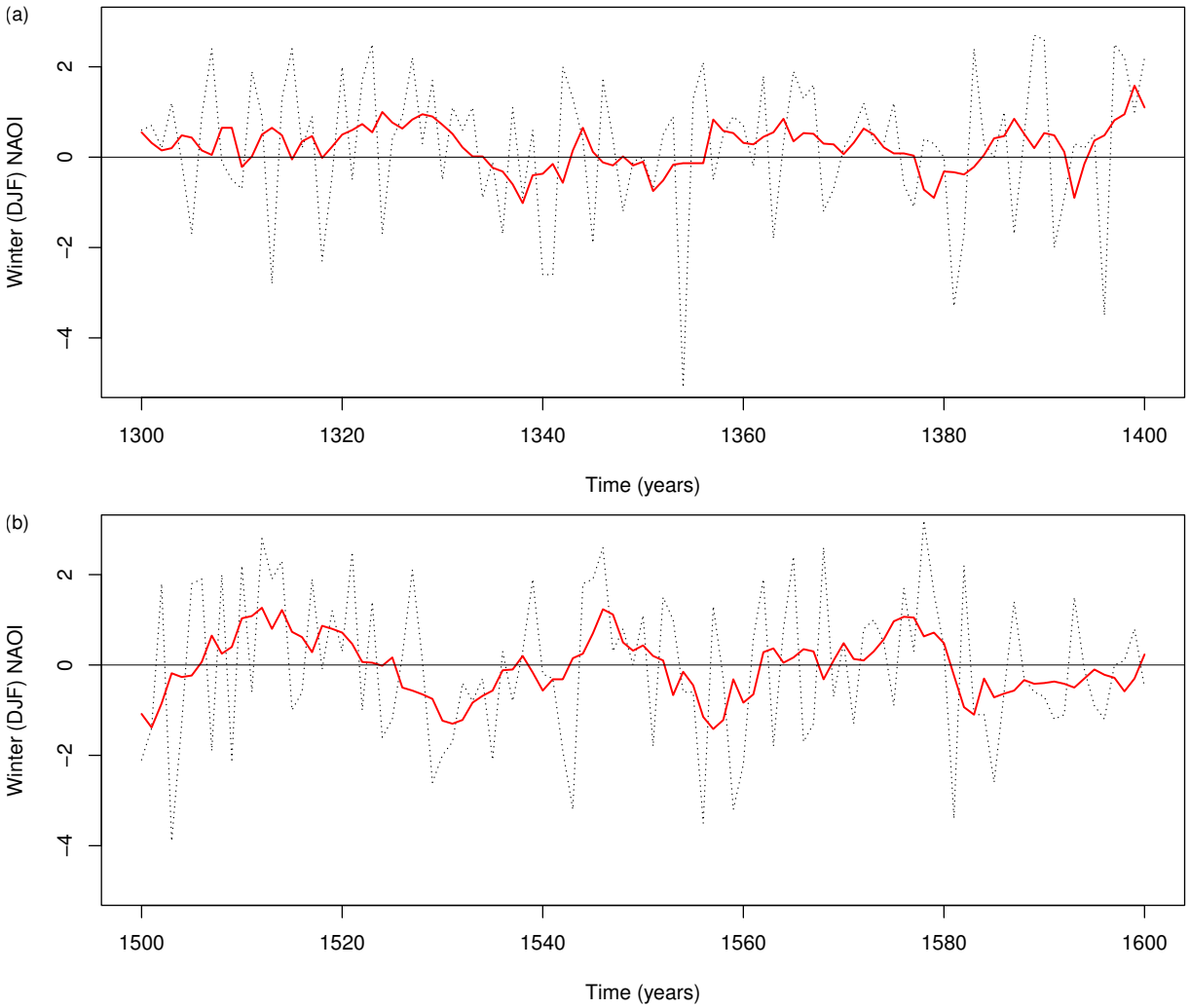

Figure 6.2: Grid point-based North Atlantic Oscillation Index (dashed line) and two-sided moving average over 10 years (red line) from 1300-1400 (a) and 1500-1600 (b).

Gibraltar/Reykjavik NAO-index, starting in 1821 (*Vinther et al.* 2003)), they cannot be used to draw inferences about temporal variability on very low frequencies. Reconstructed indices using proxy data extend the time series beyond the instrumental period and allow investigations on longer time scales. *Appenzeller et al.* (1998) have analyzed the temporal characteristics of an ice core-based NAO-index reaching back to 1650 and have found significant high wavelet power not only at sub-decadal to decadal periods, but also at periods of 80-90 years. Also *Luterbacher et al.* (1999) found significant spectral power at high periods (54-68 years) in a reconstructed annual-mean NAO-index.

Obviously, the wavelet power spectra of the simulated NAO-indices do not coincide with the observed and reconstructed ones. This is, on the one hand, due to the fact that even similar indices (e.g. the Lisbon and Gibraltar NAO-indices) do not show the same low-frequency variability (*Barbosa et al.* 2006). On the other hand, the internal variability of the model and of the actual climate system are not necessarily in phase, which hinders the chronologically correct representation of the temporal characteristics of the NAO by climate models. However,

the main properties, being the absence of a predominant and persistent frequency with high power and the alternation between high- and low-frequency variability, are captured by the model.

6.2 Spatial variability

6.2.1 Description of the spatial variability

In order to investigate the spatial variability of the NAO in the transient CESM simulation, the teleconnectivity method is applied to Z500-data in the North Atlantic. To assess the temporal changes, teleconnectivity is calculated for 30-year running windows of the Z500-fields, resulting in 1221 teleconnectivity maps. Because it is difficult to present such an amount of data, we use the pattern correlation method to compare the individual time steps to a reference situation. The reference used here is the teleconnectivity map of the EraInterim 1979-2015 DJF Z500-field (Fig. 5.6b). The resulting time series from the pattern correlation analysis is depicted in Fig. 6.3. With a mean pattern correlation of 0.25, the agreement between CESM teleconnectivity and the EraInterim reference teleconnectivity is relatively low. Fig. 5.6 shows high temporal variability with rapid transitions from rather high to low values, ranging from the maximum value of 0.69 in the period 1844-1873 to the minimum value of -0.37 in the period 1609-1638. Most of the time, the values lie between 0 and 0.4. There exist some periods with prolonged constant high values, e.g. between 1400-1450, 1650-1700 and 1800-1850, and periods with values < 0 are mostly characterized by isolated drops, e.g. around 950, 1350, 1400 and 1600. Thus, Fig. 6.3 illustrates that the teleconnectivity in the North Atlantic sector is highly variable in the transient CESM simulation with respect to the reference period.

Problematic about this approach is that the chosen reference period is to some extent arbitrary.

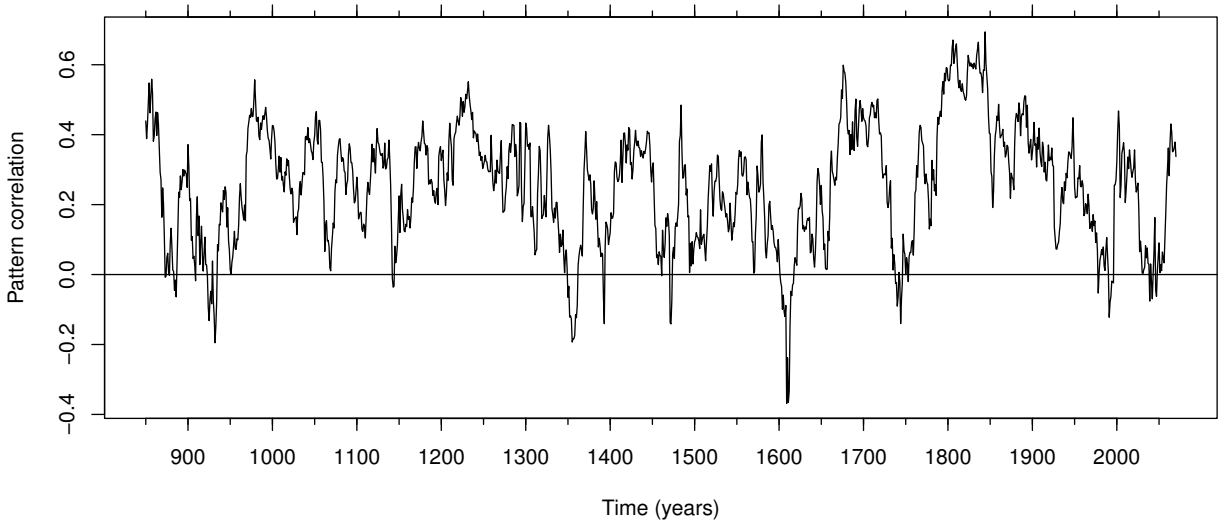

Figure 6.3: Time series of the pattern correlation of the North Atlantic EraInterim Z500 teleconnectivity field from 1979-2015 (Fig. 5.6b) and the 30-year running window of the North Atlantic CESM Z500 teleconnectivity field from 850-2099.

As already mentioned in section 5.2.2 and indicated by the strong fluctuations of the modeled teleconnectivity, also the observed teleconnectivity field highly depends on the time. Hence, it does not mean that the EraInterim teleconnectivity from 1979-2015 is representative for the overall climate variability. Because of this, the analysis of the spatio-temporal changes of the North Atlantic teleconnections following in the next section will not be conducted by comparing the CESM teleconnectivity with observations, but rather with the simulation itself.

In doing so, the pattern correlation of each of the 1221 30-year windows with all other periods was computed, resulting in a 1221 x 1221 matrix. This correlation matrix is displayed in Fig. 6.4a. Every point displays the pattern correlation between the two corresponding time periods on the x-and y-axis. Note that the diagonal line is equal to 1 and the pattern correlations close to this line are very high, because the 30-year periods overlap. Instead of examining single points, one can also interpret every line (either from left to right or from the bottom to the top) as a color-coded time series, analogous to Fig. 6.3. The plot is characterized by medium to high pattern correlation values (between 0.3 and 1) and periods of constant low pattern correlations, e.g. around the years 925, 1300, 1400, 1875 and 2050. As these periods have low values at almost all time steps, except for small gaps, this indicates that the spatial structure of the teleconnectivity in these periods differs strongly from the patterns of the other periods, from a pattern correlation point of view. Also the periods of high pattern correlation values are interrupted only by the periods of constant low pattern correlation.

To further analyze the pattern correlations among the teleconnectivity fields, the correlation coefficients of all pattern correlation time series are calculated and depicted in Fig. 6.4b. For example, the value at the intersection of the years 850 and 1200 gives the correlation coefficient of the pattern correlation time series of the years 850 and 1200. High values show that the temporal behavior of two pattern correlation time series is similar, values close to 0 indicate that there is no similar behavior, and negative values show that two time series are anti-correlated. If all points of a specific period (corresponding to a line from left to right) had high values, the pattern correlation time series of the period would be highly correlated to all other pattern correlation time series. As the teleconnectivity is highly variable over time, this is not the case for any of the periods. This additional analysis gives a more robust statement whether two fields are similar or not, because not only the patterns of the two fields are compared (as in Fig. 6.4a), but also if they show the same (dis-)similarities with other fields.

In contrast to Fig. 6.4a, where the values ranged from slightly below 0 to 1, Fig. 6.4b is characterized by values ranging from strong negative to strong positive correlations. It is striking that the lines of constant low pattern correlation from Fig. 6.4a coincide with lines of low or negative values of correlation in Fig. 6.4b. When focusing on the line of low pattern correlation values around the period 1300, one can see that the correlations with the other pattern correlation time series are mostly negative, indicating opposing temporal behavior. In other words, the pattern correlation time series of the periods around 1300 are anti-correlated with most of the other pattern correlation time series. This almost continuous line of negative values is interrupted at

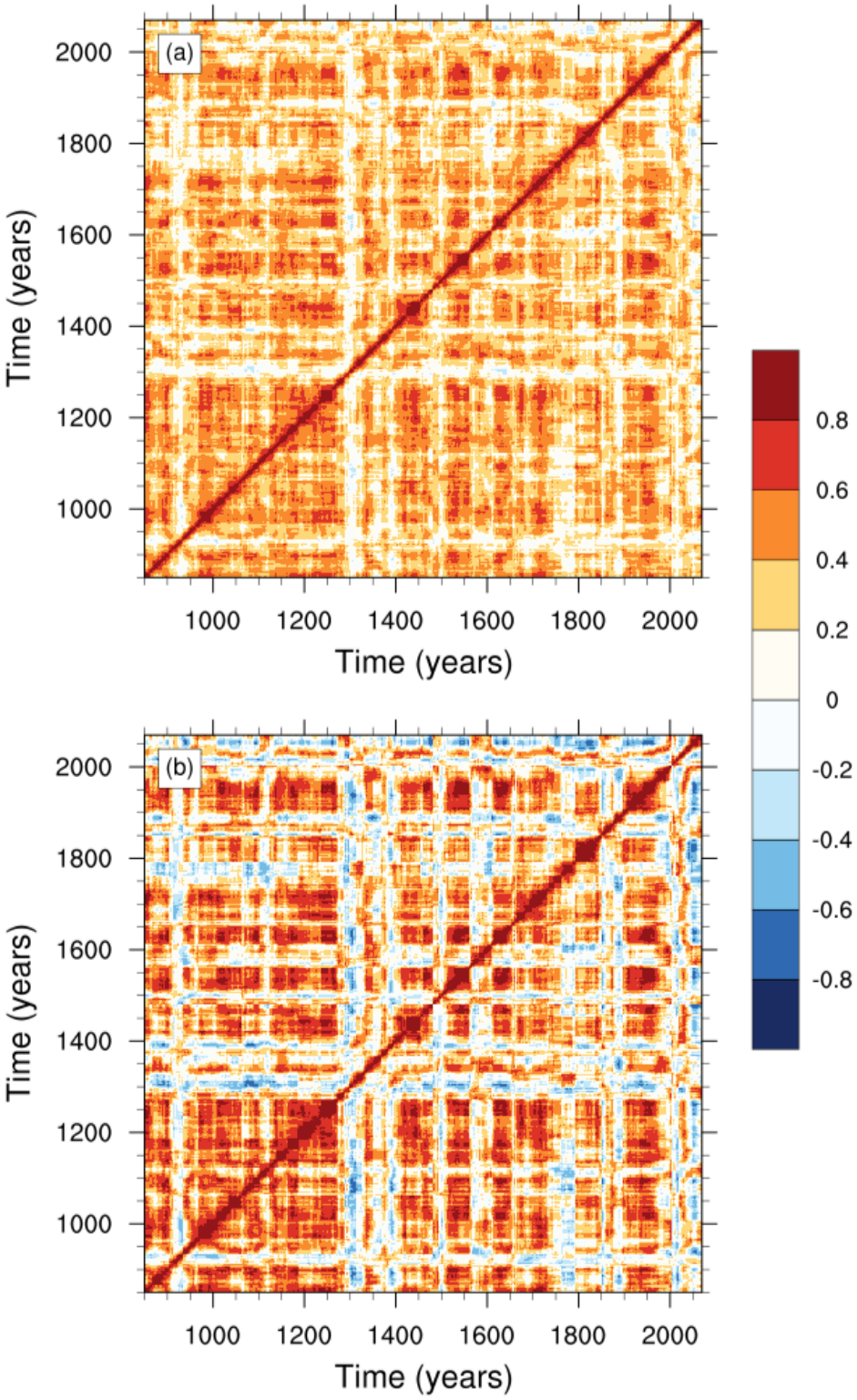

Figure 6.4: Color-coded pattern correlations of the 1221 30-year running window teleconnectivity fields with each other (a) and the correlations between the single pattern correlation time series (b). A value at the intersection of two years in (b) gives the correlation coefficient of the pattern correlation times series of the two years.

interceptions with other low-value periods, such as around the years 1400, 1600, 1800 or 2050. This behaviour also holds true for most of the other low-value periods. This suggests that the periods with low pattern correlation values (Fig. 6.4a) differ from the ones with high values, but share similarities with periods of low pattern correlation, as their pattern correlation time series are correlated.

This can be confirmed by analyzing the correlations of pattern correlation time series of periods with generally high pattern correlations. They have high correlation coefficients with most other time series, except for the quasi-continuous lines of low pattern correlation. Hence, time periods having high pattern correlation values are also correlated with each other, and anti-correlated or uncorrelated with periods of low pattern correlation.

A more condensed form of the information in Fig. 6.4a is given in Fig. 6.5, which only shows the mean value of the pattern correlations of each period. The comparison of Fig. 6.5 and Fig. 6.4a shows that the mean value of the pattern correlation time series is meaningful. The minimum values in Fig. 6.5 correspond well to the lines of low correlations in Fig. 6.4a (e.g. around the years 950, 1300, 1400, 1500, 1750, 1900 and 2050). The same holds true for periods with high values. Further, as almost no negative values are present in Fig. 6.4a, no compensation of very high and low values occurs (e.g. many values of -0.7 and +0.7 would result in a mean close to 0). Hence, taking the averages of each period with all other periods is a good approximation of the full correlation matrix.

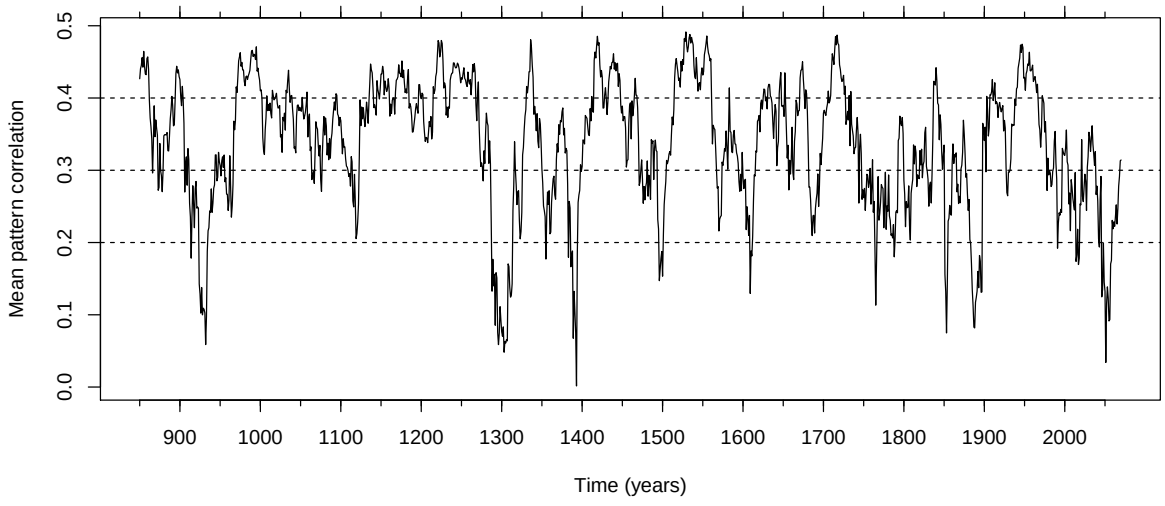

Figure 6.5: Time series of the average pattern correlations of the 30-year running windows of the CESM Z500 teleconnectivity field with all other periods from 850-2099. The value at time step 850 denotes the mean pattern correlation of the period 850-879 with all other periods, and so forth.

6.2.2 Classification methods

Classification with pattern correlation

Based on the analysis of Fig. 6.4, we attempt at identifying regimes of the North Atlantic climate variability by classifying each period into a group based on the mean pattern correlation value with all other periods (Fig. 6.5). The visual analysis of teleconnectivity maps with high and low mean pattern correlation values showed that high mean pattern correlations are associated with meridional teleconnections, while low values come along with zonally oriented teleconnections. Dividing the 1221 time steps into two groups (e.g. pc higher or lower than 0.25) results in one meridionally and one zonally oriented composite (not shown). This choice does not take the many values in the middle of the range into account. This is why both composites also contain patterns associated with the other group. A classification into 3 classes (e.g. $pc < 0.25$, $0.25 < pc < 0.35$ and $pc > 0.35$) leads to two well defined composites (one meridional, one zonal) and one composite with both meridional and zonal structures (not shown). A problem with the latter group is that, in contrast to the groups formed with high and low pc-values, the intermediate pc-values (here from 0.25-0.35) are not related to a specific pattern. Therefore, the structures in the middle group are blurred. Adding another group (four classes; e.g $pc < 0.2$, $0.2 < pc < 0.3$, $0.3 < pc < 0.4$ and $pc > 0.4$) does not only split up the intermediate class into two composites with a tendency to either the meridional or the zonal group, but also reduces the size of the upper and lower classes, making them well-defined. An additional class (5 classes) does not improve the classification, as the emerging class is very similar to one of the existing composites (depending on the choice of the thresholds).

Finally, the four categories $pc > 0.4$, $0.4 > pc > 0.3$, $0.3 > pc > 0.2$ and $pc < 0.2$ were chosen because each of the classes represents a different pattern and the composites are well separated from each other. The four composites and the corresponding variances are shown in Fig. 6.6. Note that the composite maps do not have teleconnectivity axes, as averaging them would not give a meaningful result.

The first composite map (Fig. 6.6a, $pc > 0.4$) has been calculated with 333 members and shows a spacious area of high teleconnectivity in the northern North Atlantic sector with an excrescence towards south-west. Another distinct area of enhanced teleconnectivity is located over south-western Europe. Together, these two centers show a slightly eastward shifted NAO-like pattern, as it is also present in the 1000-year CESM and the EraInterim teleconnectivity. The minimum at the south-western edge of the domain is likely the southern center of action of the western part of the NAO. The variance of composite 1 in Fig. 6.6b displays high variability of the teleconnectivity in the southern half of the domain and over Newfoundland, suggesting that the single members of the composite do not show good agreement in these areas. In contrast, the low variance in the areas of strong teleconnectivity argues for good accordance between the members.

Composite 2 (Fig. 6.6c, 502 members, $0.4 > pc > 0.3$) has a very similar spatial structure as com-

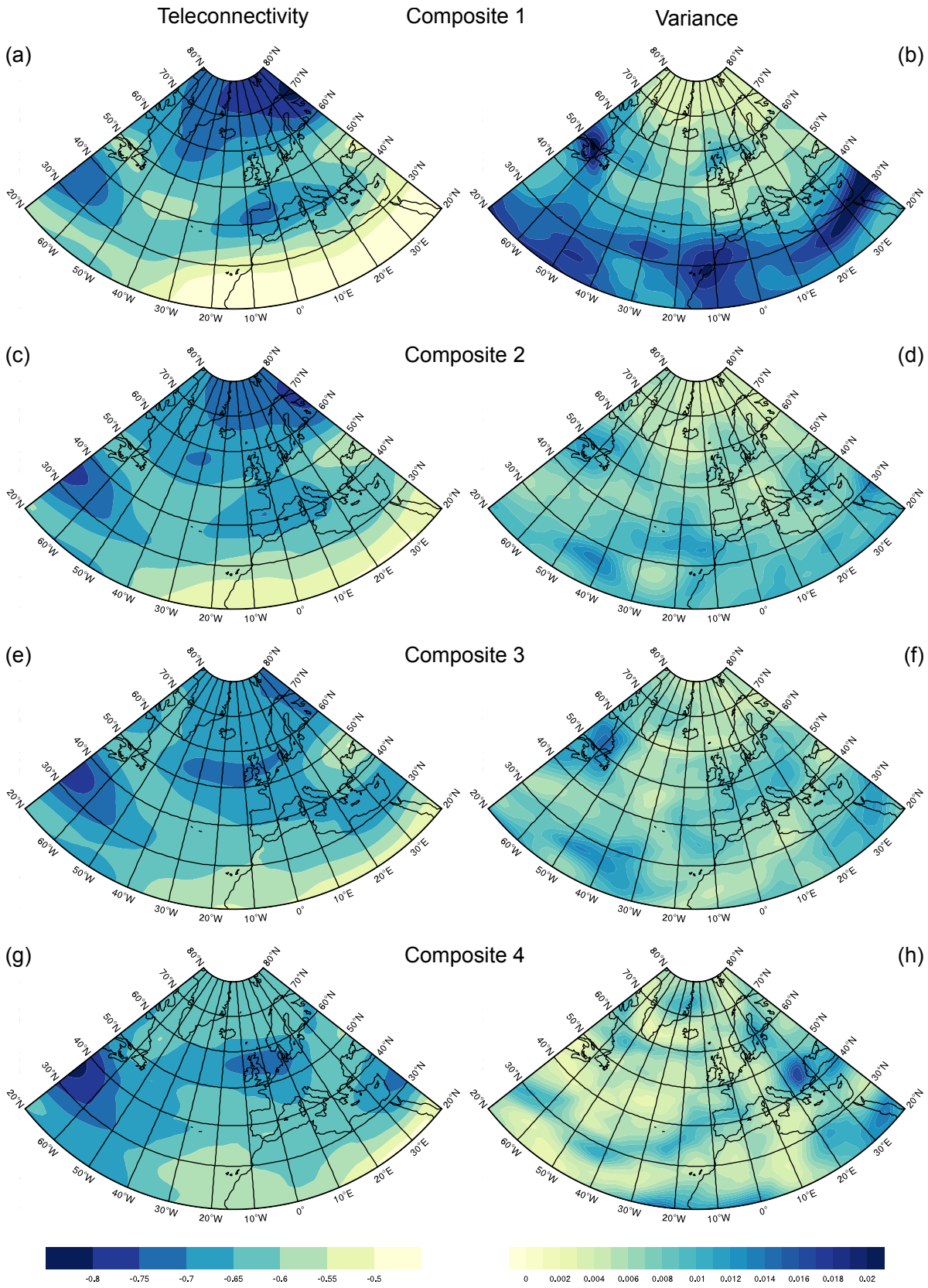

Figure 6.6: Composites of the teleconnectivity fields with a mean pattern correlation higher than 0.4 (a, 333 members), between 0.3 and 0.4 (c, 502 members), between 0.2 and 0.3 (e, 287 members) and lower than 0.2 (g, 99 members), and the corresponding variances (b, d, f and h).

posite 1. As in Fig. 6.6a, a north-south dipole structure between the northern North Atlantic and Europe is present, but the magnitudes and gradients are smaller. Further, the excrescence of the northern center of action is cut off. A comparison with the CESM teleconnectivity from 850-1850 (Fig. 5.6a in section 5.2.2) suggests that this center of action is often linked either to the south-eastern Mediterranean region by a zonal teleconnection, or to the south-western center of action. The variability (Fig. 6.6d) is overall lower than the one of composite 1, but the structure is very similar with a gradient reaching from north to south.

Composite 3 (Fig. 6.6e, 287 members, $0.3 > pc > 0.2$) is characterized by one minimum over the central North Atlantic and the British Isles, and a branch reaching towards the eastern Mediterranean. The northern North Atlantic is characterized by slightly increased teleconnectivity, but no center of action is present. In contrast to the composites 1 and 2, no clear meridional dipole structure indicating NAO-like variability is present. Instead, a meridional dipole exists. The variance (Fig. 6.6f) is rather low, again bearing a good agreement among the composite members.

Composite 4 (Fig. 6.6g, 99 members, $pc < 0.2$) partly resembles composite 3 with a more isolated central center of action and a center east of the Mediterranean. Other than the composites 1-3, composite 4 totally lacks low teleconnectivity values in the northern North Atlantic. Fig. 6.6h shows very low variability of the composite members almost all over the domain.

In summary, composite 1 and 2 are both characterized by a distinct meridional dipole structure in the North Atlantic sector. Composite 3 also yields some NAO-like structures, while only composite 4 completely lacks a center of action in the northern North Atlantic. Zonal variability in the geopotential height field is contained in composites 3 and 4, and to some extent in composite 2. About 68% of the time frames belong to the NAO-dominated composites, the remaining 33% of the time steps belong to the zonally dominated composites.

Classification with cluster analysis

Additionally to the classification by means of the pattern correlation, a K-means cluster analysis is applied to the 30-year running window teleconnectivity fields. During the procedure, many different settings ($1 < K < 50$) are tested with respect to the quality measures presented in section 4.2. The Explained Variation (EV) and the Silhouette Index (SI) are plotted in Fig. 6.7. EV increases almost monotonically with growing K, as more variance is explained by more clusters. SI has the highest value at $K = 2$ (0.38), but then drops to 0.1 and increases slowly with growing K. While EV recommends a choice of a large K, SI suggests $K = 2$. This contradiction indicates that the applied clustering method is not able to classify the single frames into well separated clusters. The cluster analysis with $K = 2$ leads to an imbalanced distribution of the single frames (1056 and 165 members) and the resulting composites are hardly distinguishable. When applying the 'elbow-rule' to the EV-plot (Fig. 6.7) and having in mind that the manual

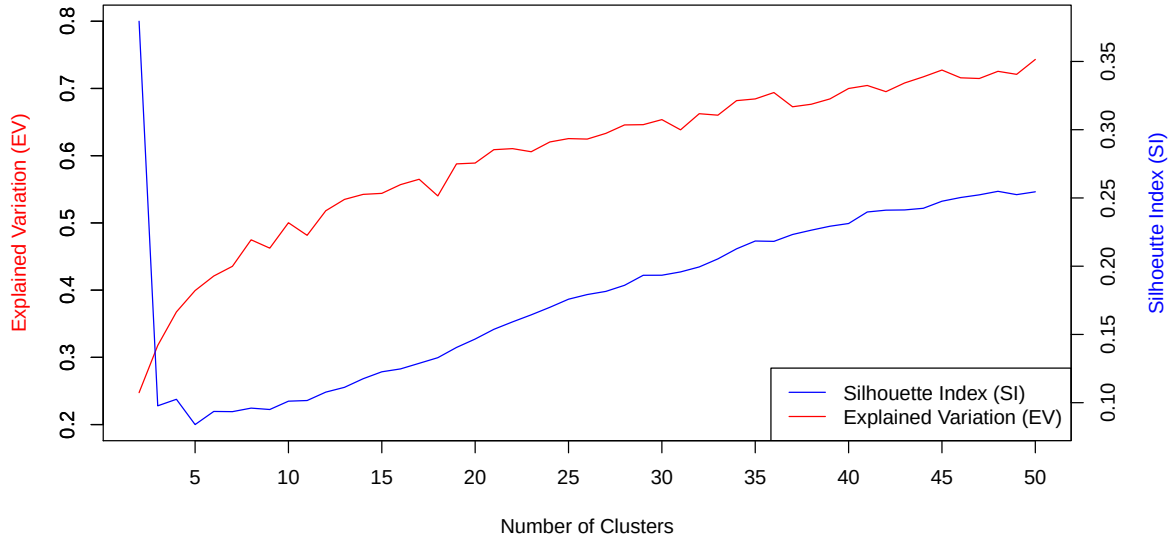

Figure 6.7: The Explained Variation (EV, red) and the Silhouette Index (SI, blue) of the k-means cluster analysis of the CESM teleconnectivity as a function of K (number of clusters).

pattern correlation classification resulted in 4 categories, the choice of $K = 4$ ($EV = 0.38$, $SI = 0.1$) seems appropriate. The composites resulting from the K-means cluster analysis with $K = 4$ and the variances of the composite members are displayed in Fig. 6.8. Note that the order of the clusters has been adapted in order to better compare them to the composites of the manual classification.

The first cluster (Fig. 6.8a, 460 members) is characterized by a dipole structure with a spacious area of strong teleconnectivity in the northern North Atlantic, reaching from the north-eastern edge of the domain to south of Greenland, and a smaller center of action over western Europe. The southern center extends far south-westwards and connects to the strong minimum at the western edge of the domain, which is present in all panels. As in composite 1 of the PC-classification, the NAO-signal is split into an eastern and a western part. The variance of the members contributing to cluster 1 (Fig. 6.8b) is low for most parts of the domain, especially in the areas where the teleconnectivity is large. The large number of members in cluster 1 (460) and the overall low variance shows that this cluster is robust.

Cluster 2 (Fig. 6.8c, 240 members) bears strong resemblance to cluster 1, but the south-western tip of the northern center of action is cut off. The center of the teleconnectivity area over western Europe is in the same position and has the same magnitude as in cluster 1, but instead of reaching to the west, it extends further to the south-east. Similar to the pattern correlation composites, a teleconnection from the central North Atlantic to the Mediterranean is present. The variance of the members of cluster 2 (Fig. 6.8d) is increased in some parts, e.g. in the south-eastern Mediterranean and west of the European Atlantic coast. However, in the areas of the NAO, the variability is low, showing that the NAO-centers of action are robust, whereas the zonal teleconnections are exposed to more variability.

Cluster 3 (Fig. 6.8e, 96 members) is characterized by generally weaker teleconnectivity values. Still, a weak NAO-like teleconnection as well as a weak zonal dipole structure from the Mediterranean to the central North Atlantic are visible. Especially the southern part of the area experiences high variability (Fig. 6.8f), suggesting an overall bad agreement among the cluster members.

Cluster 4 (Fig. 6.8g, 425 members) strongly differs from the clusters 1-3, as it is the only one which is not characterized by clear teleconnection structures. The teleconnectivity generally increases going from south to north, and the spacious, blurred regions of enhanced teleconnectivity also suggest very diverse members of the fourth cluster.

Overall, cluster 1 and 2 show strong and well-separated meridional teleconnections associated with the NAO, and resemble composite 1 and 2 of the *pc*-based classification. Even though cluster 3 contains only 96 time steps and exhibits strong variability, it still has two distinct centers of action, associated with a mixture of zonal and meridional teleconnections. Cluster 4 includes many time steps (425), but is not characterized by centers of action, suggesting that this cluster contains many differing time periods.

Classification with teleconnection axes

This classification approach uses the teleconnection axes of the single teleconnectivity fields to group the periods into different classes. In doing so, different boxes which show a high teleconnection activity within the North Atlantic domain are selected by analyzing single teleconnectivity fields visually. Then, typical teleconnections (e.g. the NAO or the EA) are assigned to one or more pairs of boxes and an algorithm detects if at least one teleconnection axis connects a box pair with each other. In Fig. 6.9, the chosen boxes and their typical connections are mapped, and Tables 6.1 and 6.2 give the exact borders of the boxes. Fig. 6.9a shows the boxes and connections linked to meridional teleconnections, and Fig. 6.9b illustrates the boxes and connections associated with zonal teleconnections. Based on a visual examination of the single 30-year periods, the following 'typical' teleconnections were chosen:

- Only NAO: A period is grouped into the category 'Only NAO' if at least one teleconnection axis connects at least one box pair of the meridional boxes in Fig. 6.9a, and no connection exists between zonal box pairs (Fig. 6.9b).
- NAO and zonal: If at least one teleconnection axis between at least one meridional box pair and one or more teleconnection axes between at least one zonal box pair is present, the corresponding time step is classified into the 'NAO and zonal'-category.
- Only zonal: A period is grouped into the 'Only zonal'-group if at least one teleconnection axis connects at least one box pair of the zonal boxes and no connection exists between

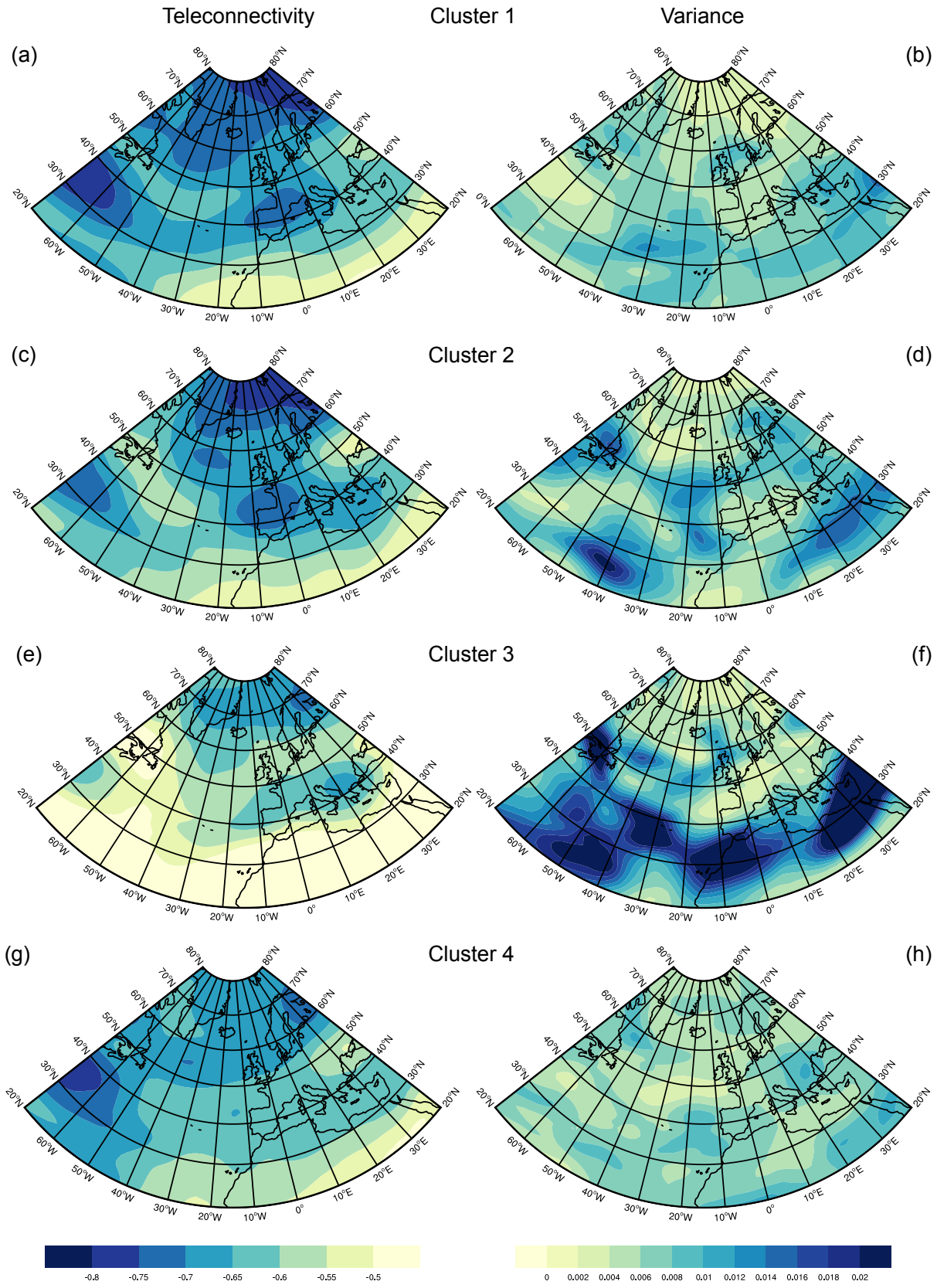

Figure 6.8: Composites of the clustered teleconnectivity fields (a, c, e and g) and the corresponding variances (b, d, f and h). Cluster 1 has 460 members, Cluster 2 240, Cluster 3 96 and Cluster 4 425.

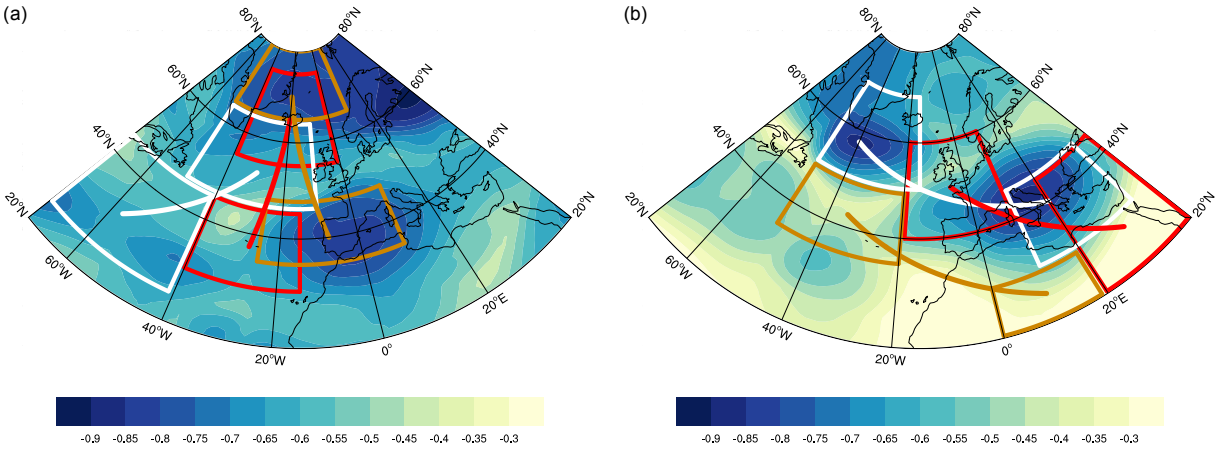

Figure 6.9: Box definitions for typical meridional (a) and zonal (b) teleconnections in the North Atlantic sector. The teleconnectivity fields are from the periods 1621-1650 (a) and 1231-1260 (b). The exact coordinates are listed in tables 6.1 and 6.2.

meridional box pairs.

- Nothing: If no connection between either meridional or zonal box pairs exist for a time step, it is grouped into the class 'Nothing'.

Obviously, this approach cannot take all teleconnections into account. For example, an eastern meridional connection from the Mediterranean to north of Scandinavia, is not represented by this method. Further, there will be no distinction between e.g. a western branch of the NAO, the 'classic' NAO or the eastern NAO, as the three boxes are combined to the category 'NAO'. However, the idea of such an approach is to reduce the complexity of a large dataset, which is accomplished by generating the four groups 'Only NAO', 'NAO and zonal', 'Only zonal' and 'Nothing'.

The composites of this classification and the variances of the members of each class are depicted in Fig. 6.10. Fig. 6.10a shows a distinct meridional pattern with the centers of action north-east of Iceland and over the Iberian Peninsula and the adjacent Atlantic Ocean. A strong center is also visible in the south-western edge of the domain, linked to the northern white box (Fig. 6.9a). The variance (Fig. 6.10b) increases from north to south and from east to west, but is generally rather low.

Table 6.1: Coordinates of the meridional boxes from Fig. 6.9a.

Box name	Color	Longitude	Latitude
nao south	red	40° W - 15° W	30° N - 45° N
nao north	red	40° W - 0° E	57.5° N - 75° N
nao_west south	white	70° W - 40° W	25° N - 45° N
nao_west north	white	50° W - 10° W	45°N - 65° N
spain	orange	25° W - 10° E	35° N - 47.5° N
north	orange	50° W - 0° E	65° N - 85° N

Table 6.2: Coordinates of the zonal boxes from Fig. 6.9b.

Box name	Color	Longitude	Latitude
south-east_1	white	10° E - 35° E	50° N - 70° N
north-west	white	50° W - 15° W	15° N - 30° N
south-east_2	red	20° E - 45° E	15° N - 40° N
central	red	20° W - 10° E	30° N - 45° N
south-east_3	orange	0° E - 20° E	15° N - 30° N
central-west	orange	50° W - 20° W	35° N - 50° N

The composite of the group 'NAO and zonal' (Fig. 6.10c) shows, as expected, meridional and zonal structures, the latter reaching from the eastern Mediterranean to the central North Atlantic/Great Britain. Fig. 6.10d indicates that the variance of this class is also low, especially in the regions of the central centers of action. The slightly increased variability near 30° E, 45° N indicates that the south-eastern center of action of the zonal teleconnection is exposed to enhanced variability.

Fig. 6.10e shows the composite of the time steps grouped into the category 'Only zonal', where the centers of action are located in the Mediterranean and over the central North Atlantic/Great Britain. The teleconnectivity is still enhanced in the northern and south-western North Atlantic, but the connections come from regions not defined in the boxes, such as e.g. the eastern Mediterranean or outside of the domain. The variance (Fig. 6.10f) has two strong maxima, and one is located within the eastern red box (Fig. 6.9b), suggesting that the variability of this center of action is higher than the one of the center of action associated with the south-eastern white box (north-west of the red box).

The composite field of the category 'Nothing' has a strong minima in the south-western and north-eastern edge of the domain (Fig. 6.10g). The weak center of action over Europe is linked either to the one in the north-east, or to the one south of Greenland, as an investigation of the single members yields (not shown). These two connections are not represented by one of the boxes. The variability is very high in the south and over Newfoundland, while the northern regions are more stable (Fig. 6.10h).

As this classification method is based on previously selected teleconnections, it is clear that every group represents specific patterns. 71% of the time steps are characterized by NAO-like structures (classes 'Only NAO' and 'NAO and zonal'), 43% show zonal teleconnections, and 15% do not show any connection associated with the defined boxes.

Using these box definitions, indices describing the strength of teleconnectivity of each box pair can be calculated to derive a temporal representation of spatial changes. The indices between each box pair are calculated as the sum of the average teleconnectivity values of the two boxes:

$$I(t) = |[T(t)]_{box1} + [T(t)]_{box2}|, \tag{6.1}$$

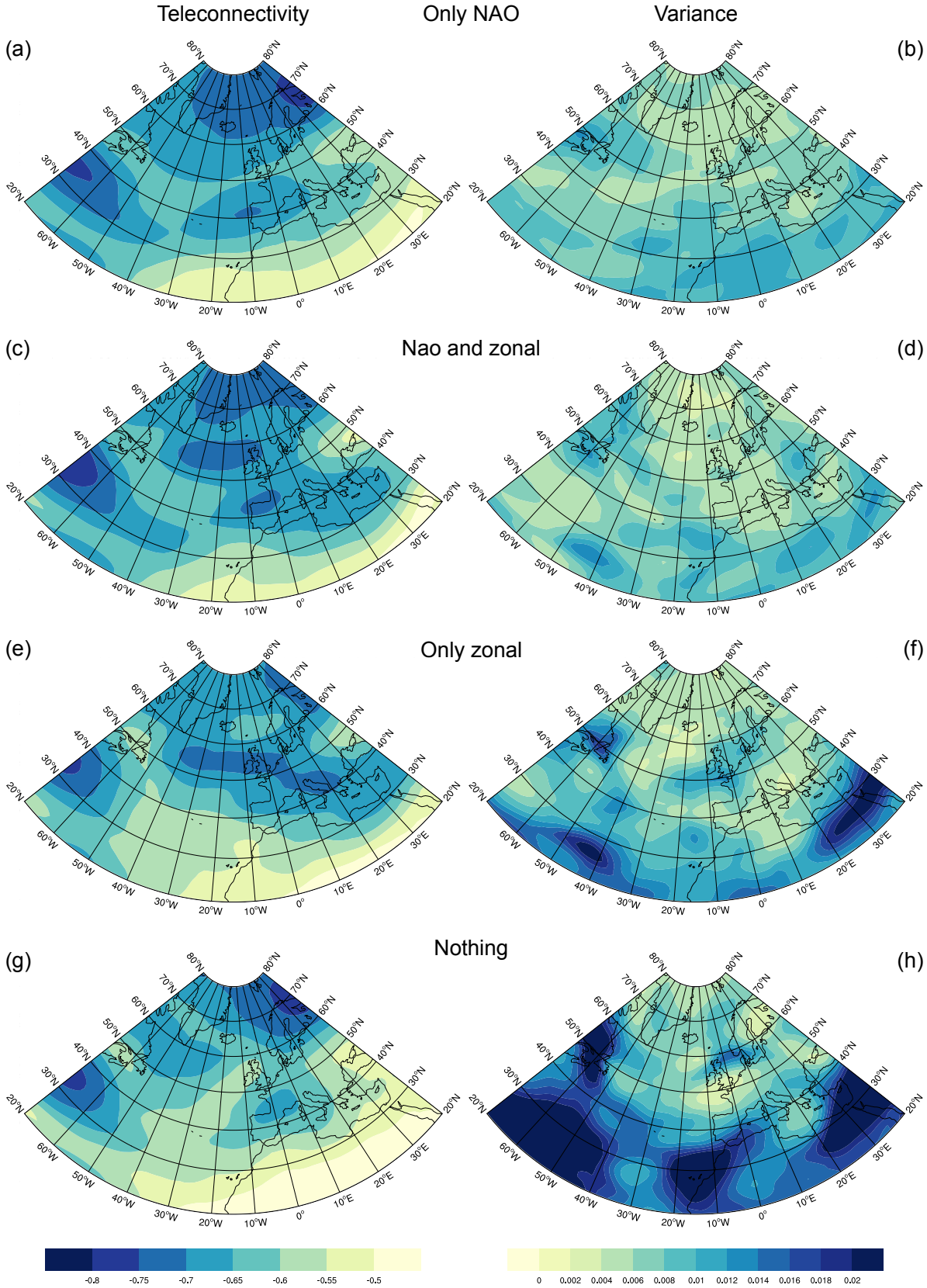

Figure 6.10: Composites of the teleconnectivity fields belonging to the groups 'Only NAO' (a, 515 members), 'NAO and zonal' (c, 358 members), 'Only zonal' (e, 164 members) and 'Nothing' (g, 184 members), and the corresponding variances (b, d, f and h).

where $T(t)$ corresponds to the teleconnectivity value at a specific 30-year time period and $[T(t)]_{box}$ to its spatial mean in the related box. Note that the absolute values are chosen such that high values correspond to strong teleconnectivity and low values to weak teleconnectivity. Finally, the index is normalized:

$$I_{norm}(t) = \frac{I(t) - \overline{I}}{\sigma(I)}. \tag{6.2}$$

These indices are not calculated for the four categories 'Only NAO', 'NAO and zonal', 'Only Zonal' and Nothing', because the averaging would be performed over too many points. Instead, all the boxes depicted in Fig. 6.9 are used. Note that the box 'spain' is divided into an easterly box (still called 'spain') and a westerly box (from now on called south-east Atlantic, 'sea'), and they both connect to the northern box. Hence, we obtain 7 indices from 7 box pairs, which are shown in Fig. 6.11. The red dots in every panel indicate that at least one teleconnectivity axis connects the two associated boxes, and the index line is colored red at time steps where a teleconnection axis was detected.

For the most part, high index values come along with the occurrence of teleconnection axes between the related boxes, and low values are associated with gaps in the connection time series. Nevertheless, mismatches are also present where low values are accompanied by connections and vice versa. The indices 'nao', 'sea_n', 'nao_west', 'se1_nw' and to some extent 'se2_c' (Fig. 6.11a, c, d, e and f) are characterized by phases of prolonged high values and connections, which alternate with long-lasting periods of low values and absence of connections. On the other hand, the connections of 'sp_n' and parts of 'se2_c' (Fig. 6.11b and f) are not preserved over longer periods, but strongly fluctuate. It is striking that all indices, especially the zonally oriented and nao_west (6.11d-g), show a distinct drop between 1240 and 1260, which implies that during this period, very low teleconnectivity is present. Exemplary for this period, the teleconnectivity map of the 30-year period 1255-1284 is depicted in Fig. 6.13, which is characterized by overall low teleconnectivity values and no teleconnection axes. Starting at the drop and lasting until ca. 1350, the meridionally oriented indices are characterized by low values and few connections (Fig. 6.11a-d). In contrast, the indices 'se1_nw' and 'se2_c' quickly increase after the drop and show consecutive periods with connections. Table 6.3 shows that the meridional indices (Fig. 6.11a-d) are highly correlated among each other (except for 'nao_west'), and less correlated with the zonal indices (Fig. 6.11e-g).

Fig. 6.12 gives a condensed overview over the connections between the box pairs. In contrast to Fig. 6.11, where every teleconnection axis between the related boxes are marked by a red point, only time steps with connections which are part of a period with at least 10 consecutive connections are drawn. This representation emphasizes the different occurrences of teleconnections between the box pairs. For example, it is clearly visible that the connections of the box pair 'sp_n' are very short-lived, as only four periods with at least 10 consecutive teleconnections exist. In contrast, 'sea_n' has not only more, but also long-lived connections. Further, the figure illustrates that most of the box pairs have prolonged periods with present and absent teleconnections. For example, 'nao' has many long-lived teleconnection axes between 850 and

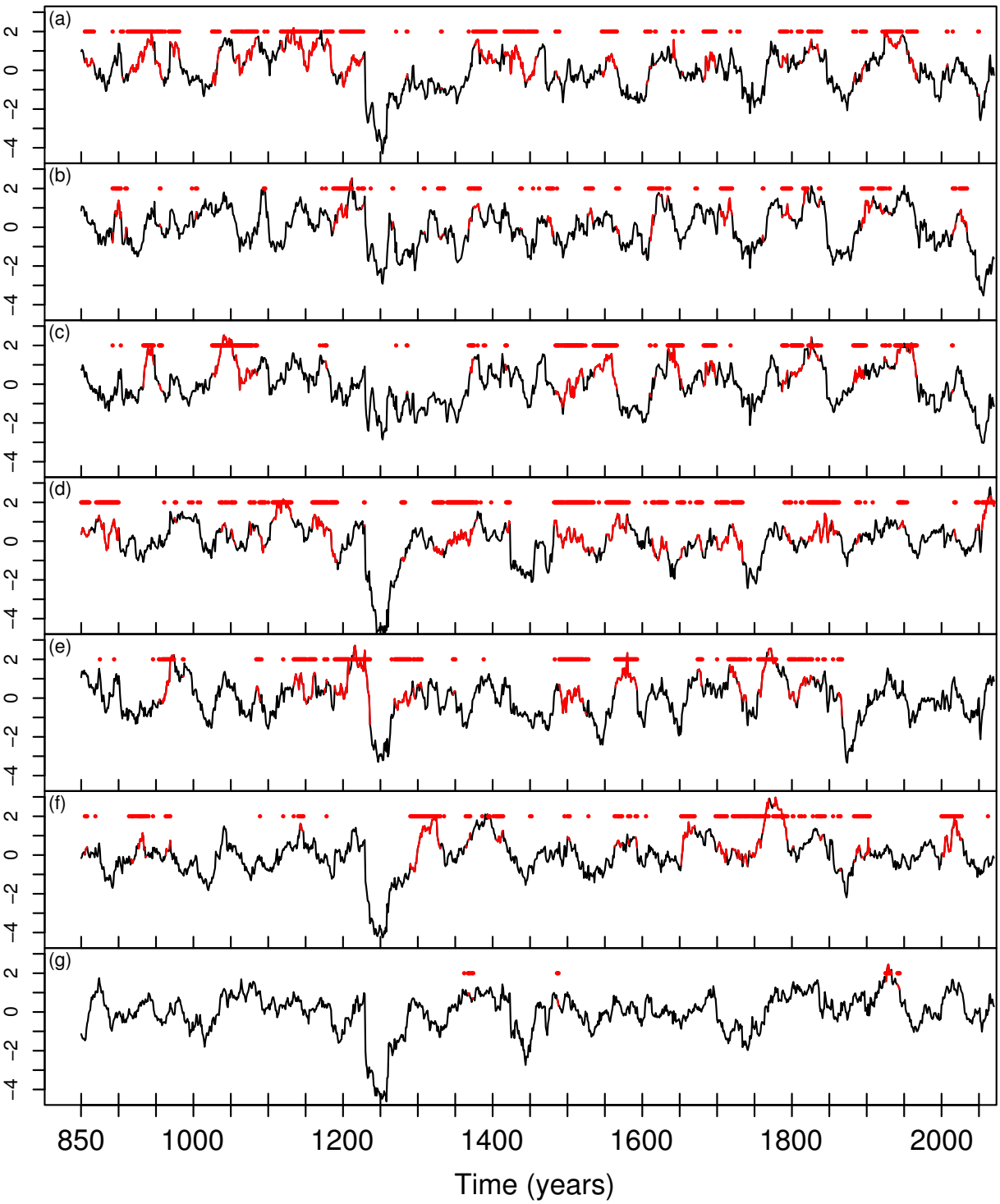

Figure 6.11: Indices describing the strength of teleconnectivity between the box pairs 'nao' (a), 'sp_n' (b), 'sea_n' (c), 'nao_west' (d), 'se1_nw' (e), 'se2_c' (f) and 'se3_cw' (g). The red dots and the red colored sections of the indices label time steps where teleconnection axes between the box pairs were detected.

Table 6.3: Correlation coefficients between the 7 indices

	nao	sp_n	sea_n	nao_west	se1_nw	se2_c	se3_cw
nao	1	0.65	0.83	0.56	0.44	0.47	0.63
sp_n	0.65	1	0.79	0.23	0.42	0.42	0.32
sea_n	0.83	0.79	1	0.23	0.19	0.32	0.44
nao_w	0.56	0.23	0.23	1	0.62	0.51	0.71
se1_nw	0.44	0.42	0.19	0.62	1	0.64	0.4
se2_c	0.47	0.42	0.32	0.51	0.64	1	0.62
se3_cw	0.63	0.32	0.44	0.71	0.40	0.62	1

1200, but none between 1200 and 1300.

6.2.3 Comparison of the classifications

Pattern correlation classification vs K-means Clustering

Composite 1 of the PC-classification and Cluster 1 are rather similar, as they both show a strong NAO-like variability. Composite 2 and Cluster 2 also match well, with meridionally oriented NAO-like centers of action and the zonal teleconnections from south-east of southern Greenland to the Mediterranean. Cluster 3 matches the most with composite 1 and 2, while it is not possible to visually assign Cluster 4 to one of the PC-composites. In Fig. 6.14, the counts of assignments to one of the four PC-categories is shown for the time steps that have been assigned to each of the four clusters. Most of the time steps that are related to Cluster 1 are assigned to either PC-category 1 (184) or 2 (209). 62 time steps of Cluster 1 are associated with the third PC-category, and 5 time steps are assigned to PC-category 4. This is in accordance with the visual comparison of the composites of the PC-classes 1 and 2 and Cluster 1, as all of them are mainly dominated by a meridional, NAO-like teleconnection.

112 periods associated with Cluster 2 are assigned to PC-category 2, and 67 and 57 periods belong to PC-category 3 and 1, respectively. Again, only very few time steps correspond to

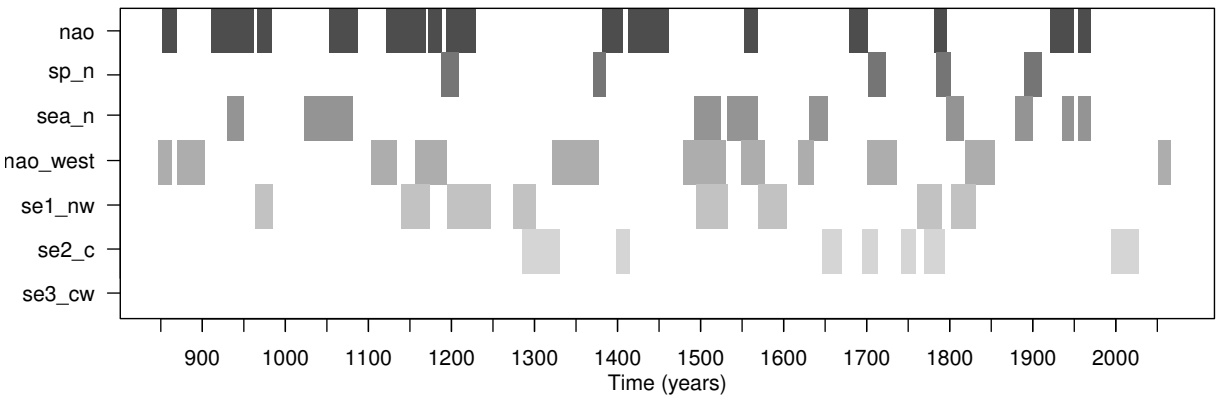

Figure 6.12: Time steps which are part of at least 10 consecutive time steps with connections between the box pairs 'nao', 'sp_n', 'sea_n', 'nao_west', 'se1_nw', 'se2_c' and 'se3_cw'.

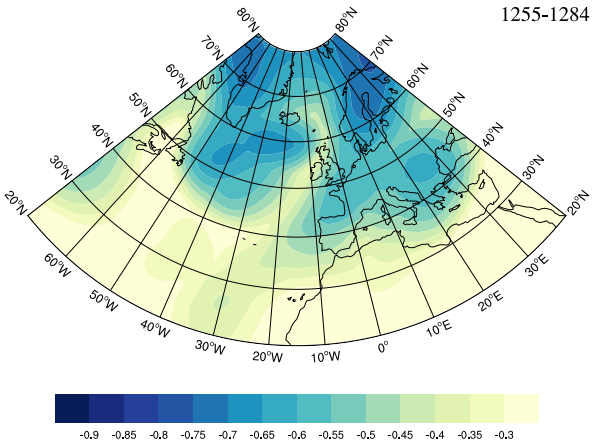

Figure 6.13: Teleconnectivity map of the 30-year period 1255-1284. This map is exemplary for the period of low overall teleconnectivity and few teleconnection axes between 1240 and 1260 (when taking into account the 30-year periods 1289).

PC-category 4 (4) . This agrees well with the structures observed on the composite maps. Both Cluster 2 and the composite of PC-category 2 show a mixture of NAO-like variability and zonal teleconnections, PC-class 1 is more meridionally oriented and PC-class 3 more zonally. Cluster 3 is the category with the least time steps (96). Most of them are classed into PC-category 1 (54), 34 are in PC-category 2, and 8 belong to the third category. None are categorized into the fourth class. As cluster 3 is mainly characterized by meridional variability, the PC-categories 1 and 2 match the classification. The bulk of the time steps associated with Cluster 4 are within PC-categories 3 (150) and 2 (147). Almost all time steps from PC-category 4 (90) are in Cluster 4, and 38 periods are associated with PC-category 1. This shows that Cluster 4 is characterized by a mixture of NAO- and zonal variability, and explains why its composite is blurred in such a way.

Teleconnection axes classification vs Pattern correlation classification

The time steps associated with PC-category 1 are mostly within the 'Only NAO'-category (164), and the categories 'NAO and zonal' and 'Nothing' receive 92 and 64 time steps, respectively (Fig. 6.15). The category 'Only zonal' is underrepresented with only 8 time steps. As PC-category 1 is characterized by a NAO-pattern, the two classification methods match quite well. Also the second PC-category is dominated by the 'Only NAO'-category (215) and the 'NAO and zonal'-category (145), while 'Only zonal' and 'Nothing' share 68 and 74 time steps with PC-category 2, respectively. The composite of PC-category 2 shows a mixture between NAO-

Table 6.4: Membership counts of the different classification methods. C1-C4 represent the composites of the classification methods in the plotted order.

Classification method	C1	C2	C3	C4
Pattern correlation	333	502	287	99
K-means cluster	460	240	96	425
Box- and axes-based	515	358	164	184

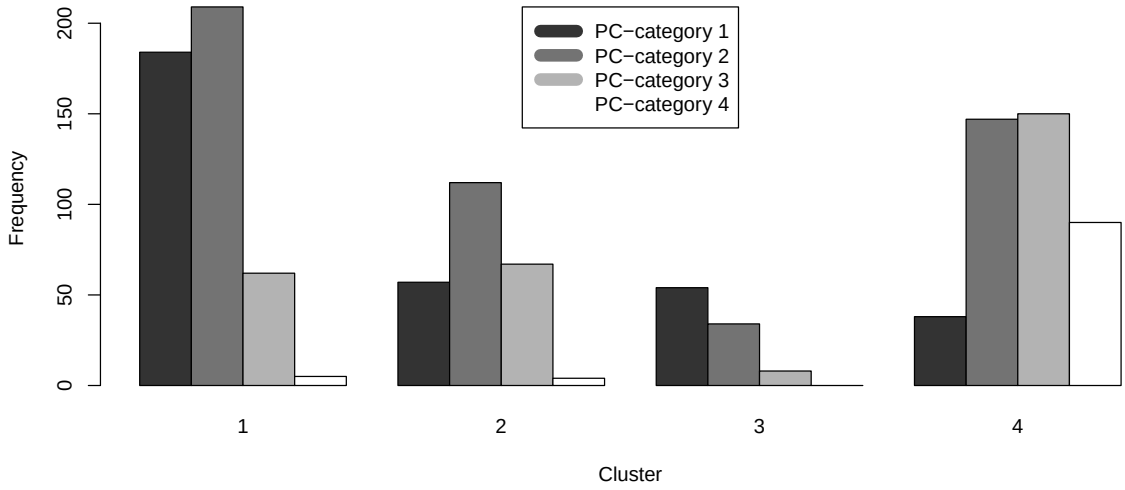

Figure 6.14: Membership of time steps classified by the pattern correlation method to the four clusters.

like variability and zonal teleconnections. Therefore, the distribution of the time steps in the axes classification makes sense, especially when taking into account that the category 'Only zonal' contains only 164 time steps in total. Most time steps lying within the third PC-group are categorized into 'Only NAO', but there exists no clear dominance. Composite 3 of the PC-classification is zonally oriented with some NAO-like variability. It therefore makes sense that a large fraction of the 'Only zonal'-intervals (37%) is associated with this PC-group, while only 21% are within the 'Only NAO'-group. The fourth PC-category has only very few time steps, which are uniformly distributed among the groups 'Only NAO', 'NAO and zonal' and 'Only zonal'.

In summary, the category 'Only NAO' dominates in all PC-categories (except category 4). The category 'NAO and zonal' also has many occurrences in all PC-categories. This dominance partly arises from the inclusion of the box pair 'nao_west' into the 'NAO'- category, as it is the second most frequent teleconnection (Fig. 6.12). Based on this approach, during most of the time (71% of all time steps), the North Atlantic sector is characterized by one or more meridional teleconnections, while only 43% of the time steps show zonally aligned anti-correlations.

6.2.4 Discussion

All of the above applied classification methods are subjected to limitations. The pattern correlation classification is a very simple approach, using the mean pattern correlation value of a 30-year teleconnectivity period with all other time intervals. The method relies on the assumption that time intervals with a similar mean pattern correlation with all other time intervals show similar spatial patterns. The major shortcoming about this method is that even though the pattern correlation between two frames is high, the spatial structures of the two frames

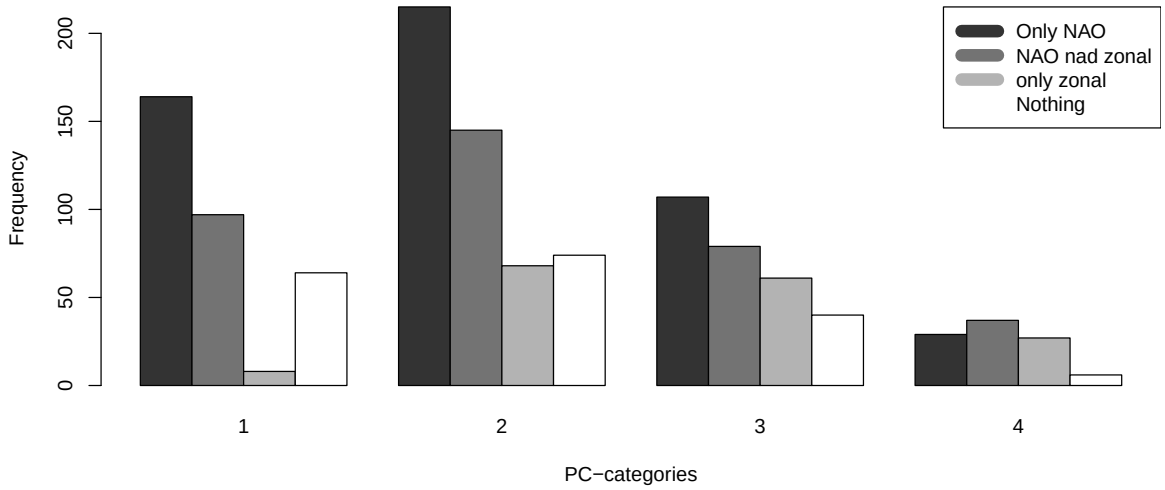

Figure 6.15: Membership of time steps classified by means of the teleconnection box classification to the four PC-categories.

are not necessarily similar. Further, the teleconnectivity axes that determine which regions are connected by teleconnections are not taken into account. Fig. 6.16 shows two examples for misclassifications made by this method. The time interval 1234-1263 (a) shows a very strong zonal teleconnection from south of Greenland to eastern Europe, the interval from 2070-2099 (b) is characterized by a meridional teleconnection from the south-western edge of the domain to the central North Atlantic. Even though the two intervals differ visually from each other (and would be classified into the groups 'Only zonal' and 'Only NAO' by the axes-based method), they are both grouped into the same class (in this case PC-class 1), because they both have a mean PC-value larger than 0.4. The opposite situation, where two periods with a similar structure are grouped into different classes, also occurs (c and d). Both intervals show zonal teleconnection(s) in the eastern and western parts and meridional teleconnections in the central part, and would be grouped into the 'NAO and zonal'-group by the axes-based classification. While the period 1306-1335 is assigned to PC-group 4 (PC = 0.08), the period 1890-1919 is a member of PC-group 3 (PC = 0.21).

Also the k-means clustering results in misclassifications, which gets obvious when analyzing the composite maps of the four clusters (Fig. 6.8). While the composites of the first and second cluster represent nicely separated, mostly zonal teleconnections, especially cluster 4 is rather blurred, indicating that many different patterns were assigned to it. Hence, the k-means clustering with $K = 4$ does not satisfactorily classify the teleconnectivity maps. The choice of a higher number of clusters is possible, but the slow increase of EV and SI with growing K (Fig. 6.7) suggests that a larger number of clusters is necessary to obtain significantly better results. However, having a high number of clusters is against the idea of reducing the complexity of the data set. Furthermore, a comparison with the other two methods would be hindered.

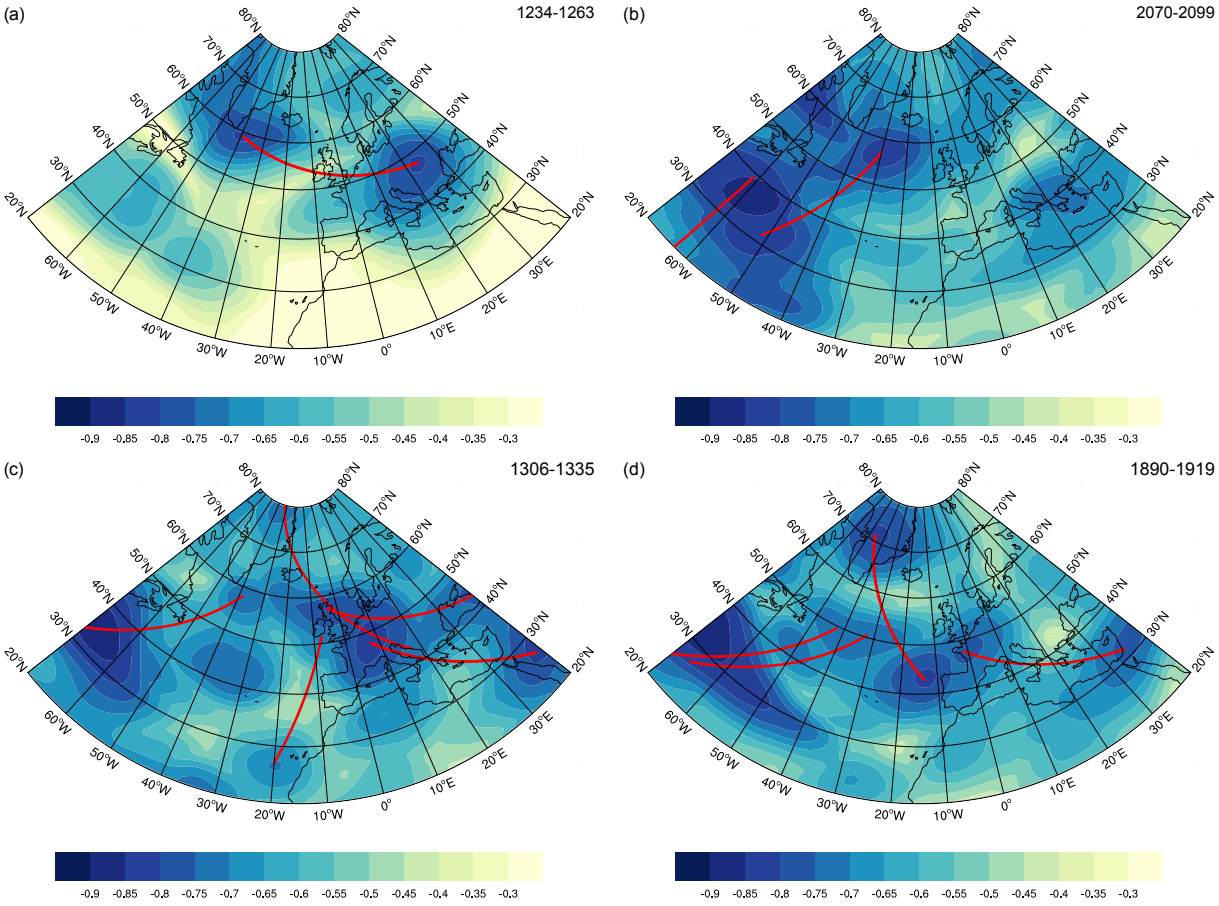

Figure 6.16: Single teleconnectivity maps with teleconnectivity axes of the periods 1234-1263 (a), 2070-2099 (b), 1306-1335 (c) and 1890-1917 (d) in the North Atlantic sector, indicating misclassifications of the pattern correlation assignments.

The intuitive choice of boxes lying within areas of high teleconnection activity is exposed to shortcomings as well. Firstly, this method is based on the presence or absence of teleconnectivity axes, which are defined by an arbitrarily chosen threshold. Therefore, an interval can be assigned to a certain class because a teleconnection axis connects two grid points with $T = -0.71$, and two grid points located in boxes associated with another class are not connected by a teleconnection axis, because they have values slightly higher than -0.7. Moreover, also the boxes are defined arbitrarily, as the border has to be set at some point. That is why this method can not group all time steps with similar spatial patterns into the same group. Finally, the number of groups would need to be higher, if the spatial variability of the Euro-Atlantic climate shall be resolved better. The subdivision of only one group into two, such as for example 'NAO' into 'Western NAO' and 'Eastern NAO', increases the number of groups from 4 to 7. Similar to the cluster analysis, the consideration of one more group does add only little more information, while the complexity increases at a higher rate.

Changing teleconnection structures in the North Atlantic sector have been diagnosed in several studies with different methodologies and on different time scales, and the bulk of them agrees on the non-stationarity of centers of action of the NAO (e.g. *Ulbrich and Christoph* 1999;

Raible et al. 2006; *Moore et al.* 2013; *Raible et al.* 2014). In *Raible et al.* (2014), a pattern correlation approach similar to the pattern correlation classification used in this thesis has been applied to detect structural changes in the modeled and observed North Atlantic climate variability. They found that high pattern correlation values are associated with patterns similar to the observations, and low pattern correlation values come along with structural changes depending on the climate model, such as e.g. the disappearance of the NAO-like pattern over Europe. In contrast to the results obtained from the pattern correlation classification in this study, no situations showing only zonally oriented teleconnections and no NAO-like pattern (such as composite 4 in Fig. 6.6g) are described. These discrepancies might arise from the different references used to compute the pattern correlations (observed pattern vs. modeled pattern). In another study, *Raible et al.* (2006) made use of the teleconnectivity axes to identify changing climate variability in the Euro-Atlantic region. There, periods with zonal and/or meridional connections were found with very stable periods alternating with unstable ones. This agrees with the analysis of the temporal occurrence of teleconnection axes between predefined boxes conducted in this thesis. However, the absence of teleconnection axes over a prolonged period and generally low teleconnectivity values throughout the entire North Atlantic region, as in the period from 1240-1260 (Fig. 6.11), is not reported in *Raible et al.* (2006) and *Raible et al.* (2014). The pattern correlation approach (neither with the observed nor with the modeled references, Figs. 6.3 and 6.5) in this thesis did not account for this extraordinary period of low teleconnection activity as well, which shows that this method is defective.

Another approach is used in *Wang et al.* (2012), where the angle of a line connecting the NAO-centers of action (derived from EOF-analysis) with the meridians is used to compute an index. This index then describes the zonal displacements of the centers of action relative to each other. Applied to reanalysis data over 140 years, *Wang et al.* (2012) found multi-decadal variability of this index, which generally agrees with the findings in this thesis. However, the angle-index is applied only to EOF1-data, for which reason the results are limited to the NAO.

Chapter 7

Drivers of the North Atlantic climate variability

Based on the results and analyses concerning the spatial variability of the North Atlantic teleconnections from section 6.2, linkages between different components of the climate system are investigated. In the scientific literature, many different processes driving the temporal variations of the NAO on different time scales are discussed, amongst others the coupling between the NAO and the ocean (SST) and the sea ice distribution. However, the factors controlling the spatial variability of the NAO-centers of action are hardly considered. In the following, composite maps of the global SST and the sea ice edge in the North Atlantic are shown for situations when specific teleconnections are present. In doing so, SST- and sea ice patterns occurring during periods of different teleconnections shall be identified, which are used to hypothesize couplings. Ideally, different patterns of SST and the sea ice edge are found for the meridional and zonal teleconnections. Then, indices describing the North Atlantic climate variability derived from the classifications from section 6.2.2 are used for linear regression analysis with SST and the sea ice edge in order to evaluate if a linear relationship exists. The analysis in this chapter is conducted for winter mean (DJF) only, because it is based on the results from section 6.2, which is limited to winter. Additionally, the period 1850-2099 is omitted, as both SST and the sea ice extent show a strong response to the anthropogenic warming signal since 1850.

7.1 Connection to the ocean

When dealing with long-term variability of the atmospheric circulation, the role of the ocean has to be considered, because the inertia of the ocean allows for couplings to the atmosphere on various time scales. To get an idea about the SST-variations in the North Atlantic during the last millennium in the CESM-simulation, the time series of the 30-year running mean winter (DJF) SST-anomalies averaged over the southern (20°-40° N), middle (40°-60° N) and northern (60°-90° N) North Atlantic ocean are depicted in Fig. 7.1. The variations of the different parts of the North Atlantic mostly happen in phase, such as the major coolings around 1250 and 1450,

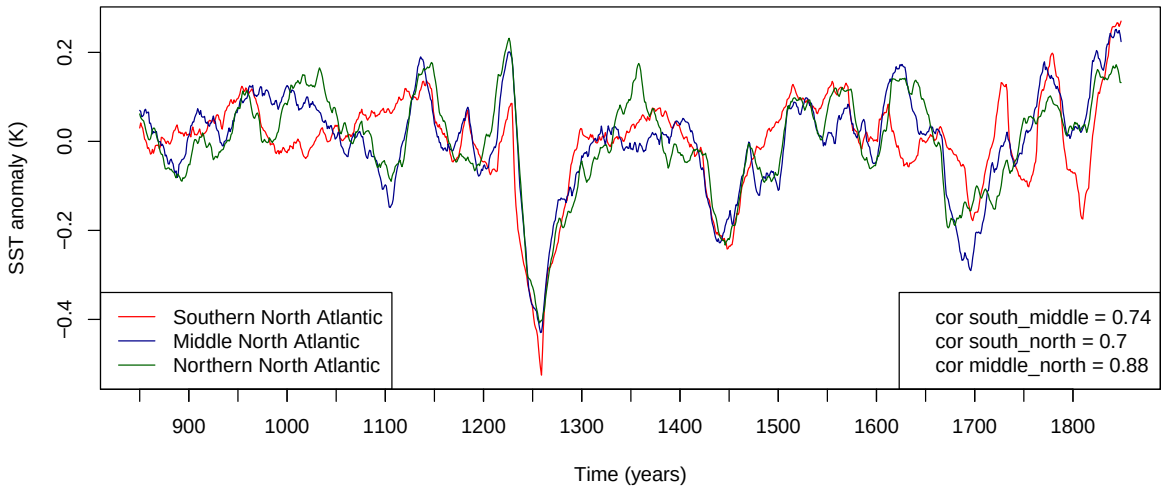

Figure 7.1: Time series of the area-averaged 30-year running mean winter (DJF) *SST*-anomalies in the southern (20°-40° N), middle (40°-60° N) and northern (60°-90° N) North Atlantic (100° W - 20° E).

which are driven by large volcanic eruptions and therefore occur on a global scale (Fig. 3.1 in chapter 3). But especially the southern North Atlantic *SST* is sometimes decoupled from the other two, e.g. between 1000 and 1150 or between 1700 and 1800, which is also reflected in the lower correlation coefficients. It is striking that the gap of teleconnections (Fig. 6.11) falls into the period of strong *SST*-cooling, induced by the volcanic eruption in 1257.

In a first step, the state of the global *SST* during the occurrence of the different teleconnections is analyzed. The composites of *SST*-anomalies computed with the classification 'Only NAO', 'NAO and Zonal', 'Only Zonal' and 'Nothing' derived in section 6.2.2 have very low magnitudes and only differ slightly from each other (not shown). This already hints that no clear *SST*-patterns are associated with the different states of North Atlantic climate variability. To consider as many situations as possible, composites are calculated on the basis of teleconnections of the seven box pairs presented in section 6.2.2. In order to take only longer-lasting periods into account, just time steps with connections being part of at least 10 consecutive 30-year periods with present connections (Fig. 6.12) are used to compute the composites.

In Fig. 7.2, these composite maps of the detrended global 30-year running mean *SST*-anomalies associated with teleconnections between the box pairs are shown. When a persistent NAO-like pattern is present, the global *SST*-anomalies are generally characterized by weak magnitudes (Fig. 7.2a). In the North Atlantic, a small minimum in the central part and slightly enhanced values east and west of the minimum are present. Negative *SST*-anomalies in almost the entire Northern Hemisphere are present during 'sp_n'-phases, with minimum values in the central North Atlantic ($<$ -0.2 K) and off the west coast of North America (Fig. 7.2b). In contrast, 'sea_n' -situations come along with opposite *SST*-anomalies, where mostly warm conditions are found in the central and northern North Atlantic as well as off the west coast of America

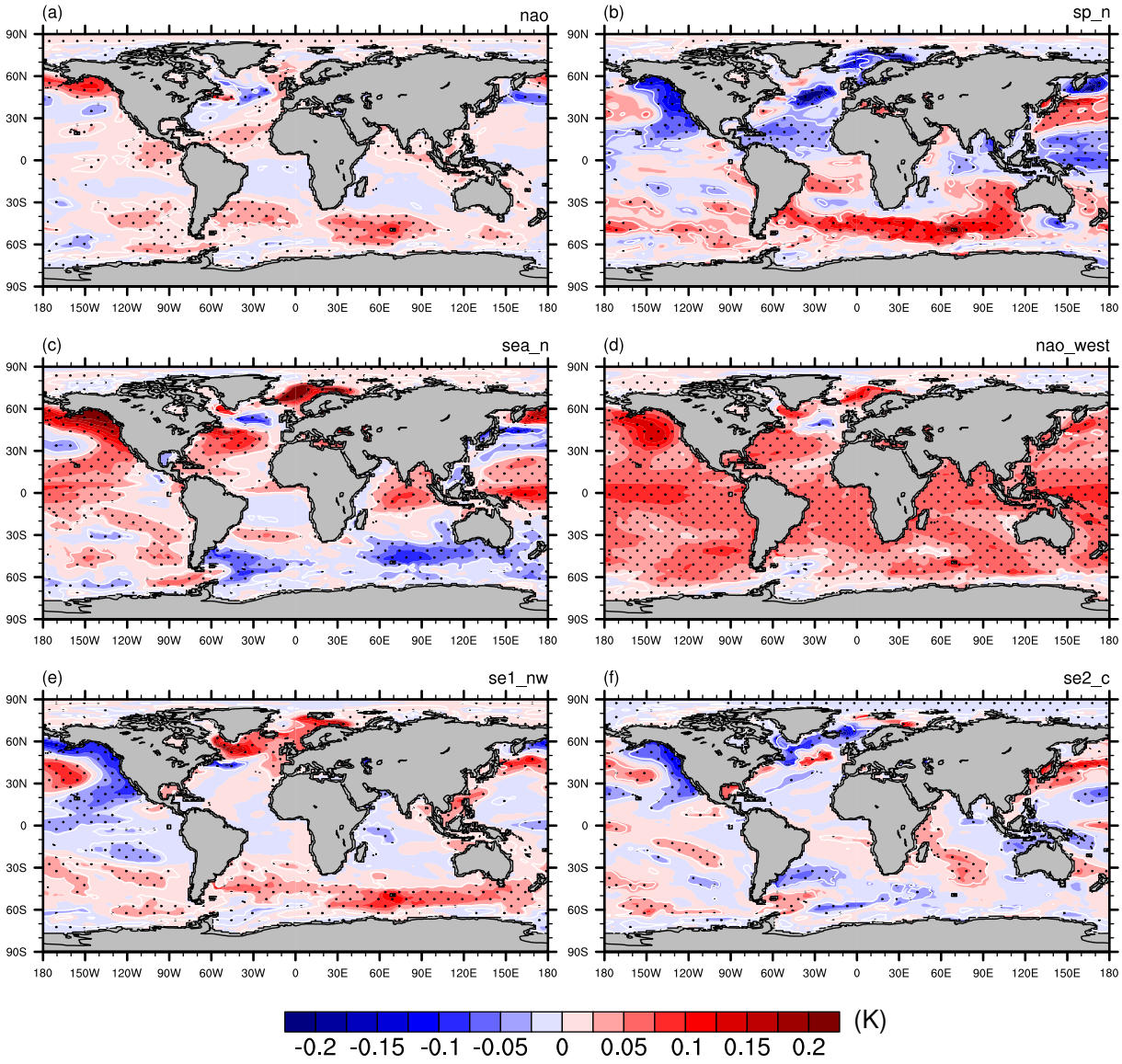

Figure 7.2: Composite maps of global detrended 30-year running mean winter (DJF) *SST*-anomalies calculated at time steps when teleconnection axes are present for at least 10 consecutive time steps between the box pairs 'nao' (a), 'sp_n' (b), 'sea_n' (c), 'nao_west' (d), 'se1_nw' (e) and 'se2_c' (f). The box pair 'se3_cw' is not shown because it has none of these periods. Stippled areas exceed the 95% confidence interval, calculated with a 2-tailed t-test. Note that only the period from 850-1849 has been taken into account to avoid an anthropogenic warming signal.

(Fig. 7.2c). *SST* during persistent 'nao_west'-phases are almost uniformly increased, except for a small area in the central North Atlantic (Fig. 7.2d). A warm northern North Atlantic and a cold eastern North Pacific is present during 'se1_nw'-phases (Fig. 7.2e), and 'se2_c'-connections are accompanied by a cool northern North Atlantic (Fig. 7.2f). All composites have in common that significant *SST*-anomalies do not only occur in the North Atlantic, but also at distant regions of the world. For example, in all panels of Fig. 7.2, relatively strong anomalies occur in the eastern North Pacific Ocean, and the anomalies are of equal sign as the ones in the North Atlantic during 'sp_n'-, 'sea_n'-, 'nao_west'- and 'se2_c'-situations (Fig. 7.2b,c,d and f) and of opposite sign during 'nao'- and 'se1_nw'-phases (Fig. 7.2a and e).

Although many of the anomalies are different from the background variations of *SST* at a confidence interval of 95% (stippled areas in Fig. 7.2), it is challenging to interpret the *SST*-composites, because the composites associated with the meridional (7.2a-d) and zonal (7.2e and f) teleconnections vary strongly among each other. Some similarities within the classes are found, such as cold anomalies in parts of the central North Atlantic during the presence of meridional teleconnections (a-d), or the sign of the anomaly in the eastern North Pacific, which is positive during meridional teleconnections (except 'sp_n') and negative during zonal teleconnections. But mostly, discrepancies prevail, which makes it difficult to hypothesize specific *SST*-patterns which are associated with the occurrence of either meridional or zonal teleconnections in the Euro-Atlantic sector.

To further investigate the relationship between the different teleconnections and *SST*, the indices describing the strength of each teleconnection (Fig. 6.11, equation 6.1) are used as predictors for linear regression analysis. The regression coefficient (rc) at the grid point i, j is calculated as

$$rc(i,j) = \frac{Cov(SST(i,j), I)}{\sigma(I)}, \tag{7.1}$$

where Cov denotes the covariance between *SST* and the index I. The resulting coefficient rc has the unit Kelvin, and corresponds to an index anomaly of 1 standard deviation (equal to 1, because the indices are normalized). Note that, in contrast to 'normal' teleconnection indices such as the Hurrell NAO-index, the indices used here do not make a statement about the phase of the teleconnection (such as e.g. NAO+ or NAO-), but rather indicate the strength of the teleconnection, independently of the phase. Therefore, the spatial patterns of the regression coefficients should resemble the composite patterns from Fig. 7.2, if *SST* and the strength of teleconnectivity in the North Atlantic are linearly related. The coefficients of the teleconnection indices regressed onto detrended *SST* from 850 to 1849 are shown in Fig. 7.3. The period from 1240 to 1270, during which the volcanic eruption from 1257 influences the 30-year means of *SST*, has been excluded from the analysis, because it strongly biases the regression coefficients towards positive values.

Each panel is characterized by mostly positive values of very low magnitude, suggesting that high teleconnection activity in the North Atlantic is linked to higher global *SST*, and low *SST*

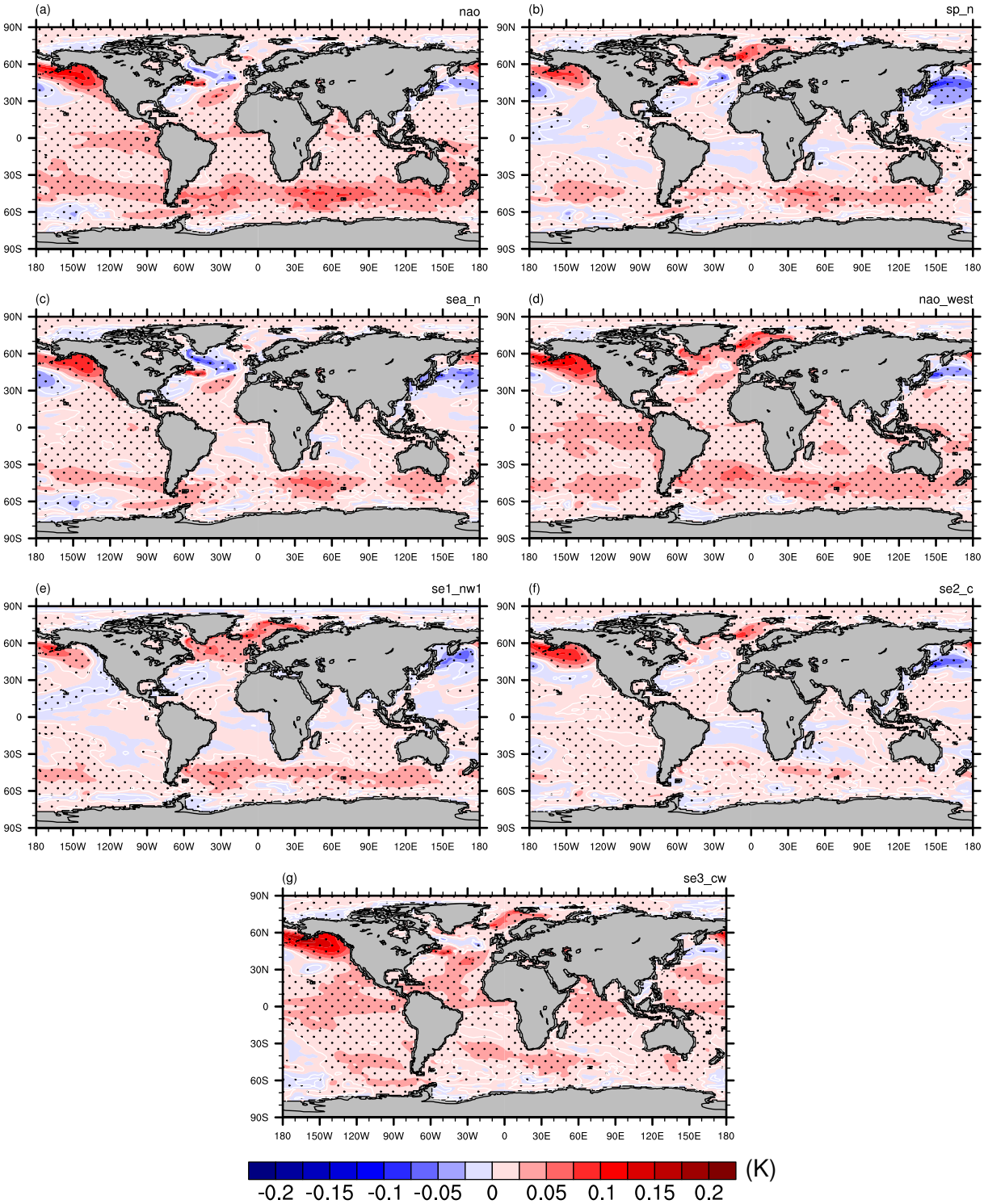

Figure 7.3: Regression of the teleconnectivity indices 'nao' (a), 'sp_n' (b), 'sea_n' (c), 'nao_west' (d), 'se1_nw' (e) and 'se2_c' (f) onto detrended North Atlantic *SST* from 850 to 1849. Units are in K and correspond to index anomalies of 1 standard deviation. Stippled areas exceed the 95% confidence interval, calculated with a 2-tailed t-test. The period from 1240 to 1270 is excluded from the analysis to eliminate the impact of the volcanic eruption.

is accompanied by low teleconnection activity. However, in the central North Atlantic, a negative relationship is evident for the indices 'nao', 'sp_n' and 'sea_n' (Fig. 7.3a-c). The highest magnitudes of the regression coefficients are located in the North Atlantic and in the eastern North Pacific, which is in agreement with the composites. This suggests a regional connection of North Atlantic *SST* and a hemispheric-scale coupling of the eastern North Pacific with the teleconnections. However, the signs of the regression coefficients in the North Pacific are positive for all indices and therefore do not match with the composites of 'sp_n', 'se1_nw' and 'se2_c' (Fig. 7.2b, e and f). Generally, it is astonishing that the regression coefficients (especially in the eastern North Pacific) have the same sign for all indices even though the very cold period from 1240 to 1270 with low teleconnectivity indices has been excluded. Hence, if there is a coupling with the eastern North Pacific, it cannot explain the different states of teleconnectivity in the North Atlantic, as the response is the same for all teleconnections. In the North Atlantic, the patterns of the regression coefficients and the ones of the composites are similar for the meridional teleconnections (Fig. 7.2a-d), with negative values in the central part surrounded by positive values (except for the composite of 'sp_n', Fig. 7.2b). This suggests that the NAO-like teleconnections favor cold *SST* in the central North Atlantic and argues for a regional coupling. However, the regression coefficients in the North Atlantic do not exceed ± 0.1 K per index anomaly. It is therefore questionable if these low magnitudes can effectively change the atmospheric circulation patterns in the North Atlantic. In the tropical parts of the Atlantic and Pacific, very low regression coefficients are present, hinting that no coupling with the tropical oceans exists.

This analysis does not allow for a reliable statement that particular *SST*-patterns favor a specific state of teleconnectivity (e.g. NAO-like or zonal) in the North Atlantic. Even though similar *SST*-structures in the North Atlantic are found for the meridional teleconnections, it is difficult to hypothesize a coupling, as the magnitude of the *SST*-signal is very low. In addition, the relatively high regression coefficients of same sign associated with all indices located in the eastern North Pacific raise the question if the regression analysis is biased by an unknown factor, similar to the volcanic eruption in 1257.

7.2 Connection to the sea ice extent

The extension of sea ice at high latitudes can alter the atmospheric circulation by changing the regional heat fluxes and thus can also influence teleconnections in the North Atlantic (e.g. *Nakamura et al.* 2015). Fig. 7.4 shows the long-term mean of the winter (DJF)- mean sea ice edge latitude (defined as the lowest latitude exceeding a sea ice cover of 50%) in the North Atlantic sector (65° W - 40° E). In the western part of the North Atlantic, the mean sea ice edge reaches further south (ca. 50° N) than in the eastern part. Starting from the east coast of Greenland, the mean sea ice edge shifts northward almost constantly until west of Svalbard, where the maximum latitude (ca. 78° N) is reached. This gradient is produced by the different ocean currents, which distribute the heat in the North Atlantic non-uniformly. Note that the gaps in the line

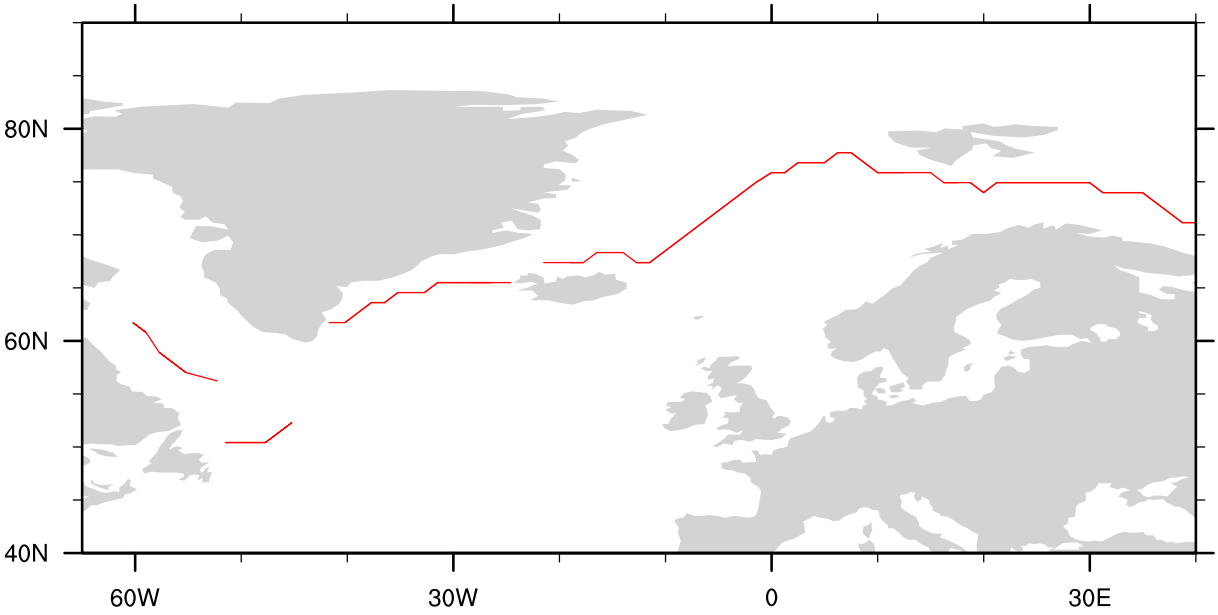

Figure 7.4: Climatology (850-1849) of the sea ice edge latitude in the North Atlantic (65° W - 40° E). Note that the gaps in the line are caused by the calculation of the sea ice edge latitude, which assigns one latitude value to each longitude. Therefore gaps arise when the sea ice edge 'turns around', as for example in the Labrador Sea.

are caused by the calculation of the mean sea ice edge, as every longitude can only hold one latitude value.

In order to assess the relationship between the North Atlantic sea ice and the teleconnections, the same procedure as for *SST* is applied. Firstly, composites of the anomalies of the 30-year mean sea ice edge latitude in the North Atlantic are shown during the presence of the different teleconnections (Fig. 7.5). Again, only time steps which are part of periods with at least 10 consecutive teleconnection axes between the box pairs are considered.

Between 65° and 45° W, the composites of the sea ice edge anomaly during persistent teleconnections vary strongly. All anomalies show a strong northward shift of 0.5° - 1.5°, except 'se2_c', which is characterized by a southward shift of ca. 1.5° (Fig. 7.5). The high amplitude in this small sector can mostly be explained by the problems which come along with the calculation of the sea ice edge. When the southern-most tip of the sea ice edge off the coast of Newfoundland (Fig. 7.4) extends very far eastwards, the sea ice edge latitude around 45° W takes the low value at ca. 50° N, because only the lowest value is taken by the calculation. On the other hand, the sea ice edge latitude at 45° W receives values around 60° N, when warmer conditions in the north-western North Atlantic prevail and the sea ice in the Labrador sea retreats. As *SST* associated with the teleconnection 'se2_c' are very low in the Labrador Sea (composites of *SST*, Fig. 7.2f), it is the only connection associated with a southward shift of the sea ice edge at 45° W. Therefore, we do not pay too much attention to these high amplitudes.

Between the east coast of Greenland and Iceland, the composites are almost equal with no vari-

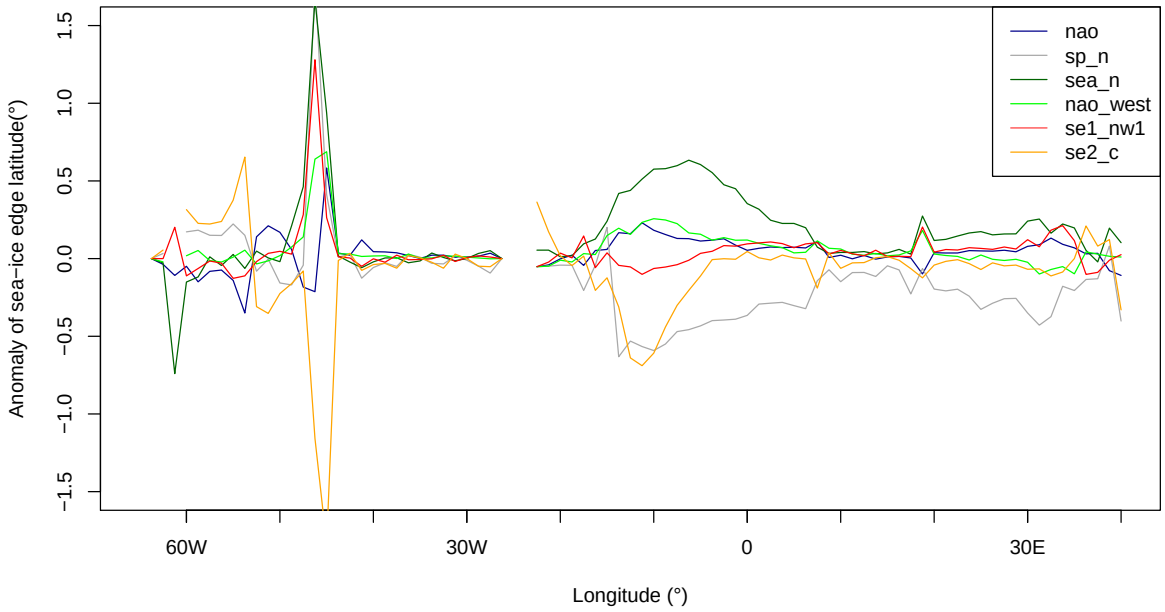

Figure 7.5: Composites of the 30-year running mean sea-ice edge latitude anomaly in the North Atlantic (65° W - 40° E) calculated at time steps when teleconnection axes are present for at least 10 consecutive time steps between the box pairs 'nao' (a), 'sp_n' (b), 'sea_n' (c), 'nao_west' (d), 'se1_nw' (e) and 'se2_c' (f). The box pair 'se3_cw' is not shown because it has none of these periods.

ations in the sea ice edge. In contrast, most of the composites show rather strong anomalies between 20° W and 10° E. The composite associated with connections of the box pair 'sea_n' is characterized by a northerly shift of the sea ice edge of about 0.75°, and the composites of the box pairs 'nao' and 'nao_west' show a similar behaviour, but with weaker amplitudes. The mean sea ice edge associated with teleconnections between the box pairs 'sp_n' and 'se2_c' is strongly shifted southwards, with a maximum amplitude of ca. 0.5°.

When comparing the sea ice edge anomaly composites with the *SST*-composites (Fig. 7.2), we note that the sea ice shifts are an imprint of the northern North Atlantic *SST*-anomalies. The anomalously cold *SST* in the North Atlantic during persistent 'sp_n'- and 'se2_c'-teleconnections match with the southward shifted sea ice edge, just as the warm conditions in the Northern North Atlantic during active 'nao'-, 'nao_west'- and 'sea_n'-phases with a retreat of the sea ice. This is obvious, because the sea ice extent is strongly coupled to high-altitude *SST*. It is therefore arguable if the composites of the sea ice edge are related to the different teleconnection states, or if they are driven by *SST* only.

The regression coefficients, obtained by regressing the indices describing the strength of the different teleconnections between the box pairs onto the 30-year running mean sea ice edge, are shown in Fig. 7.6a. The locations of the extrema are equal to the ones in Fig. 7.5, but they are mostly of positive sign, indicating a northward shift of the sea ice edge associated with

strong teleconnectivity, or a retreat of the sea ice during periods with low teleconnection activity in the Euro-Atlantic sector. Between 20° W and 10° E, this behaviour fits to the composites of 'nao', 'sea_n' and 'nao_west', but also 'sp_n' and 'se2_c' are associated with positive values, which have negative values in the composites. To assess the impact of the volcanic eruption in 1257, the regression analysis is also performed without the period 1240-1270, and the new regression coefficients are shown in Fig. 7.6b. Note that the scale is reduced by the factor 2. Between Iceland and Svalbard, a decrease of the amplitudes relative to Fig. 7.6a is observed, but the coefficients with 'sp_n' and 'se2_c' are still positive. Further, the p-value generally in-

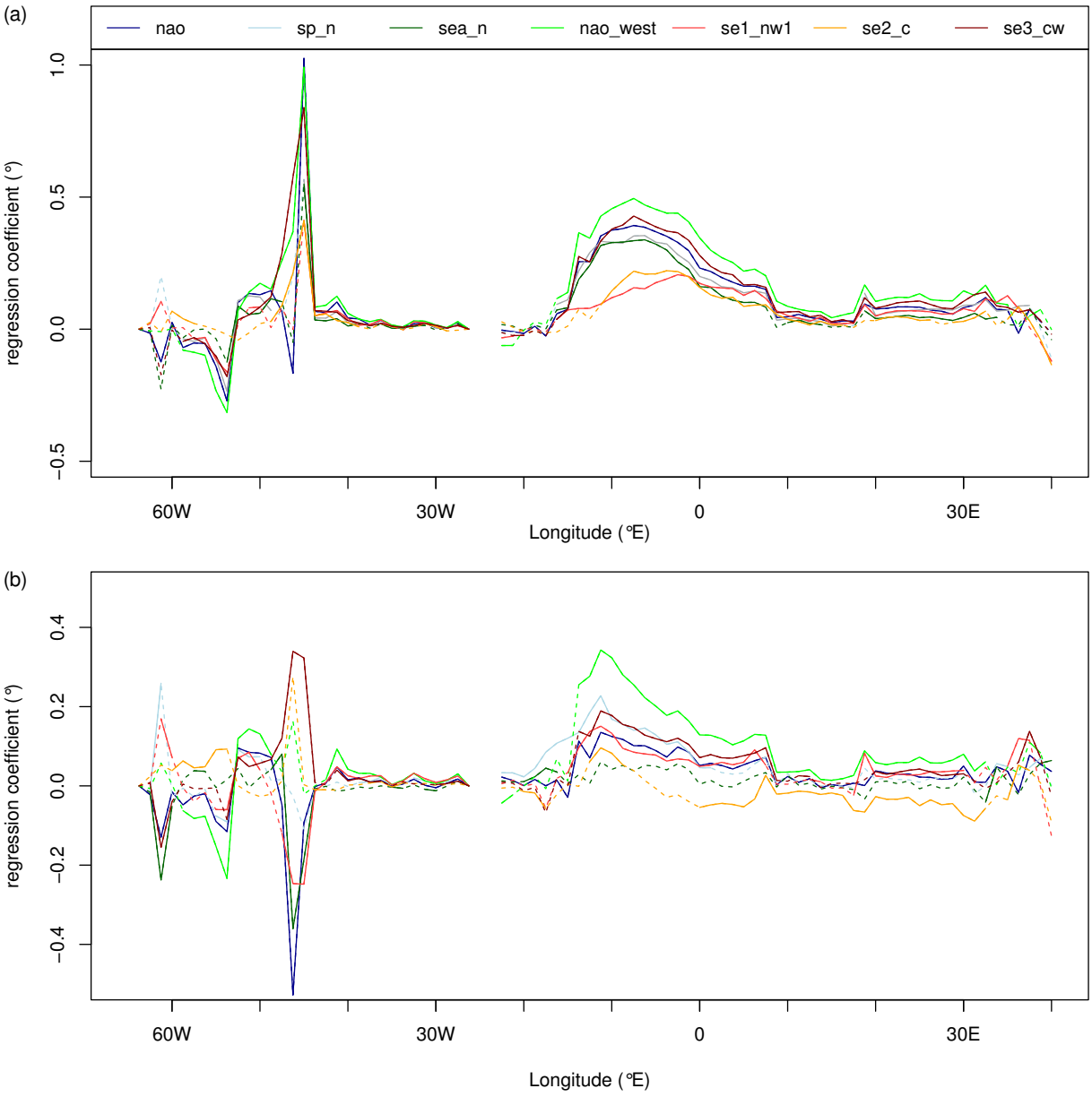

Figure 7.6: Regression of the normalized indices 'nao' (a), 'sp_n' (b), 'sea_n' (c), 'nao_west' (d), 'se1_nw' (e) and 'se2_c' (f) onto the sea ice edge latitude. The whole period from 850 to 1849 is used in panel a, and the period from 1240-1270 is excluded in panel b. Units are in ° and correspond to an index anomaly of 1 standard deviation. Dashed lines indicate regions which are below the 95% confidence interval, calculated with a 2-tailed t-test.

creases, with some parts being below the confidence interval (dashed lines). Therefore, the volcanic eruption strongly influences the result of the regression analysis.

Changes of the sea ice edge in the North Atlantic might affect the presence of different teleconnections in the North Atlantic sector, as the composites show substantial anomalies during the occurrence of different teleconnections. But the inconsistent signs of the signals throughout the two teleconnection classes (NAO-like and zonal) oppose this statement. Furthermore, the regression analysis is very sensitive to the volcanic eruption in 1257, suggesting that the regression coefficients are not very robust. The composites of the teleconnections 'sp_n' and 'se2_c' have the same sign, even though they are associated with differing atmospheric circulation patterns (also evident for the composites of *SST*). A process-based explanation is therefore not possible.
But most importantly, the regression coefficients of the teleconnection indices onto the sea-ice edge reflect the results from the regression analysis of *SST* in the northern North Atlantic. The sea ice edge strongly depends on the ocean temperature, for which reason no separation of the two variables is possible with this approach. No connection between the sea ice edge and the different teleconnections in the Euro-Atlantic sector is found with the applied method.

7.3 Discussion

The approach used in this thesis does not allow for a final conclusion that specific *SST*-patterns or variations in the North Atlantic sea ice extent are coupled to different states of teleconnectivity in the Euro-Atlantic sector. In general, it is difficult to bring together the composites and regression coefficients of each teleconnection, as the discrepancies prevail. However, in the North Atlantic and North Pacific regions, some box pairs show similar *SST*-patterns in composites and regression coefficients, which could point towards a regional-scale or hemispheric-scale coupling of *SST* and the occurrence of North Atlantic teleconnections. Yet, it is challenging to consider related processes, as the magnitudes of the *SST*-patterns are very small. The *SST*-patterns in the eastern North Pacific are not consistently linked to either meridional or zonal teleconnections and the signs are not coherent between composites and regression coefficients. Hence, no link of *SST* in the eastern North Pacific to the state of the North Atlantic climate variability can be established. In contrast, a regional coupling between North Atlantic *SST* and the different teleconnection states is more likely. According to the composites and the regression coefficients, high NAO-like teleconnection activity is related to colder temperatures in the central North Atlantic.

Overall, strong discrepancies between the composites and the regression coefficients of both *SST* and the sea ice edge are present. While the composites show both positive and negative anomalies, the regression coefficients are mostly positive. One reason for the diverging patterns of the composites and the regression coefficients could be that patterns visible in the composite maps are non-linearly linked to the occurrences of specific teleconnections, which is not considered by linear regression analysis. Another point is that the composites are calcu-

lated for situations when teleconnection axes between the related box pairs are detected for at least 10 consecutive periods, while the linear regression is computed with the index describing the strength of the teleconnectivity (equation 6.1). These two quantities are deduced independently from each other and therefore do not perfectly match (Fig. 6.11).

It is suspicious that the regression coefficients of all indices have mostly positive values (*SST* almost all over the globe, sea ice edge only between 15° W and 10° E), even though the periods from 1240 to 1270 (strong cooling induced by a major volcanic eruption) and from 1850 to 2099 (strong warming signal) are excluded from the analysis and *SST* is linearly detrended. Theoretically, it could be possible that high teleconnection activity in the North Atlantic (no matter if NAO-like or zonal) is linearly linked to globally warmer *SST* conditions and a retreat of the sea ice in the North Atlantic. But it is more likely that the regression analysis is still biased by an unknown factor.

At this point, also the applied method has to be scrutinized. The teleconnection indices used for the regression analyses only make a statement about the strength of the teleconnections between two boxes, but do not take into account the phase, which finally controls the large-scale atmospheric flow. Therefore, only the mean states of *SST* or the sea ice extent during the occurrence of the different teleconnections can be analyzed, but not the underlying processes. Furthermore, 30-year running means of *SST* and the sea ice edge are analyzed in order to be compatible with the indices. Due to this smoothing, processes below the 30-year scale are difficult to identify, as the amplitudes are strongly damped. On the other hand, 'normal' teleconnection indices, such as the winter-mean NAO-index, just account for the phase of the teleconnection, but not for its presence/absence (only inferable from the amplitude). Hence, regression analysis of these indices with *SST* or the sea ice edge cannot explain the different conditions (NAO-like or zonal).

There are many studies assessing the relationship between *SST* or the sea ice extent in the North Atlantic and the phase of the classic NAO-index on different spatial scales. Very recently, *Reintges et al.* (2017) investigated the variability of the NAO-index and its relationship to the circulation in the Atlantic Ocean in climate models and observations, and they concluded that the sub-decadal variability originates from dynamical two-way air-sea interactions. *Nakamura et al.* (2015) found a negative phase shift of the NAO-index induced by Arctic sea ice retreat. They argued that the sea ice reduction induces a local warming of the atmosphere at high latitudes, which decreases the geopotential height gradient between the mid- and high-latitudes and hence shifts the NAO-index towards the negative phase. Unfortunately, most studies concerning the NAO and its relationship to the ocean or the sea ice deal with phase shifts of the NAO, but not with spatial changes of the structures. Nevertheless, the two examples mentioned above illustrate that the variability of the North Atlantic atmospheric circulation is strongly coupled to other components of the climate system, even though they address only the temporal variability. Therefore, couplings between the ocean or the sea ice with the spatial variability seem likely, and based on the rudimentary analysis conducted in this thesis,

we cannot exclude them.

External forcings, such as volcanic eruptions, variations in the solar irradiance or changes in the atmospheric composition, might also contribute to spatial variations of teleconnections. In the simulation used in this thesis, a period with very low teleconnectivity in the North Atlantic occurs simultaneously with the largest volcanic eruption during the simulation. Of course, this could be a coincidence, which is supported by the fact that other large volcanic eruptions (e.g. around 1450 or 1850) are not accompanied by extraordinary low teleconnection activity (Figs. 3.1 and 6.12). Furthermore, no linkage between external forcings and the migration of the centers of action (*Raible et al.* 2014) or the indices of teleconnections (*Gõmez-Navarro and Zorita* 2013) was found in modeling studies. Finally, internal atmospheric dynamics likely play an important role in altering the position of the teleconnections, as the NAO is primarily an atmospheric feature generated without two-way-couplings to the ocean.

Chapter 8

Conclusions and outlook

8.1 Conclusions

Teleconnections are an important part of internal climate variability and exert extensive impacts on the atmospheric circulation. In the North Atlantic region, the North Atlantic Oscillation is the most important feature of internal climate variability and strongly determines the predominant weather situation and surface climate variables throughout large parts of the Euro-Atlantic sector, especially in winter. Additionally to the well-studied short-term variations of the NAO, the North Atlantic climate variability also fluctuates on decadal to multidecadal time scales. Further, the spatial structure of the NAO is variable as well. It is crucial to improve our understanding of these processes also on long time scales, because they act as a substantial element of uncertainty in the projection of future climate. In this thesis, the temporal and spatial variability of North Atlantic teleconnections are investigated in a transient 1250-year simulation with the fully coupled Community Earth System Model.

Many state-of-the-art comprehensive climate models have problems in simulating dynamical processes closely linked to the NAO, such as atmospheric blockings at high latitudes (e.g. *Davini and Cagnazzo* 2014). In the CESM simulation, systematic biases of Z500 and the zonal wind at mid-latitudes similar to the ones described for other models are found in the CESM simulation. Despite these biases, the spatial patterns of the dominant wintertime modes of variability in the North Atlantic are generally well captured in the CESM simulation, even though the underlying formation processes are not necessarily simulated appropriately (*Davini and Cagnazzo* 2014). The teleconnections obtained by applying the teleconnectivity method over 1000 years strongly resemble the ones calculated with EraInterim reanalysis data, both at the surface and at 500 hPa, showing that the barotropic structure of the NAO is simulated. The leading EOFs of the North Atlantic sector slightly differ from the observed ones, with an overall eastward shift of the NAO-dipole in EOF1 and a rotated structure in EOF2.

In the first part of the analysis (section 6.1), the temporal characteristics of NAO-indices are investigated. The wavelet power spectra of the grid point- and EOF-based indices indicate strong non-stationarity with variability on various different time scales and no persistent and

predominant frequency. The highest amplitudes are found at frequencies corresponding to sub-decadal to decadal (4-16 years) and multi-decadal (32-64 years) time scales. Especially at the latter frequencies, active phases with enhanced low-frequency variability alternate with passive phases. The power maxima of the two indices are mostly in phase and at similar frequencies, even though the amplitude of the EOF-based index is slightly reduced. The results match with the ones obtained from studies with both observed and reconstructed indices, showing that the temporal characteristics of the NAO are properly simulated by CESM.

The spatial variations of the North Atlantic climate variability are assessed with three different methods, all of them based on 30-year running mean teleconnectivity maps (section 6.2). The first approach uses the pattern correlation tool, where the spatial structure is compared to a reference pattern. The variability of the simulated teleconnectivity patterns is investigated by computing pattern correlation time series between every time period and all remaining time steps, resulting in a 1221×1221 correlation matrix. Its analysis shows that time steps with generally high pattern correlation values with the other periods resemble each other, and the same is true for time steps with generally low pattern correlation values. Hence, the mean value of every time series is a representative parameter to describe the spatial structure of the teleconnectivity. It turns out that high mean pattern correlation values are associated with a NAO-like pattern, and low values with zonally (east-west) aligned structures in the teleconnectivity field. Building on these findings, every teleconnectivity map is assigned to one of four classes, depending on the value of the mean pattern correlation.

The second approach uses a K-means clustering algorithm to statistically group the teleconnectivity maps. The clustering produces well separated groups only for very high numbers of clusters, which is not suitable to tackle the research questions. To ensure comparability with the other methods, 4 clusters are chosen, but only two of them show clear teleconnection structures. As the clustering does not result in a proper classification describing the spatial variability of the North Atlantic teleconnections, it is not further considered.

Thirdly, a more process-based approach is applied, where teleconnectivity maps are classified by detecting teleconnection axes between typically linked regions. Thereby, six box pairs are defined, each three representing meridionally and zonally aligned teleconnections, respectively. In doing so, we obtain four categories, characterized by a NAO-like dominated situation, a mixture of NAO- and zonally oriented teleconnections, an 'only-zonal' pattern and a situation where both meridional and zonal teleconnections are absent.

All classification methods yield that during most of the time, NAO-like structures dominate the teleconnectivity maps of the North Atlantic. The axes-based classification groups 71% of the time steps into the groups 'Only NAO' and 'NAO and zonal', while 43% of the time steps are associated with zonal teleconnections ('Only zonal' and 'NAO and zonal') and 15% do not show any connection. Despite this predominance of NAO-like structures, the spatial structures are subjected to strong variations during the simulation, which is emphasized when we do

not group the box pairs into the meridional and zonal categories, but look at occurrences of teleconnections between all box pairs. For example, the box pair 'nao', associated with centers of action close to the Azores and Iceland, is indeed the most prominent teleconnection of the North Atlantic sector, but there exist many long-lasting gaps, during which other teleconnections dominate. Furthermore, not only shifts of the centers of action (e.g. northerly shift of the northern NAO-center) occur, but also the disappearance of NAO-like structures is found in the simulation. Also periods with no teleconnection axes at all in the North Atlantic sector are simulated by the model, such as the period between 1240 and 1270. During this period, all indices describing the strength of teleconnectivity drop, indicating that the teleconnectivity values are very low in the entire domain.

The pattern correlation method is simple and implemented easily, and generally shows a good agreement with the axes-based results. However, the fact that the pattern correlation approach does not account for the extraordinary period of low teleconnectivity between 1240 and 1270 points towards major shortcomings of this method. Obviously, also the method based on the detection of teleconnection axes between box pairs is defective, as subjective decisions have to be made during the definition of the box borders and the threshold for teleconnectivity axes. However, a precise visual analysis of the teleconnectivity fields allows a proper choice of the box pairs. Overall, we conclude that this method is the most suitable among the three to represent the variability of the North Atlantic teleconnections.

In the second part of the results (chapter 7), linkages between the spatial variations of the teleconnections in the Euro-Atlantic sector and the sea surface temperature and the sea ice extent are investigated. Firstly, composite maps are calculated during persistent periods (at least 10 consecutive 30-year mean periods) of the different teleconnections. Secondly, the relationship between the occurrence of the different teleconnections and SST and the sea ice extent is evaluated by linear regressions of indices describing the strength of the teleconnections with the two variables. For SST, we found that the composite patterns and the regression coefficients in the central North Atlantic are similar during the four NAO-like teleconnections. Hence, this SST-pattern could be interpreted as favorable for NAO-like teleconnections. High amplitudes are also found in the composites and regression coefficients of the eastern North Pacific, but the signs of the patterns cannot be consistently linked to either meridional or zonal teleconnections. Despite the relatively high magnitudes of the signals, we assume that no coupling from the eastern North Pacific SST and the spatial variability of the North Atlantic teleconnections exists. No connection between the sea ice extent and the strength of teleconnectivity in the North Atlantic is found, as no consistent patterns throughout the teleconnection classes are present. Both the composites and the regression coefficients rather show a strong dependence to SST in the northern North Atlantic.

Concluding, the analysis of the driving forces of the spatially variable teleconnections in the Euro-Atlantic sector presented in this thesis is far from being complete. In order to tackle this complex problem appropriately, many more factors than only mean states of the sea surface

temperature and the sea ice extent have to be taken into account, such as ocean circulations, internal atmospheric dynamics and different time scales.

8.2 Outlook

Many open questions remain. Further studies concerning not only the temporal, but also the spatial variability of teleconnections are pertinent. Therefore, some suggestions and ideas for future research are given in the following.

- In this study, only the winter (DJF) mean teleconnections were analyzed. Even though the climate variability in the North Atlantic is the strongest in wintertime, it is still present also during the rest of the year, and partly shows strongly differing patterns from the winter structures (e.g. summer-NAO). Therefore, we can expect that these patterns are also subjected to both temporal and spatial variability. Also the driving forces were only analyzed during the winter months. Especially the inert ocean has a memory, which allows for inter-seasonal and inter-annual coupling to the atmosphere.

- In order to systematically assess the drivers for the observed spatial variability of the NAO, idealized sensitivity simulations with GCMs could be performed. For example, simulations with prescribed SST-values (e.g. climatological SST) and only one-directional coupling could give valuable insights into the role of dynamical interactions between the ocean and the atmosphere. When the spatial variability significantly differs from the one obtained with the fully coupled model, this hints that the interplay between ocean and atmosphere plays an important role in generating this variability. If this is the case, SST-patterns in specific regions which are likely to be the driving force of the variability (e.g. cold central North Atlantic surrounded by warm SST, as proposed in section 7.1) could be inserted in a next step. Otherwise, when the spatial variability is similar to the one simulated with fully coupled atmosphere-ocean dynamics, it is likely that internal atmospheric processes or other forcings are responsible. Obviously, this procedure can also be applied to other components of the climate system and to external forcings. However, owing to the fact that millennium-scale simulations with highly resolved GCMs are computationally very costly, the choice of the sensitivity experiments has to be made well-considered. Still, meaningful results might also be obtained from shorter simulations, as the time scale of the spatial variations of the NAO lies far below millennia.

- The analysis presented here only focuses on the climate variability in the Euro-Atlantic sector, but also teleconnections in other regions show similar variations. For example, the Pacific/North American pattern (PNA) exhibits similar spatial variability as the NAO (*Raible et al.* 2014). Teleconnections are not only confined to the extra-tropics, as the examples ENSO and West African Monsoon illustrate. While the former and its predominant mechanisms are extensively studied, there are open questions about the drivers of multi-decadal variations of the West African Monsoon.

List of Figures

List of Tables

Bibliography

Ångström, A.: Teleconnections of climatic changes in present time. *Geografiska Annaler*, **17**, 242–258, 1935.

Appenzeller, C., Stocker, T. F., and Anklin, M.: North Atlantic Oscillation dynamics recorded in Greenland ice cores. *Science*, **282**, 446–449, 1998.

Baldwin, M. P. and Dunkerton, T. J.: Propagation of the Arctic Oscillation from the stratosphere to the troposphere. *Journal of Geophysical Research: Atmospheres*, **104**, 937–946, 1999.

Barbosa, S., Silva, M. E., and Fernandes, M. J.: Wavelet analysis of the Lisbon and Gibraltar North Atlantic Oscillation winter indices. *International Journal of Climatology*, **26**, 581–593, 2006.

Barnston, A. G. and Livezey, R. E.: Classification, seasonality and persistence of low-frequency atmospheric circulation patterns. *Monthly Weather Review*, **115**, 1083–1126, 1987.

Benedict, J. J., Lee, S., and Feldstein, S. B.: Synoptic view of the North Atlantic Oscillation. *Journal of the Atmospheric Sciences*, **61**, 121–144, 2004.

Bjerknes, J.: Atlantic air-sea interactions. *Advanced Geophysics*, **10**, 1–82, 1964.

Bjerknes, J.: Atmospheric teleconnections from the equatorial Pacific. *Monthly Weather Review*, **97**, 163–172, 1969.

Blackmon, M. L. and White, G. H.: Zonal wavenumber chararcteristics of Northern Hemisphere transient eddies. *Journal of the Atmospheric Sciences*, **39**, 1985–1998, 1982.

Brayshaw, D. J., Hoskins, B., and Blackburn, M.: The basic ingredients of the North Atlantic storm track. Part I: Land – sea contrast and orography. *Journal of the Atmospheric Sciences*, **66**, 2539–2558, 2009.

Camenisch, C., Keller, K. M., Salvisberg, M. et al.: The 1430s: A cold period of extraordinary internal climate variability during the early Spörer Minimum with social and economic impacts in north-western and central Europe. *Climate of the Past*, **12**, 2107–2126, 2016.

Czaja, A., Robertson, A. W., and Huck, T.: The role of Atlantic ocean-atmosphere coupling in affecting NAO-variability. In: *The North Atlantic Oscillation: Climatic significance and environmental impact*, 147–172. 2003.

Davini, P. and Cagnazzo, C.: On the misinterpretation of the North Atlantic Oscillation in CMIP5 models. *Climate Dynamics*, **43**, 1497–1511, 2014.

Davini, P. and D'Andrea, F.: Northern Hemisphere atmospheric blocking representation in global climate models: Twenty years of improvements? *Journal of Climate*, **29**, 8823–8840, 2016.

Dee, D. P., Uppala, S. M., Simmons, A. J. et al.: The ERA-Interim reanalysis: Configuration and performance of the data assimilation system. *Quarterly Journal of the Royal Meteorological Society*, **137**, 553–597, 2011.

Defant, A.: Die Schwankungen der atmosphärischen Zirkulation über dem nordatlantischen Ozean im 25-jährigen Zeitraum 1881-1905. *Geografiska Annaler*, **6**, 13–41, 1924.

Domingues, M. O., Mendes, O., and Da Costa, A. M.: On wavelet techniques in atmospheric sciences. *Advances in Space Research*, **35**, 831–842, 2005.

Dove, H. W.: Über die nicht periodischen Änderungen der Temperaturvertheilung auf der Oberfläche der Erde. *Abhandlungen der Königlichen Akademie der Wissenschaften in Berlin 1839*, 305–440, 1841.

Drinkwater, K. F., Belgrano, A., Borja, A., Conversi, A., Edwards, M., Greene, C. H., Ottersen, G., Pershing, a. J., and Walker, H.: The response of marine ecosystems to climate variability associated with the North Atlantic Oscillation. *Geophysical Monograph Series*, **134**, 211–234, 2003.

Eden, C. and Willebrand, J.: Mechanism of interannual to decadal variability of the North Atlantic circulation. *Journal of Climate*, **14**, 2266–2280, 2001.

Exner, F. M.: Übermonatliche Witterungsanomalien auf der nördlichen Erdhälfte im Winter. *Sitzungsberichte d. Kaiserl. Akad. der Wissenschaften*, **122**, 1165–1241, 1913.

Feldstein, S. B.: The dynamics of NAO teleconnection pattern growth and decay. *Quarterly Journal of the Royal Meteorological Society*, **129**, 901–924, 2003.

Folland, C. K., Knight, J., Linderholm, H. W., Fereday, D., Ineson, S., and Hurrell, J. W.: The summer North Atlantic Oscillation: Past, present and future. *Journal of Climate*, **22**, 1082–1103, 2008.

Gao, C., Robock, A., and Ammann, C.: Volcanic forcing of climate over the past 1500 years: An improved ice core-based index for climate models. **113**, 1–15, 2008.

Glowienka-Hense, R.: The North Atlantic Oscillation in the Atlantic-European SLP. *Tellus*, **42**, 497–507, 1990.

Gõmez-Navarro, J. J. and Zorita, E.: Atmospheric annular modes in simulations over the past millennium: No long-term response to external forcing. *Geophysical Research Letters*, **40**, 3232–3236, 2013.

Hann, J.: Zur Witterungsgeschichte von Nord-Grönland, Westküste. *Meteorologische Zeitschrift*, **7**, 1890.

Holton, J. R.: *An introduction to dynamic meteorology, 4th Edition*. Academic Press Inc., 2004.

Hunke, E. C. and Lipscomb, W. H.: CICE: The Los Alamos Sea Ice Model documentation and software user' s manual LA-CC-06-012. Technical report, 2010.

Hurrell, J. W.: Decadal trends in the North Atlantic Oscillation - Regional temperatures and precipitation. *Science*, **269**, 676–679, 1995.

Hurrell, J. W.: The climate data guide: Hurrell North Atlantic Oscillation (NAO) Index (station-based). 2017.

Hurrell, J. W. and Deser, C.: North Atlantic climate variability: The role of the North Atlantic Oscillation. *Journal of Marine Systems*, **78**, 28–41, 2009.

Hurrell, J. W., Holland, M. M., Gent, P. R. et al.: The Community Earth System Model: A framework for collaborative research. *Bulletin of the American Meteorological Society*, **94**, 1339–1360, 2013.

Hurrell, J. W., Kushnir, Y., and Ottersen, G.: An overview of the North Atlantic Oscillation. In: *The North Atlantic Oscillation: Climatic significance and environmental impact*, 134, 1–35. 2003.

Hurrell, J. W., Loon, H. V., and Van Loon, H.: Decadal variations in climate associated with the North Atlantic Oscillation. *Climatic Change at High Elevation Sites*, **36**, 301–326, 1997.

Hurtt, G. C., Chini, L. P., Frolking, S., Betts, R. A., Feddema, J., and Fischer, G.: Harmonization of land-use scenarios for the period 1500 – 2100: 600 years of global gridded annual land-use transitions, wood harvest, and resulting secondary lands. *Climatic Change*, **109**, 117–161, 2011.

Jones, P. D., Osborn, T. J., and Briffa, K. R.: Pressure-based measures of the North Atlantic Oscillation (NAO): A comparison and an assessment of changes in the strength of the NAO and in its influence on surface climate parameters. In: *The North Atlantic Oscillation: Climatic significance and environmental impact*, 51–62. 2003.

Kaufman, L. and Rousseeuw, P. J.: Partitioning around medoids (Program PAM). In: *Finding groups in data: An introduction to clustering analysis*, 68–125. John Wiley & Sons, Inc, 1990.

Keller, K. M., Joos, F., Lehner, F., and Raible, C. C.: Detecting changes in marine responses to ENSO from 850–2100 CE: Insights from the ocean carbon cycle. *Geophysical Research Letters*, **42**, 518–525, 2015.

Lamarque, J. F., Bond, T. C., Eyring, V. et al.: Historical (1850 – 2000) gridded anthropogenic and biomass burning emissions of reactive gases and aerosols: Methodology and application. *Atmospheric Chemistry and Physics*, **10**, 7017–7039, 2010.

Lau, K. M. and Weng, H.: Climate signal detection using wavelet transform: How to make a time series sing. *Bulletin of the American Meteorological Society*, **76**, 2391–2402, 1995.

Lawrence, D. M., Oleson, K. W., Flanner, M. G. et al.: Parameterization improvements and functional and structural advances in version 4 of the Community Land Model. *Journal of Advances in Model ing Earth Systems*, **3**, 1–27, 2009.

Le, T., Sjolte, J., and Muscheler, R.: The influence of exernal forcing on subdecadal variability of regional surface temperature on CMIP5 simulations. *Journal of Geophysical Research: Atmospheres*, **121**, 1671–1682, 2016.

Lee, S. and Kim, H.: The dynamical relationship between subtropical and eddy-driven jets. *Journal of the Atmospheric Sciences*, **60**, 1490–1503, 2003.

Lehner, F., Joos, F., Raible, C. C., Mignot, J., Born, A., Keller, K. M., and Stocker, T. F.: Climate and carbon cycle dynamics in a CESM simulation from 850 to 2100 CE. *Earth System Dynamics*, **6**, 411–434, 2015.

Lorenz, E. N.: *The nature and theory of the gerneral circulation of the atmosphere*. World Meteorological Organization (WMO), 1967.

Luterbacher, J., Gyalistras, D., Xoplaki, E., and Wanner, H.: Reconstruction of monthly NAO and EU indices back to AD 1675. *Geophysical Research Letters*, **26**, 2745–2748, 1999.

Maechler, M., Rousseeuw, P., Struyf, A., Hubert, M., Studer, M., Roudier, P., and Gonzalez, J.: Finding Groups in Data: Package ' cluster '. 2017.

Marshall, J., Johnson, H., and Goodman, J.: A study of the interaction of the North Atlantic Oscillation with ocean circulation. *Journal of Climate*, **14**, 1399–1421, 2001.

Moore, G. W. K., Renfrew, I. A., and Pickart, R. S.: Multidecadal mobility of the North Atlantic Oscillation. *Journal of Climate*, **26**, 2453–2466, 2013.

Moss, R., Edmonds, J., Hibbard, K. et al.: The next generation of scenarios for climate change research and assessment. *Nature*, **463**, 747–56, 2010.

Mysterud, A., Stenseth, N. C., Yoccoz, N. G., Ottersen, G., and Langvatn, R.: The response of terrestrial ecosystems to climate variability associated with the North Atlantic Oscillation. In: *The North Atlantic Oscillation: Climatic significance and environmental impact*, 235–262. 2003.

Nakamura, T., Yamazaki, K., Iwamoto, K., Honda, M., Miyoshi, Y., Ogawa, Y., and Ukita, J.: A negative phase shift of the winter AO/NAO due to the recent Arctic sea-ice reduction in late autumn. *Journal of Geophysical Research: Atmospheres*, **120**, 3209–3227, 2015.

Neale, R. B., Richter, J. H., Conley, A. J. et al.: Description of the NCAR Community Atmosphere Model (CAM 4.0). Technical report, NCAR, 2010.

Orsolini, Y. J., Kindem, I. T., and Kvamstø, N. G.: On the potential impact of the stratosphere upon seasonal dynamical hindcasts of the North Atlantic Oscillation: A pilot study. *Climate Dynamics*, **36**, 579–588, 2011.

Pedersen, R. A., Cvijanovic, I., Langen, P. L., and Vinther, B. M.: The impact of regional Arctic sea ice loss on atmospheric circulation and the NAO. *Journal of Climate*, **29**, 889–902, 2016.

Pongratz, J., Reick, C., Raddatz, T., and Claussen, M.: A reconstruction of global agricultural areas and land cover for the last millennium. *Global Biogeochemical Cycles*, **22**, 2008.

Pozo-Vázquez, D., Esteban-Parra, M. J., Rodrigo, F. S., and Castro-Díez, Y.: A study of NAO variability and its possible non-linear influences on European surface temperature. *Climate Dynamics*, **17**, 701–705, 2001.

Raible, C. C.: *Introduction to Atmospheric Circulation and Modes of Variability*. Lecture notes, University of Bern, 2017.

Raible, C. C., Casty, C., Luterbacher, J. et al.: Climate variability - observations, reconstructions, and model simulations for the Atlantic-European and Alpine region from 1500-2100 AD. *Climatic Change*, **79**, 9–29, 2006.

Raible, C. C., Lehner, F., González-Rouco, J. F., and Fernández-Donado, L.: Changing correlation structures of the Northern Hemisphere atmospheric circulation from 1000 to 2100 AD. *Climate of the Past*, **10**, 537–550, 2014.

Raible, C. C., Luksch, U., and Fraedrich, K.: Precipitation and Northern Hemisphere regimes. *Atmospheric Science Letters*, **5**, 43–55, 2004.

Raible, C. C., Luksch, U., Fraedrich, K., and Voss, R.: North Atlantic decadal regimes in a coupled GCM simulation. *Climate Dynamics*, **18**, 321–330, 2001.

Reintges, A., Latif, M., and Park, W.: Subdecadal North Atlantic Oscillation variability in observations and the Kiel Climate Model. *Climate Dynamics*, **48**, 3475–3487, 2017.

Rossby, C. G. and Collaborators: Relation between variations in the intensity of the zonal circulation and the displacements of the semi-permanent centers of action. *Journal of Marine Research*, **2**, 38–55, 1939.

Rousseeuw, P. J.: Silhouettes: A graphical aid to the interpretation and validation of cluster analysis. *Journal of Computational and Applied Mathematics*, **20**, 53–65, 1987.

Schmidt, G. A., Jungclaus, J. H., Ammann, C. M. et al.: Climate forcing reconstructions for use in PMIP simulations of the Last Millennium (v1.1). *Geoscientific Model Development*, **5**, 185–191, 2012.

Smith, R., Jones, P., Briegleb, B. et al.: The Parallel Ocean Program (POP) reference manual: Ocean component of the Community Climate System Model (CCSM). *Rep. LAUR-01853*, **141**, 1–141, 2010.

Stephenson, D. B., Wanner, H., Brönnimann, S., and Luterbacher, J.: The history of scientific research on the North Atlantic Oscillation. In: *The North Atlantic Oscillation: Climatic significance and environmental impact*, 37–50. 2003.

Taylor, K. E., Stouffer, R. J., and Meehl, G. A.: An overview of CMIP5 and the experiment design. *Bulletin of the American Meteorological Society*, **93**, 485–498, 2012.

Thompson, D. W. J. and Wallace, J. M.: The Arctic Oscillation signature in the wintertime geopotential height and temperature fields. *Geophysical Research Letters*, **25**, 1297–1300, 1998.

Torrence, C. and Compo, G. P.: A practical guide to wavelet analysis. *Bulletin of the American Meteorological Society*, **79**, 61–78, 1998.

Ulbrich, U. and Christoph, M.: A shift of the NAO and increasing storm track activity over Europe due to anthropogenic greenhouse gas forcing. *Climate Dynamics*, **15**, 551–559, 1999.

Vieira, L. E. A., Solanki, S. K., and Nov, S. R.: Evolution of the solar magnetic flux on time scales of years to millenia. *Astronomy and Astrophysics*, **509**, 2010.

Vinther, B. M., Andersen, K. K., Hansen, A. W., Schmith, T., and Jones, P. D.: Improving the Gibraltar/Reykjavik NAO index. *Geophysical Research Letters*, **30**, 2222, 2003.

Visbeck, M., Chassignet, E. P., Curry, R. G., Delworth, T. L., Dickson, R. R., and Krahmann, G.: The ocean's response to North Atlantic Oscillation variability. *Geophysical Monograph Series*, **134**, 113–145, 2003.

Walker, G. T. and Bliss, E. W.: World weather V. *Memoirs of the Royal Meteorological Society*, **4**, 53–84, 1932.

Wallace, J. M. and Gutzler, D. S.: Teleconnections in the geopotential height field during the Northern Hemisphere winter. *Monthly Weather Review*, **109**, 784–812, 1981.

Walter, K., Luksch, U., and Fraedrich, K.: A response climatology of idealized midlatitude thermal forcing experiments with and without a storm track. *Journal of Climate*, **14**, 467–484, 2001.

Wang, Y. H., Magnusdottir, G., Stern, H., Tian, X., and Yu, Y.: Decadal variability of the NAO: Introducing an augmented NAO index. *Geophysical Research Letters*, **39**, 1–5, 2012.

Wanner, H., Brönnimann, S., Casty, C., Luterbacher, J., Schmutz, C., and David, B.: North Atlantic Oscillation. Concepts and studies. *Surveys in Geophysics*, 321–382, 2001.

Wilks, D. S.: *Statistical methods in the atmospheric sciences*. Elsevier Academic Press, 1995.

Acknowledgements

Mein Dank gebührt zuallererst Christoph Raible, der während meiner Masterarbeit viel Zeit und Aufwand investiert hat, um mich zu beraten und betreuen und um Fragen jeglicher Art zu beantworten.

Vielen Dank auch an Cevi für die regelmäsige Unterstützung bei allerlei Computerfragen (sei es Text-Formatierung in LaTeX oder nervige Linux-Anfängerprobleme) sowie die angenehme Arbeitsatmosphäre in B99 und interessante Gespräche on- und off-Topic. Danke auch an die KUP für die Bereitstellung der Daten und Infrastruktur sowie an die Kollegen für die allgemein gute Atmosphäre, z.B. während der Kaffeepausen.

Des Weiteren will ich meine Kommilitonen aus dem Klima-Master erwähnen, mit denen ich zwei coole Jahre verbingen konnte. Vor allem die ausgiebigen Tischtennis- und Fifa-Sessions, Kaffee- und Gelato-Pausen und das gelegentliche Feierabendbier haben mir geholfen, trotz des vor allem am Ende aufkommenden Stresses abzuschalten. Un grand merci aussi à Céline pour la relecture de ma thèse.

Vielen Dank auch an meine Mitbewohner Perrine und Hugi, die tagtäglich meine Launen aushalten mussten und mir gegen Ende meiner Masterarbeit die ein oder andere Nachlässigkeit im Haushalt verziehen haben.

Zu guter Letzt möchte ich mich bei Clara und meiner Familie bedanken, die sich immer wieder mein Leid angehört und mir Mut und Durchhaltevermögen zugesprochen haben.

Declaration of consent

on the basis of Article 28 para. 2 of the RSL05 phil.-nat.

Name/First Name: Pickl, Moritz

Matriculation Number: 15-112-485

Study program: M.Sc. in Climate Sciences with specialization in atmospheric sciences

Bachelor ☐ Master ☑ Dissertation ☐

Title of the thesis: Changing teleconnection patterns in the North Atlantic from 850-2099 AD - The role of atmosphere-ocean-sea ice interaction

Supervisor: Prof. Dr. Christoph Raible

I declare herewith that this thesis is my own work and that I have not used any sources other than those stated. I have indicated the adoption of quotations as well as thoughts taken from other authors as such in the thesis. I am aware that the Senate pursuant to Article 36 para. 1 lit. r of the University Act of 5 September, 1996 is authorised to revoke the title awarded on the basis of this thesis. I allow herewith inspection in this thesis.

.....

Place/Date

Signature